



## CONTENTS

---

**3**

**Anna Rudawska, Piotr Penkała,  
Bartosz Mischuk, Dana Stančková**

**Analysis of the effect of assembly joints technology on the strength of adhesive joints of poly(methyl methacrylate) (PMMA) used in advertising elements**

*Analiza wpływu technologii wykonania połączeń montażowych na wytrzymałość połączeń adhezyjnych polimetakrylanu metylu, stosowanych w elementach reklamowych*

**11**

**Krzysztof Piasta, Przemysław Kupidura,  
Jakub Michalski**

**Computational evaluation of assembly technique influence on ballistic performance of a bullet – non-linear relation between méplat size and the drag coefficient**

*Analiza numeryczna wpływu metody montażu elementów pocisku na charakterystyki balistyczne – nieliniowa zależność współczynnika oporu od średnicy wierzchołka*

**19**

**Jan Godzimirski, Marek Rośkowicz, Iga Barca**

**Selection of materials for repairing punctures of metal skin of semi-monocoque structures using composite patches**

*Dobór materiałów do napraw przebić pokryć metalowych struktur półskorupowych z zastosowaniem łat kompozytowych*

**33**

**Tomasz Samborski, Andrzej Zacharski,  
Andrzej Zbrowski, Mirosław Mrozek,  
Stanisław Kozioł, Margaret Haller de Hallenburg**

**Disposable personal protective equipment vending machine**

*Automat vendingowy do sprzedaży jednorazowej odzieży ochronnej*

**41**

**Viktor Mautner, Katarina Horvat, Marija Stoić,  
Antun Stoić**

**Simulation of displacement of cutting tool holders used for turning**

*Symulacja odkształceń i odchyłeń uchwytów na narzędzia skrawające stosowanych do toczenia*

**50**

**Janusz Kobiałka, Andrzej Barszcz**

**Noise emission and vibration study of a Mistra RD-165 FHAD grader to reduce environmental harmful impact**

*Badania hałasu i drgań równiarki Mistra RD-165 FHAD mające na celu zmniejszenie jej szkodliwego wpływu na środowisko*



Quarterly „Technologia i Automatyizacja Montaży” is listed on the list of scored journals of Polish Ministry of Education and Science - 40 points.

**ANALYSIS OF THE EFFECT OF ASSEMBLY JOINTS TECHNOLOGY ON THE STRENGTH OF ADHESIVE JOINTS OF POLY(METHYL METHACRYLATE) (PMMA) USED IN ADVERTISING ELEMENTS**

**ANALIZA WPLYWU TECHNOLOGII WYKONANIA POŁĄCZEŃ MONTAŻOWYCH NA WYTRZYMAŁOŚĆ POŁĄCZEŃ ADHEZYJNYCH POLIMETAKRYLANU METYLU, STOSOWANYCH W ELEMENTACH REKLAMOWYCH**

**Anna RUDAWSKA<sup>1,\*</sup> , Piotr PENKAŁA<sup>2</sup>,  
Bartosz MISZCZUK<sup>3</sup>, Dana STANČEKOVÁ<sup>4</sup> **

<sup>1</sup> Lublin University of Technology, Faculty of Mechanical Engineering, Nadbystrzycka 36, 20-618 Lublin, PL, a.rudawska@pollub.pl

<sup>2</sup> The University College of Applied Sciences in Chełm, Institute of Technical Sciences and Aviation, Poczтовая 54, 22-100 Chełm, e-mail ppenkala@panschelm.edu.pl

<sup>3</sup> The University College of Applied Sciences in Chełm, Institute of Technical Sciences and Aviation, Poczтовая 54, 22-100 Chełm, e-mail miszczuk14434@nauka.panschelm.edu.pl

<sup>4</sup> University of Žilina, Faculty of Mechanical Engineering, Univerzitna 1, 010 26, Žilina, SK, dana.stancekova@fstroj.uniza.sk

\* Corresponding author: a.rudawska@pollub.pl

**Abstract**

The aim of the article was to present issues related to the influence of the assembly joints technology (the type of adhesive material and the adhesive application) on the strength of the adhesive joints of poly(methyl methacrylate) (PMMA) used in the production of advertising elements. Angular adhesive joints, which are one of the types of joints made in the construction of advertising elements, were used in the study. The bonded material was poly(methyl methacrylate) (PMMA) of 8 mm thick. Two types of adhesives were used to make the adhesive joints: one-component solvent-based adhesives and methylene chloride as a solvent. Experimental tests determined the wettability of the surface of the adherends (with and without a protective coating) and the work of adhesion based on the measurement of the contact angle, as well as the strength of adhesive joints in accordance with the ISO 4578 standard. Based on the results of strength tests, it can be seen that the use of a solvent allows for obtaining equally strong joints as with the use of solvent-based adhesives. The purposefulness of using coatings protecting not only against dirt or mechanical damage in the form of scratches was also confirmed, but also the possibility of increasing (security) adhesive properties, defined in this case by wettability.

**Key words:** adhesive joint, angular joint, poly(methyl methacrylate), wettability, contact angle, strength.

**Streszczenie**

Celem artykułu było przedstawienie zagadnień związanych z wpływem technologii połączeń montażowych (rodzaju materiału klejącego i sposobu aplikacji kleju) na wytrzymałość połączeń klejowych z poli(metakrylanu metylu) (PMMA) stosowanych w produkcji elementów reklamowych. W badaniach wykorzystano połączenia klejowe kątowe, które są jednym z rodzajów połączeń wykonywanych w konstrukcji elementów reklamowych. Łączonym materiałem był poli(metakrylan metylu) (PMMA) o grubości 8 mm. Do wykonania połączeń klejowych zastosowano dwa rodzaje jednoskładnikowych klejów rozpuszczalnikowych oraz chlorek metylenu, jako rozpuszczalnik. W badaniach doświadczalnych określono zwilżalność powierzchni klejonych elementów (z powłoką ochronną i bez) oraz pracę adhezyjną na podstawie pomiaru kąta zwilżania, a także wytrzymałość połączeń klejowych zgodnie z normą ISO 4578. Na podstawie wyników badań wytrzymałościowych można stwierdzić, że zastosowanie rozpuszczalnika pozwala na uzyskanie połączeń równie wytrzymałych, jak przy



zastosowaniu klejów rozpuszczalnikowych. Potwierdzono również celowość stosowania powłok zabezpieczających nie tylko przed zabrudzeniami czy uszkodzeniami mechanicznymi w postaci zarysowań, ale także w celu zwiększenia (zabezpieczenia) właściwości adhezyjnych, określanych w tym przypadku przez zwilżalność.

**Słowa kluczowe:** połączenie adhezyjne, połączenie kątowna, poli(metakrylan metylu), zwilżalność, kąt zwilżania, wytrzymałość.

## 1. Introduction

Poly(methyl methacrylate) (PMMA) is a polymer material that is used in many areas of industry, including in the automotive, construction, medical and advertising industries [1,2]. This material is characterized by good mechanical properties and low toxicity. In addition, it is one of the hardest thermoplastics, resistant to UV. Poly(methyl methacrylate) (PMMA)

is used for various types of advertising panels, spatial letters and forms, illuminated boards or spatial forms. PMMA is also used in the construction industry, the aviation industry (aircraft windows), the food industry, the automotive industry (e.g. license plates, headlight elements) and others [3]. Among the various types of assembly joints in advertising elements, angular connections can be distinguished (Fig. 1), e.g. in various types of stands.

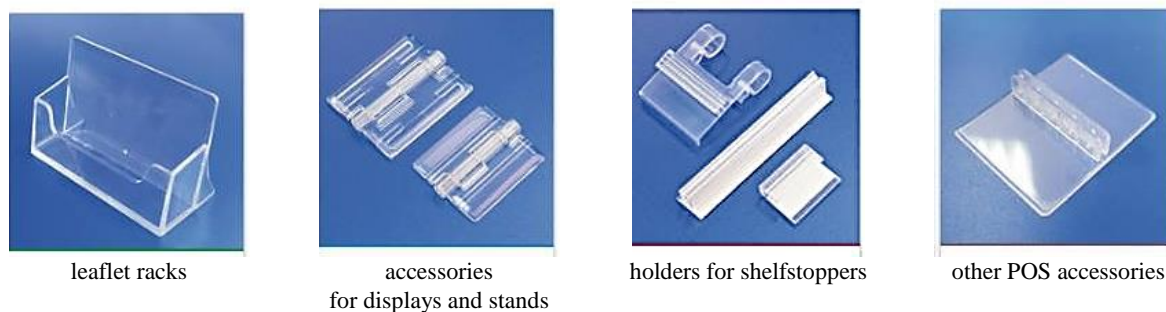


Figure 1. Examples of angular joints in the advertising industry [4]

Poly(methyl methacrylate) (PMMA) is available in many colors and textures, which allows to choose according to aesthetic requirements. In the production process, many plates made of poly(methyl methacrylate) are coated with a scratch-resistant coating [3].

One of the types of PMMA assembly joints is bonding [5], although this material is difficult to bonding due to its chemical resistance (and for this reason it is often used in elements of medical equipment). But, among others due to the requirements for the aesthetics and transparency of the joining point, this method of the joints is often chosen. Adhesives used to join metals and other polymer materials do not show strong adhesion to PMMA.

Solvent adhesives used to join PMMA are usually chemically aggressive adhesives, as they contain dichloromethane. They have a low viscosity and are very volatile, i.e. they produce a fairly high vapor pressure, and for this reason, dosing, e.g. with a syringe, causes the adhesive to constantly drip from the dispensing tip. For this reason, they can leave residues on the surface of PMMA components, and this material is often used for aesthetic reasons. Therefore, it is important to adopt an appropriate process for applying the adhesive to the adherends. These adhesives join the elements by partial dissolution of

the surface layer of the surface of the element and evaporation. Thanks to this, the assembly joints are joints created using the phenomenon of diffusion [2,6].

The aim of the conducted research was to evaluate the technology of preparing the adhesive joint, and in particular the application of the adhesive on the joined surfaces, in terms of the adhesive joints strength determined by the failure force and to determine the wettability of the surfaces of the adherend.

## 2. Materials and methods

The subject of the research were poly(methyl methacrylate) (PMMA) angular adhesive joints, which are one of the types of assembly joints made in the construction of advertising elements. The experimental tests carried out consisted in determining the wettability of the surfaces of the joined materials (with and without a protective coating), making angular adhesive joints and subjecting them to strength tests.

### 2.1. Adherend

The samples that were subjected to the bonding process were made of poly(methyl methacrylate) (PMMA) with the following dimensions 8 x 30 x 50 mm, which were then subjected to the bonding

process. The thickness of the elements resulted from the thickness of the materials used in the company for advertising construction elements. PMMA samples were made of a colorless plate produced by casting in special moulds. The product obtained in this way has lower internal stresses and is of better quality than extruded boards. In addition, cast plates are more chemically resistant, have a harder, more even surface and better optical properties [3]. The plate from which the samples were made had a high transparency of about 92%.

Table 1. Selected properties of samples made of cast PMMA plates [7]

Properties	Casting board
Density (max) g/cm <sup>3</sup>	1.19
Rockwell hardness, M scale	95
Young's modulus, min., MPa	3300
Relative elongation at break, min., %	5.5
Thermal expansion coefficient, mm/m/°C	0.065

## 2.2. Preparing conditions of adhesive joints

### 2.2.1. Surface treatment method

Bonding surfaces must be dry and clean, especially free of oil, grease or release agents [2]. Another aspect in the surface treatment of this adherend is its roughness. This material is characterized by a small

surface roughness, so the share of mechanical anchors of the adhesive practically does not affect the strength of the adhesive joints. For aesthetic reasons, in many cases it is not possible to apply mechanical treatment of the surface. The influence of surface roughness on the strength of joints has been described in numerous works [8-13]. Therefore, in this case, it is necessary to focus on the use of the appropriate type of the adhesive, which allows the connection to be made using partial dissolution of the surface of the joined material and the phenomenon of diffusion.

The surface of the joined samples was covered on both sides with a special protective coating. Due to the fact that it should remain on the product as long as possible (as the surface of the joined material is susceptible to scratches and dirt), it was removed just before the bonding process. Considering the material properties, the surface of the PMMA samples was only wiped with a dry cloth. No degreasing agent, e.g. based on alcohol, was used, because the use of alcohol could damage the surface of this material.

### 2.2.3. Adhesive joint and adhesive

The subject of the tests was angular adhesive joints of the polymer material, which was PMMA with a thickness of 8 mm, the diagram of which is shown in Figure 2. The samples were laser cut.

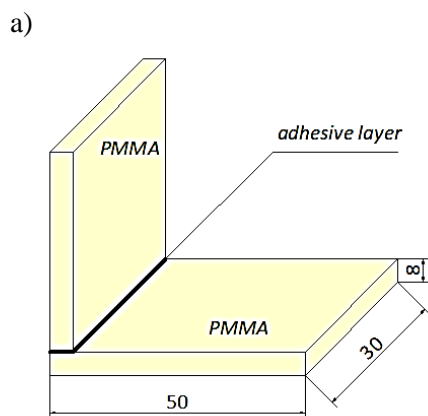


Figure 2. Angular adhesive joints: a) scheme (dimensions in mm), b) real view

Two types of adhesives were used to make three series of adhesive joints (5 joints in each series):

- one-component solvent transparent adhesive ACRIFIX 1S 0116 (Röhm GmbH Acrylic Products, Weiterstadt, Germany)
- low-viscosity solvent-based adhesive Technicoll® 108 (RUDERER KLEBTECHNIK GmbH, Zorneding, Germany),

and methylene chloride (dichloromethane, CH<sub>2</sub>Cl<sub>2</sub>, distributor: STANLAB, Lublin, Poland), as a solvent (Table 2).

Joints made with the use of the adhesive were an example of adhesive joints, while with the use of solvent - adhesive joints, but made taking into account the phenomenon of diffusion.

Methylene chloride (dichloromethane) is an organic chemical compound from the group of alkyl halides; chlorine derivative of methane. At room

temperature and atmospheric pressure, it is a colorless, rapidly evaporating liquid. It has a characteristic, sweetish smell. Methylene chloride (dichloromethane) is the base product of many solvents supporting the removal of e.g. old paint coatings from metals, wood, stone, etc. Methylene chloride is used as a very effective solvent and diluent [14].

Table 2. Selected properties of methylene chloride [based on the safety data sheet]

Properties	Date/ description
Form	colorless liquid
Composition	dichloromethane
Chemical formula	CH <sub>2</sub> Cl <sub>2</sub>
Molar mass	84.93 g/mol
Solubility in water	16 g/dm <sup>3</sup> (20°C)
Melting temperature	- 95°C
Boiling point	39.5 – 40.5°C
Temperature of self-ignition	605°C
pH value	neutralne
Density	1.326 g/cm <sup>3</sup> (20°C)

The listed solvent adhesives, according to the manufacturers' catalog information, are dedicated to making angle joints. Selected properties of the adhesives used are listed in Table 3.

When making adhesive joints with these adhesives, it is recommended that the pieces to be bonded fit snugly together, as small gaps will not be filled.

ACRIFIX® 1S 0116 was applied from a nozzled bottle to the edge of one of the items to be bonded, which, starting from one side, is then placed in contact with the second. After a short holding time, the bond is locked in position. Slight pressure applied to the bonded surface during drying also reduced bubble formation.

In the case of Technicoll® adhesive, the joining technology consisted in immersing the edge of one of the adherend in the Technicoll® adhesive, and after 5 to 10 seconds of surface impact (etching), the bonded elements were joined and pressed. This is one of the recommended, depending on the size of the surfaces of the elements to be joined, variants of the joining technology with the use of this group of adhesives.

Table 3. Selected properties of solvent adhesives [15]

Properties	Solvent adhesive	
	ACRIFIX 1S 0116	Technicoll® 108
Chemical base	contains ethylformate, nitroethane, butan-1-ol	dichloromethane: a solution of acrylic polymer in a mixture of solvents
Viscosity at 20°C, mPa·s	650-900	5
Density at 20°C, g/cm <sup>3</sup>	1.0	1.3
Refractive index, n <sub>D</sub> <sup>20</sup>	-1.39	
Color	clear to yellowish; color does not affect bonding properties	colourless change of colour does not influence characteristics of adhesion
Flash point (DIN 53213)	< 4°C	
Curing	physically, through evaporation and absorption in the bonded articles	
Wet-bonding time		approx. 5-10 seconds (one-sided application)
Thickener	approx. 10%	flakes of polycarbonate (max. 15%)

The solvent will usually evaporate residue-free. Under best circumstances the resistance to temperature is similar to the one of the feedstock. Because variation may occur during the bonding process, the resistance to temperature may be lower.

The joint was made by pressing the edges of two PMMA specimens together in a previously prepared fixture, containing a wooden stop in the form of an angle bar. The upper sample was pressed against the lower with a small steel weight (>200g). Joining took place at room temperature (approx. 20°C) with air

humidity (40-60%). The curing time in the methylene chloride mixture was in the range of 30-60 seconds at room temperature (approx. 20°C).

### 2.3. Research description

The experimental studies carried out included:

- determining the wettability of the surface and the work of adhesion (W<sub>a</sub>) based on the measurement of the contact angle,
- performance of strength tests.

Determination of surface wettability and work of adhesion concerned poly(methyl methacrylate) (PMMA) samples with and without a protective coating. Strength tests included tests of angular joints made with two types of the solvent adhesives and with the use of a solvent.

Wettability of the surface of poly(methyl methacrylate) samples and the work of adhesion were determined on the basis of direct measurement of the contact angle ( $\Theta$ ) with distilled water. There were 3 samples per each batch: uncoated and adhesive coated.

The work of adhesion was calculated on the basis of the value of the contact angle using the formula (1) [6]:

$$W_a = \gamma_L (1 + \cos\Theta) \quad (1)$$

where the symbol  $\gamma_L$  denotes the surface free energy of the wetting liquid.

The contact angle  $\Theta$  of the surface of the epoxy coatings was measured using a contact angle analyzer - Phoenix 150 goniometer with Surfaceware 7 software. Work of adhesion ( $W_a$ ) value  $W_a$  using Surfaceware 7 calculation options.

Drops of the measuring liquid were applied to the analyzed substrate using a micropipette mounted above the tested plate. The volume of drops of the

measuring liquids ranged from 5 to 7  $\mu\text{l}$ . Five drops of the distilled water were applied to the surface of the tested samples. The picture of the drop was taken with a digital camera with the lens placed parallel to the tested substrate. After that, 10-13 measurements were made and the mean per each sample batch was calculated. The contact angle was measured immediately following the application of a drop of the measuring liquid (after a few seconds). The measurements of the contact angle were performed at a temperature of  $21 \pm 1^\circ\text{C}$  and air humidity of  $28 \pm 2\%$ . Before contact angle measurements, the adherends surfaces were wiped with a dry cloth.

Adhesive joints were subjected to strength tests, in accordance with the ISO 4578 standard, on the Zwick/Roell Z150 testing machine, using the appropriate fastening in the machine's screw-wedge holders.

### 3. Results

#### 3.1. Results of contact angle measurements, determination of adhesion work and assessment of surface wettability

The results of the contact angle measurements and calculated of work of adhesion are presented in Tables 4 – 7 and Figure 3.

Table 4. Measurement results of contact angle and calculation work of adhesion for samples without protective coatings – without degreasing

Type of measuring liquid	Measurement series number	Contact angle [ $^\circ$ ] (average of 10-13 measurements)	Work of adhesion [mN/m]
Distilled water	1	52.25	117.34
	2	55.89	113.56
	3	51.04	117.79
Mean		53.06	116.23
Standard deviation		2.52	2.32

Table 5. Measurement results of contact angle and calculation work of adhesion for samples without protective coatings – with degreasing

Type of measuring liquid	Measurement series number	Contact angle [ $^\circ$ ] (average of 10-13 measurements)	Work of adhesion [mN/m]
Distilled water	1	66.17	101.47
	2	62.09	106.77
	3	63.12	106.64
Mean		63.79	104.96
Standard deviation		2.12	3.02

Table 6. Measurement results of contact angle and calculation work of adhesion for samples with protective coatings – without degreasing

Type of measuring liquid	Measurement series number	Contact angle [ $^\circ$ ] (average of 10-13 measurements)	Work of adhesion [mN/m]
Distilled water	1	66.53	102.36
	2	63.04	105.59
	3	68.00	99.96
Mean		65.86	102.64
Standard deviation		2.55	2.83

Table 7. Measurement results of contact angle and calculation work of adhesion for samples with protective coatings – with degreasing

Type of measuring liquid	Measurement series number	Contact angle [°] (average of 10-13 measurements)	Work of adhesion [mN/m]
Distilled water	1	59.28	110.01
	2	63.61	105.10
	3	57.10	111.80
<b>Mean</b>		60.00	108.94
<b>Standard deviation</b>		3.31	3.52

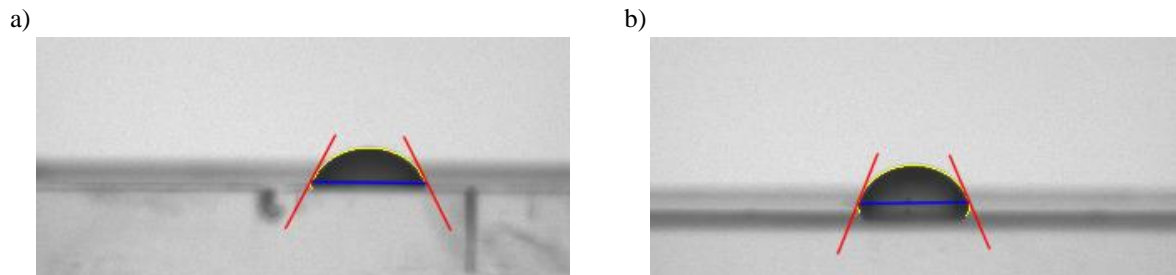


Figure 3. Contact angle of the surface of the samples (without degreasing): a) without protective coatings, b) with protective coatings

When analysing the results presented in tables 4-7, the following dependencies were observed:

1) uncoated samples are characterized by the lowest value of the contact angle (average value), amounting to  $53.06^\circ$ , hence they are characterized by the highest wettability and the highest work of adhesion ( $W_a$  is  $116.23 \text{ mN/m}$ ),

2) the use of degreasing contributes to an increase in the value of the contact angle by about 20%, which means a deterioration of the surface wettability and a decrease in the value of the work of adhesion by about 10%,

3) samples with a protective coating obtained a greater value of the contact angle than without the

coating by nearly 25%, which means that they have lower surface wettability.

Due to the fact that the protective coating was removed just before the contact angle measurements, there was no danger of soiling or reducing the energy activity of the surface. It was noticed that the protective coating itself is covered with impurities, because degreasing even this coating contributes to the increase of its wettability.

### 3.2. Strength test results

A comparison of the failure force of the analyzed variants of PMMA adhesive joints is shown in Figure 4 and Figure 5.

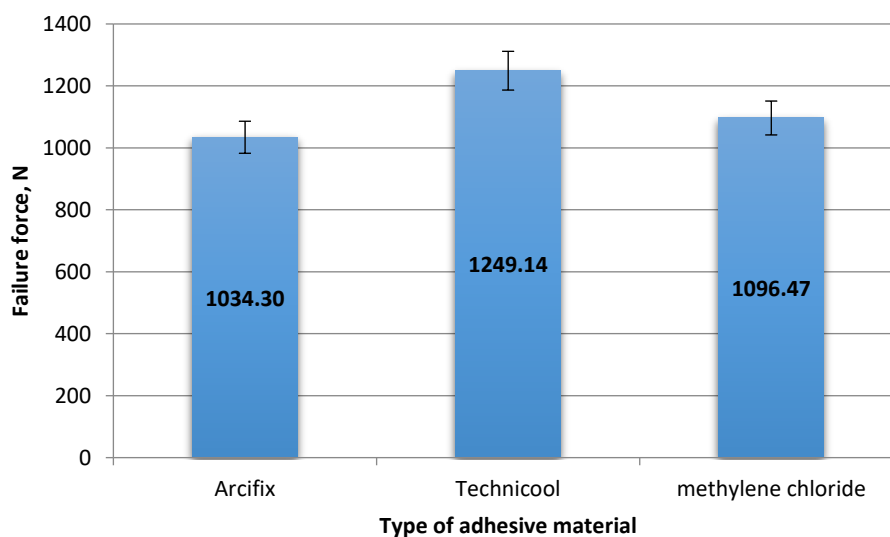


Figure 4. The value of the failure force of PMMA angular assembly joints

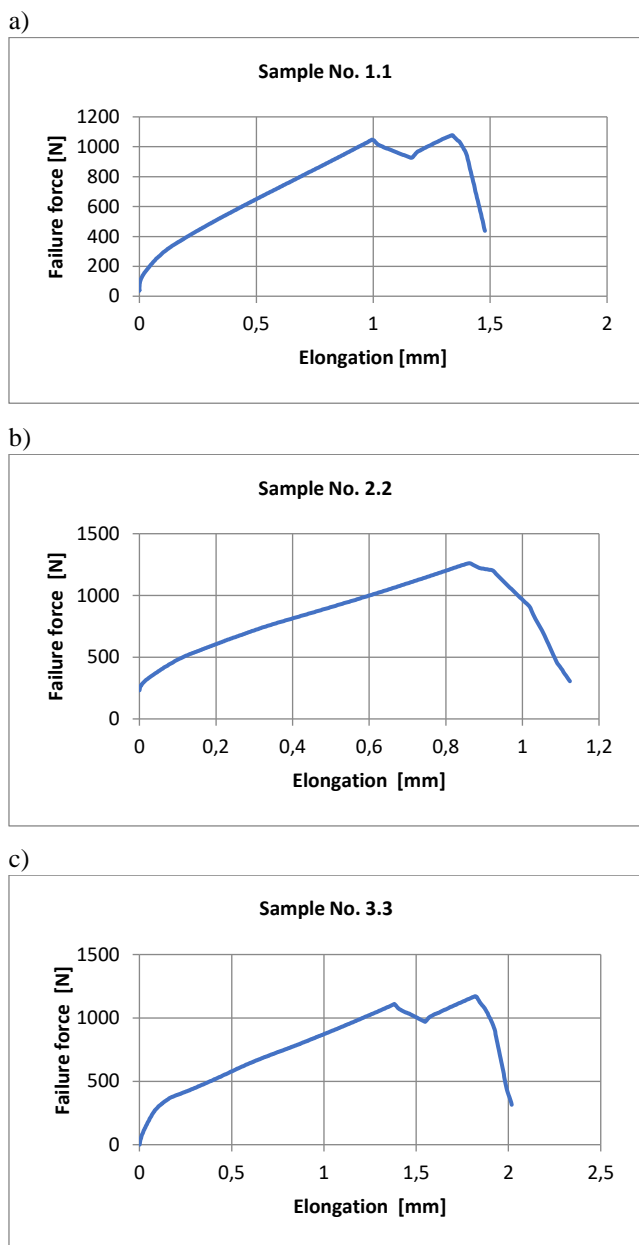


Figure 5. Examples of the elongation-failure force relationship for assembly joints made with: a) Acrifix adhesive, b) Technicool adhesive, c) methylene chloride solvent

On the basis of the obtained results (Figure 4) it was noticed that the highest value of the failure force was characteristic for the adhesive joints made with the use of one-component solvent adhesive Technicool (1249.14 N). On the other hand, joints made with the second Arcifix adhesive (also one-component solvent) had about 17% lower strength. Both adhesives used are one-component solvent adhesives, dedicated to joining polymeric materials and to making angular and T-shaped joints. It can be assumed that both the chemical composition and the assembly technology recommended for a given type of adhesive resulted in differences in the value of the failure force.

The joints made with methylene chloride solvent had a lower strength (1096.47 N) by about 12% than the highest value obtained in the case of the adhesive joints made with the one-component solvent adhesive Technicool (1249.14 N). Both types of assembly joints required the use of adhesive materials, which allows to obtain a transparent joint, which is important when making advertising construction elements.

Relationships between elongation-failure force (Figure 5) for individual types of assembly joints are similar.

In addition to the type of adhesive material in the work [5] it was noted that the decisive factor, among others, the value of the failure force of samples of PMMA and PVC adhesive joints are the properties of the bonded material.

### 3.3. Basic descriptive statistics

A basic descriptive statistics was presented in Table 8 and it was performed on the results from the strength test.

Basic statistics is the basis for further analyzes and inferences. Based on the data presented in Table 8, one can notice the repeatable accuracy of making adhesive joints, regardless of the adhesive material used.

Table 8. Parameters of descriptive statistics of the joints failure force

Type of adhesive material used to make PMMA joints	Basic descriptive statistics									
	No. of tests	Mean	Median	Mode	Mode size	Range	Variance	Standard deviation	Skewness	Kurtosis
Acrifix adhesive	15	1034.30	1035.16	multiple	1	25.63	69.0465	8.3094	-0.0369	-1.2816
Technicool adhesive	14	1249.14	1249.64	multiple	1	25.39	71.2871	8.4432	-0.1391	-1.2910
methylene chloride solvent	17	1096.47	1096.80	multiple	1	25.26	70.2013	8.3786	-0.0136	-1.2748

#### 4. Conclusions

Based on the presented results, the following observations can be made regarding individual groups of studies:

1) based on the results of the measurement of the contact angle and the assessment of wettability, it was noted that:

- the surface of the element made of poly(methyl methacrylate) (PMMA) without the protective coating is characterized by greater wettability (smaller value of the contact angle) than the surface of the samples with the protective coating,
- due to the fact that the protective coating was removed just before the contact angle measurements, there was no risk of soiling or reducing the energy activity of the surface,
- it was noticed that the protective coating itself is covered with impurities, because degreasing even this coating contributes to the increase in its wettability,
- it can be confirmed that the use of coatings protecting not only against dirt or dust, or protection against mechanical damage in the form of scratches, but also the ability to protect and increase adhesive properties, defined in this case by wettability, can be confirmed.

2) the obtained results of the failure force of the angular joints allow to assume that:

- both the adhesive application technology and the type of adhesive will affect the strength of the joints,
- the use of a solvent allows for an equally strong joints as with the use of solvent adhesives (with a failure forces comparable to adhesive joints made by some solvent adhesives).

The use of solvent adhesives and solvents is one of the methods of making assembly joints of poly(methyl methacrylate). The surface of elements made of poly(methyl methacrylate) (PMMA) is characterized by very low roughness, therefore the use of the assumptions of the theory of diffusion adhesion in this case becomes significant. The small surface roughness does not allow for effective joints of such elements, because the phenomenon of mechanical adhesion will not occur in the general component of the adhesion, due to the lack of possibility of mechanical anchoring of the adhesive. Therefore, the use of solvent adhesives or solvents allows for effective joining of

such elements, although, as it results from the research, it is necessary to analyze, among others, adhesive application technology, resulting from the properties of the adhesive, including its viscosity.

#### References

1. Żuchowska Danuta. 2000. *Polimery konstrukcyjne: Wprowadzenie do technologii i stosowania*. Warszawa: WNT.
2. Adams Robert D., Comyn John, Wake Wiliam Charles. 1997. *Structural Adhesive Joints in Engineering Book*. United Kingdom: Springer.
3. <https://tuplex.pl>, dostęp: 12.04.2023.
4. <https://posshop.pl/materialy-pos>, dostęp: 12.04.2023.
5. Rudawska Anna, Sztorc Piotr, Kujan Krzysztof. 2012. „Wpływ wybranych czynników konstrukcyjnych na wytrzymałość połączeń klejowych PVC oraz PMMA”. *Przetwórstwo Tworzyw 5*: 505–510.
6. Baldan Ahmet. 2012. „Adhesion phenomena in bonded joints”. *International Journal of Adhesion and Adhesives* 38: 95-116.
7. <https://tuplex.rs/reklama/plyty-akrylowe-ekstrudowane/akcesoria/akcesoria-301>, dostęp: 12.04.2023.
8. Zielecki Władysław, Pawlus Paweł, Perłowski Ryszard, Dzierwa Andrzej. 2013. „Surface topography effect on strength of lap adhesive joints after mechanical pre-treatment”. *Archives of Civil and Mechanical Engineering* 13 (2): 175–185.
9. Rudawska Anna. 2010. „Wpływ sposobu przygotowania powierzchni na wytrzymałość połączeń klejowych blach ze stali odpornej na korozję”. *Technologia i Automaty-zacja Montażu* 3: 36–39.
10. Chumble Rohan P., Darekar Deepak H. 2017. Influence of surface roughness of adherend on strength of adhesive joint”. *International Journal of Engineering Development and Research* 5 (4): 100–106.
11. Doluk Elżbieta, Rudawska Anna, Brunella Valentina. 2020. „The Influence of technological factors on the strength of adhesive joints of steel sheets”. *Advances in Science and Technology Research Journal* 14(1): 107-15.
12. Rudawska Anna, Izabela Miturska, Dana Stančeková. 2020. The effect of the surface preparation method on the ultimate strength of single lap adhesive joints of selected construction materials. *Technologia i Automaty-zacja Montażu* 4: 14–20.
13. Boutar Yasmina, Naïmi Sami, Mezlini Salah, Ali Moez B.S. 2016. „Effect of surface treatment on the shear strength of aluminium adhesive single-lap joints for automotive applications”. *International Journal of Adhesion and Adhesives* 67: 38–43.
14. <https://sklep.biomus.eu/pl/108-methylene-chlorek>, dostęp: 12.04.2023.
15. <https://www.technicoll.eu/adhesive/technicoll-108.html>, dostęp: 12.04.2023

## COMPUTATIONAL EVALUATION OF ASSEMBLY TECHNIQUE INFLUENCE ON BALLISTIC PERFORMANCE OF A BULLET – NON-LINEAR RELATION BETWEEN MÉPLAT SIZE AND THE DRAG COEFFICIENT

### ANALIZA NUMERYCZNA WPŁYWU METODY MONTAŻU ELEMENTÓW POCISKU NA CHARAKTERYSTYKI BALISTYCZNE – NIELINIOWA ZALEŻNOŚĆ WSPÓŁCZYNNIKA OPORU OD ŚREDNICY WIERZCHOŁKA

Krzysztof PIASTA<sup>1,\*</sup> , Przemysław KUPIDURA<sup>2</sup> , Jakub MICHALSKI<sup>3</sup> 

<sup>1</sup> Military University of Technology, Faculty of Mechatronics, Armament and Aviation, 2 Sylwestra Kaliskiego Str., 00-908 Warsaw, Poland, e-mail: krzysztof.piesta@wat.edu.pl

<sup>2</sup> Military University of Technology, Faculty of Mechatronics, Armament and Aviation, 2 Sylwestra Kaliskiego Str., 00-908 Warsaw, Poland, e-mail: przemyslaw.kupidura@wat.edu.pl

<sup>3</sup> Military University of Technology, Faculty of Mechatronics, Armament and Aviation, 2 Sylwestra Kaliskiego Str., 00-908 Warsaw, Poland, e-mail: jakub.michalski@wat.edu.pl

\* Corresponding author: krzysztof.piesta@wat.edu.pl

#### Abstract

The continuous development of production and assembly techniques gives rise to the idea of following a new approach in the small-arms ammunition design process. Commonly used intermediate cartridges were designed over 60 years ago, and their construction and assembly processes are not significantly different than what was available almost a century ago. Along with the recent development of individual protection devices and with the general availability of modern ballistic plates utilized in *plate carriers* type of individual armor, it sparks the necessity of designing a new, intermediate cartridge, using new assembly and technology methods. The vital aspect of the ammunition design process is a determination of the materials utilized in bullet elements and its assembly method. Therefore, there is a necessity of evaluating if different assembly techniques can provide the improved ballistic performance of a bullet.

The paper includes a comparison of two differently assembled projectiles with steel penetrators: a standard Full Metal Jacket and a reverse-drawn Semi-Jacketed bullet. The designs were evaluated in terms of their external ballistic performance for specific initial conditions using 2D Computational Fluid Dynamics simulations and, separately, with a semi-empirical method. The paper aimed to assess the influence of the assembly method on the bullet's external ballistic performance. Both calculations revealed a nonlinear relation between the projectile méplat diameter and the coefficient of drag, which indicates a limit where the méplat size reduction is beneficial. The results implicate a perspective bullet construction that would provide the user with better external ballistic performance, more consistent and precise than a standard Full Metal Jacket design.

**Keywords:** mechanical engineering, ballistics, assembly methods, CFD, ammunition.

#### Streszczenie

Nieustanny rozwój technik produkcji i montażu rodzi pomysł wykorzystania nowego podejścia w procesie projektowania amunicji do broni strzeleckiej. Obecnie powszechnie stosowane naboje pośrednie zostały zaprojektowane ponad 60 lat temu, a proces ich wykonania i montażu nie różni się znacząco od technologii dostępnej na początku XX wieku. Biorąc pod uwagę dynamiczny rozwój środków ochrony indywidualnej w ostatnim czasie oraz powszechną dostępność nowoczesnych płyt balistycznych stosowanych w kamizelkach kuloodpornych typu *plate carrier*, zaistniała potrzeba zaprojektowania nowego naboju pośredniego, stosując nowoczesne technologie i metody montażu. Jednym z najistotniejszych aspektów procesu projektowania amunicji jest określenie materiału elementów pocisku oraz sposobu ich montażu, dlatego zasadne jest określenie wpływu metody montażu elementów pocisku na jego właściwości balistyczne.



Artykuł zawiera porównanie dwóch różniących się metodą montażu pocisków z rdzeniem stalowym: standardowego pocisku pełnopłaszczyzowego oraz pocisku półpłaszczyzowego. Konstrukcje zostały ocenione pod kątem ich charakterystyk balistyki zewnętrznej dla określonych warunków początkowych za pomocą symulacji komputerowej dynamiki płynów w 2D oraz niezależnie wykorzystując program balistyczny. Celem pracy była ocena wpływu sposobu montażu elementów na właściwości balistyczne pocisku. Obie metody obliczeniowe wykazały nieliniową zależność między wielkością średnicy wierzchołka pocisku a współczynnikiem oporu, wskazując zakres wartości, do których zmniejszanie rozmiaru wierzchołka jest uzasadnione. Wyniki wskazują perspektywiczną konstrukcję pocisku, która zapewniłaby użytkownikowi lepsze charakterystyki balistyki zewnętrznej, zapewniając lepszą powtarzalność i precyzję niż standardowa konstrukcja pocisku pełnopłaszczyzowego.

**Słowa kluczowe:** inżynieria mechaniczna, balistyka, metody montażu, CFD, amunicja.

## 1. Introduction

The possibility of manufacturing new, before-unavailable shapes of different elements on a wide scale, provides an option of following a new approach in designing small-arms ammunition. The design idea of currently used cartridges has not changed for almost 100 years. Moreover, individual protection devices have significantly improved along with the development of new manufacturing and assembly methods. The general availability of ballistic plates and plate carrier vests has increased, therefore it is becoming standard-issued equipment on the battlefield. Modern individual armor consists of Hard Armour Plates made of ceramic or ultra-high-molecular-weight polyethylene (UHMWPE), and Soft Armour Inserts made of dry Kevlar layers or UHMWPE fabric [1]. It provides complete protection from all intermediate cartridges used nowadays, including the armor-piercing rounds [2]. Therefore, there is an urgent need of providing the NATO soldiers with a cartridge that can defeat the opponent equipped with the aforementioned protection devices, which gives the necessity of evaluating a new projectile in terms of external ballistics.

A typical Full Metal Jacket (FMJ) bullet consists of a lead alloy core and a copper jacket. Usually, the lead-antimony alloy is hot or cold extruded into a wire and cut into slugs. Followingly, the slug is pressed in several punches and formed into the final shape of a core, to fit the inner surface of the ogive closely. Then, the core is fed, seated, and closed into the copper, pointed jacket from the rear part, leaving the base of the bullet open. Boattail bullets are then coned and finally closed [3]. Nowadays, projectiles can utilize a steel core inside the copper jacket, filled with a copper slug, instead of a lead core. The assembly method, however, remains similar, with the core fixed through the back of the copper jacket. Such an approach to the design process has its drawbacks and limitations, for instance concerning the shape of the forward part of the bullet: the ogive and méplat, which are vital in the aspect of external ballistics performance. Following a different approach to the main

construction idea may provide the ability to achieve better external ballistic characteristics, greater repeatability, and required armor-piercing abilities of the bullet.

An important reason for further analysis of the materials planned to utilize in a new bullet, is that due to the directives included in regulations of the European Commission on the use of lead in ammunition, toxic-free materials must be used in the new design [4]. The necessity of designing a new, lead-free projectile of improved performance is inevitable.

In a previous analysis, authors have concluded that to achieve the required stopping power while maintaining reasonable peak chamber pressure, a bullet of 6.8 mm diameter would be satisfactory [5]. In terms of the bullet construction, three perspective designs were assessed to be worth analyzing. One construction utilizes a steel penetrator extended from the jacket, assembled from the front. The second is a reverse-jacketed projectile with a light tungsten penetrator extended from a jacket, clasped in an aluminum sleeve, also assembled from the front, and the last design with a tungsten penetrator centered with an aluminum sleeve, but fully jacketed by a copper jacket, assembled in a standard way, from the rear side of the bullet. The main factor differentiating the designs is the choice of assembly direction, creating a Full Metal Jacket or Semi-Jacketed projectile [6].

One of the vital aspects not estimated before is the projectile's ogive shape and méplat diameter. The influence of a differently shaped front part of the bullet on the external ballistics performance was estimated by authors in refs. [7-9]. However, there is still a necessity for analyzing the external ballistic performance of two bullets, with different, before-mentioned assembly methods which provide different possibilities of the méplat dimensions. The main objective of the paper is an estimation of the méplat diameter influence on the aerodynamics of a bullet, to assess which design idea is more perspective.

## 2. Material and methods

The following constructions were analyzed:

- 6.8 mm Full Metal Jacket Steel Core (FMJ SC);
- 6.8 mm Semi-Jacketed Steel Core (S-J SC).

The bullets are characterized by equal mass and overall external shape, with a difference concerning only the diameter of a méplat. Different variations of méplat size were analyzed to assess its influence on the drag coefficient.

### 2.1. 6.8 mm FMJ Steel Core

The first design is a standard Full Metal Jacket bullet with a steel core. The projectile assembly requires forming the steel core, then, inserting the core into the copper jacket from the rear part, filling the space with a copper slug and enclosing the jacket, precisely shaping the ogive, méplat and boattail. The base of the bullet in that case remains open. Currently used intermediate FMJ bullets with the standard manufacturing and assembly methods provide a méplat diameter of 1.0 mm up to 1.6 mm. The design of analyzed construction is shown in Fig. 1.

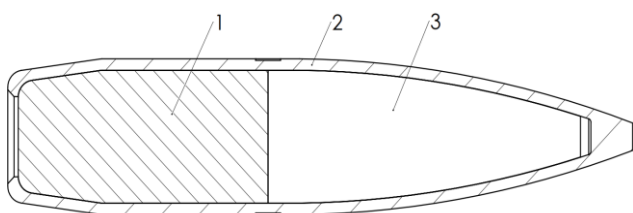


Fig. 1. Cross section of 6.8 mm FMJ Steel Core bullet  
1 – copper slug, 2 – copper jacket, 3 – steel penetrator

### 2.2. 6.8 mm Semi-Jacketed Steel Core

The second construction is a Semi-Jacketed projectile, with a steel arrow-shaped penetrator exposed from the copper jacket. The bullet is assembled from the front part of the jacket, while the copper slug is formed and inserted into the drawn copper jacket and the steel arrow-shaped penetrator is inserted in the jacket and enclosed in it.

The following design provides greater possibilities in terms of precision and consistency of the ogive and méplat dimensions. Therefore, concerning the possibility of manufacturing a steel penetrator shape, designs with méplat diameters of 0.8 mm, 0.6 mm and 0.4 mm were analyzed. The projectile is shown in Fig. 2.

Dimensions and data of the projectiles are shown in Table 1.

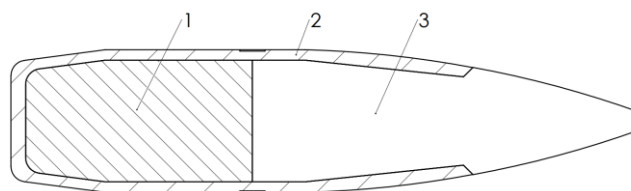


Fig. 2. Cross section of 6.8 mm Semi-Jacketed Steel Core bullet  
1 – copper slug, 2 – copper jacket, 3 – steel penetrator

Table 1. Technical data of designed bullets

Parameter	Value
Bullet length (mm)	30
Bullet mass (g)	6.6
Steel core mass: FMJ/S-J (g)	2.04/2.32
Ogive radius (mm)	50
Méplat diameter (mm)	0.4, 0.6, 0.8, 1.0, 1.2, 1.4, 1.6

## 3. Calculation

Two separate approaches were followed to estimate the performance of designed projectiles. Numerical approach, performing Computational Fluid Dynamics analysis with ANSYS Fluent software, and a semi-empirical approach, through simulations with PRODAS software. For each projectile several calculations were performed, varying the méplat diameter, with all the remaining dimensions preserved.

### 3.1 Numerical approach

Ansys Fluent 2022R2 was used to perform the numerical calculations. The software solves Reynolds-Averaged Navier-Stokes equations using the finite volume method.

#### 3.1.1. Geometry and domain

2D geometries representing the external shape of the projectiles and surrounding domains were designed using the Design Modeler component of Ansys 2022R2. Separate geometries were designed for each méplat diameter size: 0.4 mm, 0.6 mm, 0.8 mm, 1.0 mm, 1.2 mm, and 1.4 mm. To ensure resolved wake flow, the size of the domain was set to approximately 30 diameters radially away from the bullet, 17 diameters forward, and 23 diameters rearwards.

Using Ansys Meshing structured, quadrilateral meshes were created. The vicinity of the projectile surface is presented in Fig. 3. Discretization parameters for each calculation are presented in Tab. 2. The non-dimensional distance from the wall to the first mesh node ( $y^+$  value), should be of the order of 1.0 to correctly resolve the flow in the boundary layer. For all analyzed velocities the  $y^+$  value was maintained lower than 1.0 through the projectile's whole surface,

and less than 0.5 around the base and boattail, to allow a correct solving of the wake flow [10].

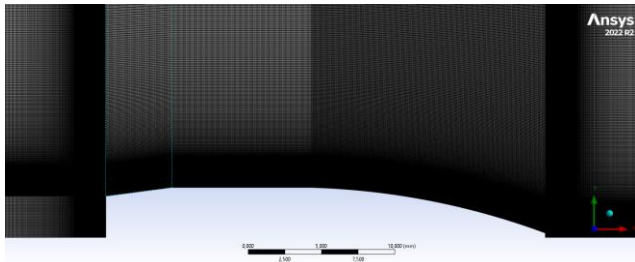


Fig. 3. Mesh generated in proximity of the geometry

Table 2. Discretization scheme parameters and mesh metrics

Parameter	Value
Number of elements	1506800
First cell height (µm)	< 0.44
Max. skewness	0.225
Max. aspect ratio	2604
Min. orthogonal quality	0.933

### 3.1.2. Simulation settings

Steady-state, 2D axisymmetric, double-precision, density-based solver was initiated for the analysis of external compressible flow. The value of zero-yaw drag coefficient is negligibly different for unsteady and steady-state calculations [11], therefore there is no need to follow a computational power demanding unsteady approach. To obtain several values of drag coefficient for each different méplat size, simulations were performed for the steady-flow velocities of Mach 1.5, 2.0, and 2.5, where the latter corresponds to the assumed muzzle velocity of 850 m/s.

In order to model the turbulence in the flow correctly, a viscous model of  $k-\omega$  SST with compressibility effects was chosen. The ideal-gas settings were applied with the viscosity model set to Sutherland [12]. For each simulation, the boundary conditions shown in Table 3 were set. Simulations were initiated using the implicit, First Order Upwind approximation algorithm method, with Roe-FDS flux type and Courant number equal to 0.8. After convergence with the initial solution, the Second Order precision algorithm was followed.

Table 3. Boundary conditions set for the analysis

Boundary	Type
Inlet	Pressure-far-field
Outlet	Pressure-outlet
Axis	Axis
Projectile	Wall (no-slip)
Far-field	Pressure-far-field

Convergence criteria were set of residuals to reduce at least 3 orders of magnitude and the drag coefficient changing less than 0.001 over 500 iterations. The determining factor for all the cases was the change in the drag coefficient value. The solution has converged after approximately 16000 iterations for the velocity of Mach 2.5 and 2.0, and around 25000 iterations for Mach 1.5. Figure 4 presents the residual reduction for the Mach 2.5 case of 1.2 mm méplat diameter simulation. A peak in the values is noticeable after 7000 iterations, due to the discretization theme order change from 2<sup>nd</sup> to 1<sup>st</sup>.

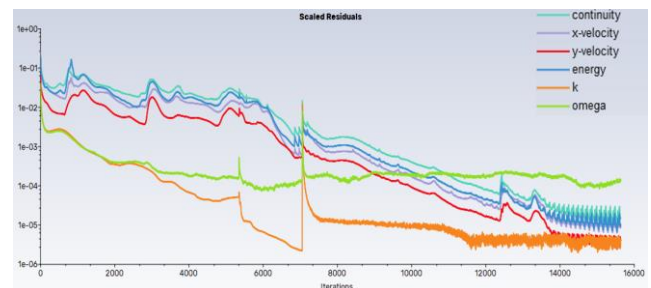


Fig. 4. Residuals behavior (Méplat dia.: 1.2 mm, Mach 2.5):

### 3.2. Semi-empirical approach

Using the PRODAS V3.5 Arrow Tech software, semi-empirical calculations of the projectiles were performed. Geometries of the projectiles were designed (Fig. 5, Fig. 6), with méplat diameter sizes varying from 0.4 mm to 1.6 mm.

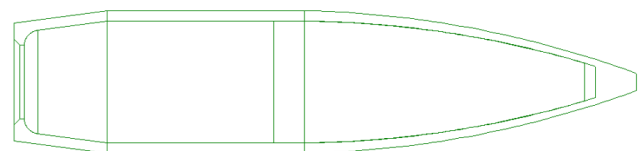


Fig. 5. Prodass geometry of the 6.8 mm FMJ SC projectile

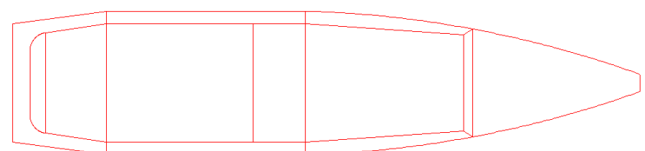


Fig. 6. Prodass geometry of the 6.8 mm S-J SC projectile

To validate the models, stability evaluation was performed, and the results indicated that all the projectiles are characterized by a gyroscopic factor (GF) of over 4.0. For uncertainties of the muzzle velocity, mass distribution and atmospheric conditions, the required GF value should exceed 1.5, therefore the estimation confirmed that the projectiles

are characterized by good stabilization with uncertainties safety margin [13].

To compare the trajectories of designed projectiles, point-blank shooting simulations were performed. The following initial conditions were set [14]:

- muzzle velocity:  $v_0 = 850$  m/s;
- target height:  $h = 0.5$  m;
- barrel length:  $l = 406$  mm;
- barrel twist:  $l_0 = 178$  mm, 6 grooves;
- pressure:  $P_0 = 1013.2$  hPa, temperature:  $t = 15^\circ\text{C}$ , air density:  $\rho_0 = 1.225$  kg/m<sup>3</sup>, speed of sound:  $v_s = 340.2$  m/s.

## 4. Results

### 4.1. Computational Approach

#### 4.1.1. Flow fields

Velocity magnitude fields for the 1.2 mm méplat projectile are shown in Fig. 7. The flow behaviors are practically identical for the remaining cases.

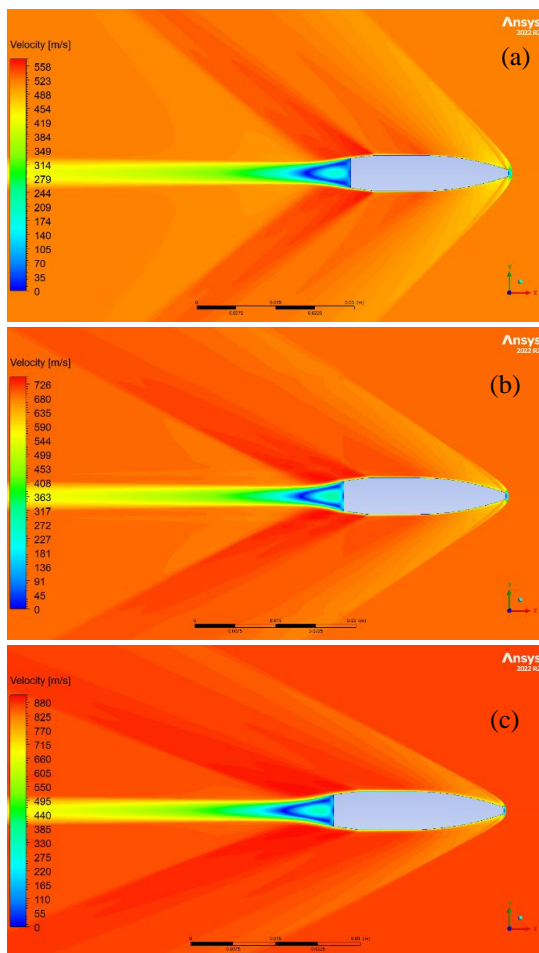


Fig. 7. Velocity fields (méplat dia. 1.2 mm): (a) Mach 1.5, (b) Mach 2.0; (c) Mach 2.5

In the case of Mach 1.5 (Fig. 7a), the flow is supersonic through the whole surface of the projectile,

except for the base region and a small local subsonic region in the vicinity of the blunt nose. The bow shock can be noticed close to the projectile nose with a standoff of approximately 0.5 diameters. The standoff decreases and the curvature of the shock increases with the flow velocity, becoming oblique in Mach 2.0 (Fig. 7b). Furthermore, a trailing shock is visible at the end of the boattail, with a region of very low flow velocity magnitude and pressure at the base of the projectile, which corresponds to the base drag, and increases with the flow speed. In the case of high supersonic velocity of Mach 2.5 (Fig. 7c), the oblique shock angle is even smaller, and the shock wave appears to be almost in contact with the projectile's méplat.

Fig. 8-10 present the nose region for different méplat diameters, in the case of Mach 2.0.

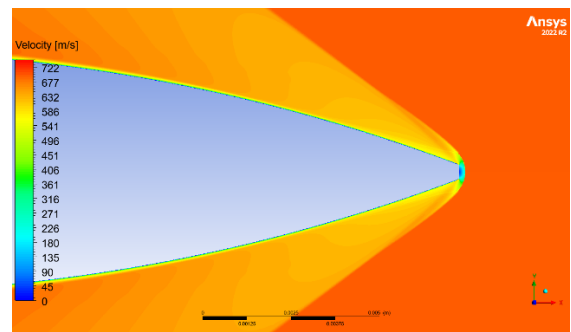


Fig. 8. Velocity field in nose region – méplat dia.: 0.4 mm, Mach 2.0

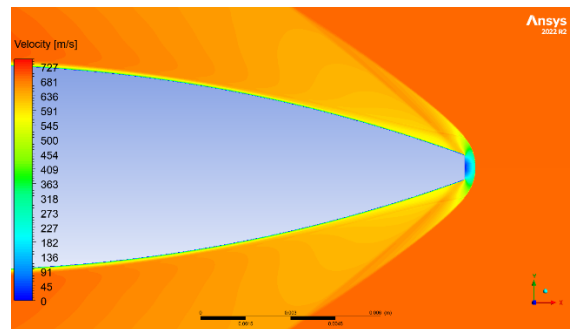


Fig. 9. Velocity field in nose region – méplat dia.: 0.8 mm, Mach 2.0

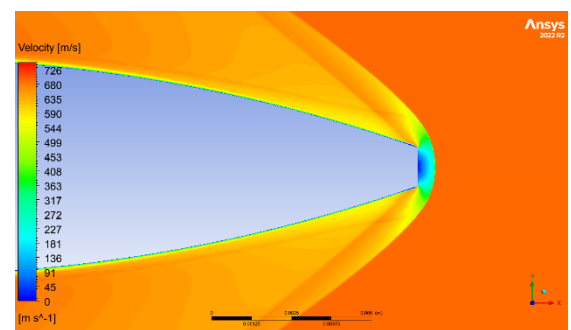


Fig. 10. Velocity field in nose region – méplat dia.: 1.2 mm, Mach 2.0

The diameter of the méplat directly influences the behavior of the shock wave. The increase in méplat diameter results in an increase of the bow shock standoff from the projectile. The local nose subsonic region is noticeably larger with a larger méplat diameter.

#### 4.1.1. Drag coefficient

The calculated drag coefficient values for different flow velocities and méplat diameters are presented in Table 4 and Fig. 11.

Table 4. Calculated drag coefficient – numerical approach

Mach number	Méplat diameter (mm)					
	6.8 mm S-J SC			6.8 mm FMJ SC		
	0.4	0.6	0.8	1.0	1.2	1.4
1.50	0.354	0.354	0.348	0.351	0.353	0.358
2.00	0.300	0.301	0.302	0.304	0.318	0.318
2.50	0.276	0.276	0.273	0.272	0.284	0.290
AVG	0.310	0.310	0.308	0.309	0.318	0.322

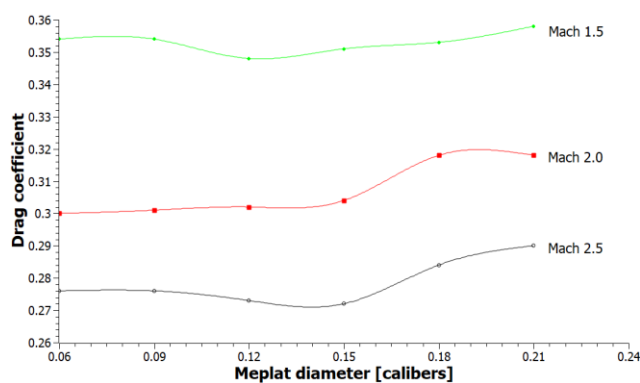


Fig. 11. Calculated drag coefficient versus méplat diameter (numerical results)

The results indicate a non-linear relation between the méplat diameter and drag coefficient. For a set ogive length, the value of drag force reduces with the reduction of a méplat to a certain value. Further reduction of the diameter causes an increase, or at maximum a lack of reduction in the drag coefficient value (case of Mach 2.0). In analyzed case of a 6.8 mm bullet, the lowest drag coefficient of 0.308 was achieved with a méplat size of 8.0, which equals 0.12 calibers. However, the differences between 0.4 mm and 0.8 mm meplat are negligible and can be considered within the calculation error.

### 4.2. Semi-empirical approach

#### 4.2.1. Projectiles trajectories

Point-blank trajectories calculated with the semi-empirical approach are shown in Fig. 12 below.

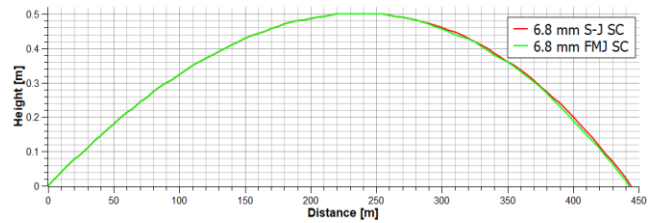


Fig. 12. Point-blank trajectories

There is a slight difference in the point-blank range between analysed projectiles. The 6.8 mm FMJ SC achieves 442.6 m of point-blank range at 850 m/s to a 0.5 m high target, while the 6.8 mm S-J SC equals 444.1 m. The difference of less than 0.4 % however, is negligible.

#### 4.2.2. Drag coefficient

Drag curves calculated with a semi-empirical method for the projectiles 6.8 mm S-J SC with 0.8 mm méplat diameter and 6.8 mm FMJ SC with 1.2 mm méplat are shown in Fig. 13 below.

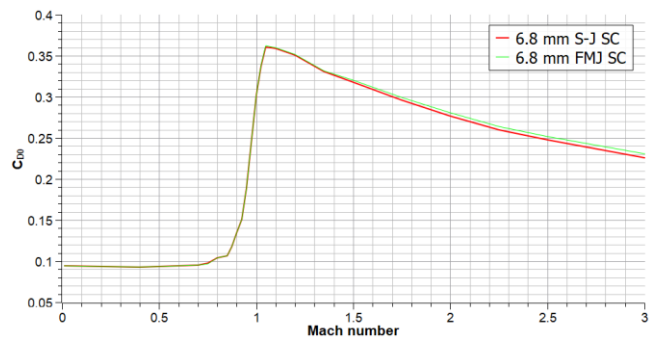


Fig. 13. Calculated drag curves of the projectiles

As assumed, due to the almost identical external shape of the designs, with slight variations of the méplat diameter, the drag curves of the projectiles closely coincide. However, in the high supersonic range, the 6.8 mm S-J SC projectile is characterized by a slightly lower coefficient of drag, reaching 0.248 at Mach 2.5, compared to 0.250 for the FMJ.

The values of the drag coefficient calculated for each méplat size and different Mach numbers are presented in Table 5 and graphically in Fig. 14.

Table 5. Calculated drag coefficient – semi-empirical approach

Mach number	Méplat diameter (mm)					
	6.8 mm S-J SC			6.8 mm FMJ SC		
	0.4	0.6	0.8	1.0	1.2	1.4
1.50	0.322	0.319	0.318	0.319	0.320	0.324
1.75	0.301	0.298	0.296	0.298	0.299	0.305
2.00	0.282	0.279	0.277	0.278	0.280	0.287
2.25	0.266	0.263	0.260	0.262	0.264	0.272
2.50	0.254	0.251	0.248	0.250	0.252	0.261
AVG	0.285	0.282	0.280	0.281	0.283	0.290

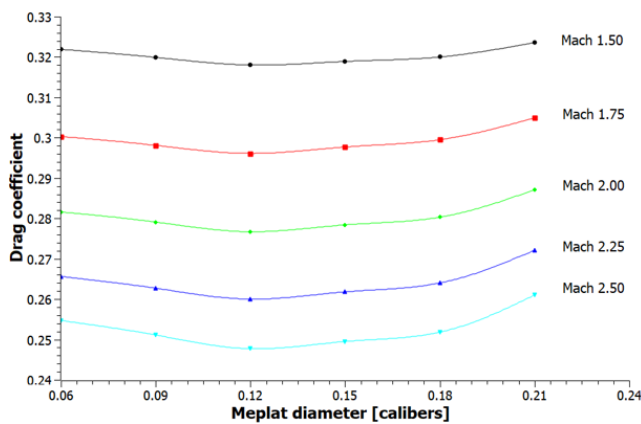


Fig. 14. Calculated drag coefficient versus méplat diameter (semi-empirical approach)

The value of the drag coefficient decreases with the decrease of bullet méplat diameter down to 0.8 mm – 0.12 diameters. The values are lower than achieved with the numerical method, averaging 0.280 for a 0.8 mm diameter. However, both simulations confirm the tendency of achieving the lowest drag with a méplat diameter of approximately 0.12-0.15 calibers.

#### 4. Discussion

The main aim of the paper was to assess the relation between the méplat size of a bullet and the coefficient of drag, to assess a better assembly method for a perspective construction. The characteristics were evaluated with two separate methods, and the results indicate similar conclusions.

Drag dependence of méplat diameter in calibers shown in Fig. 11 and Fig. 14 indicate that there is an improvement in terms of the external ballistic performance of a bullet while reducing the méplat to a value of 0.10-0.15 diameters. Further reduction not only does not decrease the drag acting on a projectile but may even increase it for certain cases. The reason behind this effect might be the wave drag differences due to a different angle between the ogival part of the projectile and the flow direction, which increases with the decrease of the méplat diameter when the ogive length remains unchanged. Charts in Fig. 11 and 14 show that with the increase of the flow velocity, the non-linear relation is stronger – the drag decreases and increases more rapidly at the vicinity of its minimum value for Mach 2.5 than Mach 1.5 and 2.0, which confirms the wave-drag effect explanation. Therefore, in cases of assumed high supersonic bullet flow, the importance of precise and consistent méplat dimensions increases. The relation between the méplat diameter and coefficient of drag value confirms the theory presented in ref. [7].

The use of CFD methods in the estimation of the ballistic characteristics of a bullet is more time and

computationally expensive, however, it provides accurate results. Simulations estimated the value of zero-yaw drag coefficient, as well as the velocity, pressure, and density changes in the fluid, providing the ability to analyze the behavior of air in proximity to the projectile surface. On the other hand, utilizing PRODAS ballistic software provides quick, cost and time-effective results by comparative analysis of the design to a considerable amount of actual rounds data. It is a less accurate method than a CFD analysis, however, it can be a very valuable tool, when used in terms of a preliminary analysis.

#### 5. Conclusions

- To reduce the drag force acting on a 6.8 mm projectile in flight, in case of a set ogive length, a méplat diameter of between 0.8 mm to 1.0 mm should provide the best outcome. Achieving that value with higher precision and repeatability is possible with steel element, so with the reverse-drawn semi-jacketed design of a projectile;
- Designing a bullet with a steel front part provides additional benefits, like increased resistance to damage due to transport, carrying, and weapon operational cycle, which means more consistent performance of the ammunition;

Analyzing the material properties of the designed construction, the following hypothesis can also be stated:

- Semi-jacketed bullet would provide increased terminal ballistics performance, due to a harder material being in immediate contact with the target;
- Design with a steel penetrator outside of the jacket would help to avoid the material wrinkling at the projectile nose due to the lubrication, which causes imbalances and therefore stability issues and is common for standard copper jacketed bullets production;
- Two-material ogival part of the bullet provides the possibility of designing a hybrid ogive shape, with a secant front – steel penetrator shape, turning into a tangent shape of the jacketed part, which would be a further increase in repeatability and constant external performance.

Results from this study provide valuable information concerning the design process of a projectile, in terms of the technique of assembly and the necessity of precision of the bullet's front part. The main conclusion is that the drag dependence on méplat diameter is not constant – reducing the méplat size reduces the coefficient of drag to some point, after

which further diameter reduction is not needed, or even undesirable for certain flow velocities.

The results have strong implications for future bullet designs. Further works should focus on analyzing the projectile external performance dependence on minor damage caused during production and assembly, which may cause irregularities and asymmetries.

### Acknowledgements

The work was financed by Military University of Technology under research project UGB 22 829.

### References

1. Crouch G. I. 2021. "Defence Technology". *Critical interfaces in body armour systems* 17 (6): 1887-1894.
2. NIJ. 2000. *Resistance of Personal Body Armor NIJ Standard-0101.04*, Washington: U.S. Department of Justice, Office of Justice Programs.
3. Frost George. 1990. *Ammunition making*. Washington: National Rifle Association.
4. Official Journal of the European Union. 2021. COMMISSION REGULATION (EU) 2021/57 of 25 January 2021.
5. Piasta Krzysztof, Przemysław Kupidura and Grzegorz Leśnik. 2022. "Projectile for a New Intermediate Cartridge", *Problems of Mechatronics. Armament, Aviation, Safety Engineering* 13 (4) : 123-126.
6. Piasta Krzysztof, Przemysław Kupidura. 2023. "Perspective Armour Piercing intermediate Cartridge Projectile", *Problems of Mechatronics. Armament, Aviation, Safety Engineering* 14 (1) : 89-104.
7. McCoy Robert L. 2012. *Modern exterior ballistics, Revised 2<sup>nd</sup> Edition*. USA: Schiffer Military, s. 32-34, 71.
8. Muruganatham, V. R., Thoma Babin. "Numerical investigation of hybrid blend design target bullets", MATEC Web of Conferences 172 01006.
9. Larson, Eric, Racha Lwali and Dejan Samardzic. 2015. "Bullet Drag Estimation with Compressible Conical Flow Equations and Commercial Software", Department of Aerospace Engineering and Engineering Mechanics, San Diego State University research.
10. Rodriguez Sal. 2019. *Applied Computational Fluid Dynamics and Turbulence Modeling*. Switzerland: Springer Nature, s. 238.
11. DeSpirito James, Karen Heavey. 2004. "CFD Computation of Magnus Moment and Roll-Damping Moment of a Spinning Projectile", AIAA 2004-4713.
12. Ansys Inc. 2021. *Ansys Fluent Theory Guide*. USA: Ansys Inc.
13. Litz Bryan. 2015. *Applied ballistics for long-range shooting*. USA: Applied Ballistics LLC, s. 157-162.
14. Arrow Tech. *Prodas V3 Documentation*.

## SELECTION OF MATERIALS FOR REPAIRING PUNCTURES OF METAL SKIN OF SEMI-MONOCOQUE STRUCTURES USING COMPOSITE PATCHES

### DOBÓR MATERIAŁÓW DO NAPRAW PRZEBIĆ POKRYĆ METALOWYCH STRUKTUR PÓLSKORUPOWYCH Z ZASTOSOWANIEM ŁAT KOMPOZYTOWYCH

Jan GODZIMIRSKI<sup>1</sup> , Marek ROŚKOWICZ<sup>1</sup> , Iga BARCA<sup>1,\*</sup> 

<sup>1</sup> Faculty of Mechatronics, Armament and Aerospace, Military University of Technology, Sylwester Kaliski Street 2, Warsaw, Poland

\* Corresponding author: [iga.barca@wat.edu.pl](mailto:iga.barca@wat.edu.pl)

#### Abstract

For repairing punctures of skin of semi-monocoque structures under field conditions, simple methods are sought to guarantee the reliability of the repaired structure. Therefore, adhesive joints and composite materials are being increasingly used in repairs. During repairs using adhesion, an important aspect that affects the quality of the joint is the selection of the adhesive and the quality of surface preparation of the parts to be joined. This is necessary to get the right bond strength and durability of the joint in working environments characterized by extreme temperatures and exposure to chemicals and moisture. The purpose of the study was to select an adhesive with good strength properties for bonding AW2024T3 aluminum sheets to carbon and glass composites, and to analyze the effect of metal surface preparation on the strength of adhesive joints (grinding, sandblasting and chemical surface preparation). The tests were carried out on overlap (metal-composite) specimens. For selected adhesives, strength tests were also carried out on specimens replicating the repaired damage with a diameter of 20 mm of metal skin repaired by different methods, including composite patches and adhesive joints. The specimens were loaded in tension and loss of stability. The tests made it possible to determine the requirements for composite patches used for repairing upper and lower airframe wing skins.

**Keywords:** repair node, adhesive joints, surface roughness, composite materials, numerical analysis.

#### Streszczenie

Do napraw przebić pokryć konstrukcji półskorupowych w warunkach polowych, poszukuje się prostych metod, które zagwarantują niezawodność naprawianej struktury. Dlatego coraz częściej w naprawach wykorzystuje się połączenia adhezyjne i materiały kompozytowe. Podczas napraw z zastosowaniem klejenia ważnym aspektem, który wpływa na jakość połączenia, jest dobór odpowiedniego kleju oraz jakość przygotowania powierzchni klejonych elementów. Jest to niezbędne do uzyskania odpowiedniej siły wiązania i trwałości połączenia w środowisku pracy, które cechują ekstremalne temperatury oraz narażenie na działanie chemikaliów i wilgoci. Celem badań był dobór kleju o dobrych właściwościach wytrzymałościowych do łączenia blach AW2024T3 z kompozytami węglowymi i szklanymi oraz analiza wpływu przygotowania powierzchni metalowych na wytrzymałość połączeń adhezyjnych (szlifowanie, piaskowanie i chemiczne przygotowanie powierzchni). Badania przeprowadzono na próbkach zakładkowych (metalowo-kompozytowych). Dla wybranych klejów wykonano również badania wytrzymałościowe próbek imitujących naprawione uszkodzenie o średnicy 20 mm pokrycia metalowego naprawianego różnymi metodami, w tym z zastosowaniem łat kompozytowych i połączeń adhezyjnych. Próbki obciążano na rozciąganie i utratę stateczności. Przeprowadzone badania pozwoliły określić wymagania dotyczące łat kompozytowych stosowanych do napraw górnych i dolnych pokryć skrzydeł płatowców.

**Słowa kluczowe:** węzeł naprawczy, połączenia klejowe, chropowatość powierzchni, materiały kompozytowe, analiza numeryczna.



## 1. Introduction

Despite the use of new materials in aircraft manufacturing, the skin of aircraft in service is still made of aluminum alloys [1]. Research is constantly being carried out on the most favorable solutions for repairing defects in primary aircraft structures, including skins, which are most often damaged during operation [2]. The conventional approach to maintaining aircraft structures can be divided into four phases: detection of defects, diagnosis of their nature, prediction of their future behavior and implementation of countermeasures including repairs [3]. With such an approach, it is required to develop and design optimal repairs and evaluate their durability. Repairs to such structures involve cutting a hole to remove the damaged material, placing an insert to fill the hole and attaching a closing patch to support the damaged airframe structure [4].

Two methods of repairing skins are used: using adhesive joints when using composite patches, or using mechanical joints when using metal patches [5]. Due to weight savings [6], the use of classical mechanical fasteners (rivets, screws) to connect composite elements is increasingly minimized, as they cause stress concentrations at the holes [7, 8, 9]. Bonding is one of the most suitable joining technologies in terms of weight reduction and mechanical properties [10]. Adhesive repairs of the secondary bonding type (secondary bonding - joining two cured parts together using a structural adhesive) using certified high-strength epoxy adhesives for repairing aerospace structures, i.e. Loctite 9394 Aero [11], have great potential. Secondary bonding is a comprehensive bonding method because it provides faster assembly, easier handling, lower production costs and provides flexibility in the production cycle. The strength of adhesive bonds used in repairs, among other things, is affected by three main parameters - the type of adhesive selected, the material of the patch and the quality of surface preparation.

In order to make an effective adhesive bond, an optimized bonding system, i.e., the selection of appropriate parameters of substrate/surface/pretreatment/adhesive/primer combination must be selected [12]. The quality of the adhesive bond depends very much on the surface preparation strategy used for joining [13, 14]. The quality of the surface affects the mechanical properties of the interphase adhesion [15]. The mechanical properties of adhesive joints are also influenced by environmental factors such as air humidity, joint working temperature, joining process and curing cycle parameters [16]. Due to the reactivity of freshly prepared surfaces and the proximity and activity of contaminants in the environment, cleaning

these surfaces sufficiently to achieve reliable adhesive bonds can be particularly difficult under field conditions [17]. The most commonly used method of surface preparation under field conditions is grinding using specialized abrasive fabric for metal surfaces [18]. Metal surfaces require more surface treatment than composite materials and most often have poor interphase adhesion mechanical properties, which can be a reason for damage initiation [19].

During repairs, a patch is bonded to restore the primary strength of the damaged structure. For this purpose, patches made of carbon or glass composites infused with epoxy resin are used [20]. They are usually laid in such a way as to achieve quasi-isotropic characteristics, which is extremely important in the repair of aircraft structures [21]. In addition, the material parameters must be properly selected so that the repair node is characterized by sufficient strength. Also important is the condition of local "not stiffening" of structural elements as a result of the repairs performed, as this can cause additional stresses around the repair node [22, 23] and cause additional stress concentrations in the adhesive bond [24].

The purpose of the study was to determine the effect of surface preparation on the strength of secondary bonding when joining metal parts made of EN AW-2024-T3 aluminum alloy and composite parts made of CFRP and GFRP composites. In addition, the selection of the most favorable geometric parameters of patches when repairing metal structures and different methods of metal surface preparation were analyzed, using patches made of GFRP composite with different thicknesses. There is little research on secondary bonding using composite overlays made of fabrics infused with epoxy resin, mainly studies are performed on prepregs. Above that, an analysis was made of modern methods of surface preparation for bonding using the most advanced methods applicable in the industry, using chemical surface preparation.

## 2. Experimental studies

The purpose of the study was to determine the effect of surface preparation on the strength of adhesive joints, and to select the most favorable technological repair parameters (surface preparation method and patch geometry).

### 2.1. Overlap specimens - adhesive selection and surface preparation methods

The first part of the study was the selection of an adhesive for the repairs. Tests were carried out on metal-composite overlap specimens 20x12,5x2 mm (width/length/thickness) (Fig.1) made of EN AW-2024-T3 aluminum alloy and carbon/glass fiber-reinforced composites (CFRP and GFRP). The carbon

composite used is GG204T 2 x 2 Twill 3K fabric in the form of prepreg saturated with IMP503 46 epoxy resin.

The glass composite, on the other hand, is a 110g/m<sup>2</sup> fabric saturated with L285/H285 epoxy resin. Four adhesives were used for the bonding overlap specimens: L285/H285 (aerospace certificate resin), Epidian 57/Z1, DP420 and Loctite 9464. The

characteristics of the adhesives are shown in the Table 1. All adhesives are two-component, they were mixed on a Teflon plate at room temperature in proportions according to the manufacturer's instructions (Table 1). After mixing, the adhesives were applied with a sterile wooden stick.

Table 1. Characteristics of the used adhesive

Adhesive name	Resin - chemical type	Hardener - chemical type	Mass ratio (resin/hardener)	Course of curing	Shear strength [N/mm <sup>2</sup> ]	Peel strength [N/mm]
L285/H285	Epoxy	Amine	100:40	24h at 23°C + 15h at 60°C	-	-
Epidian 57/Z1	Epoxy	Amine	100:10	24h at 23°C + 5h at 80°C	15.0	-
Loctite 9464	Epoxy	Amine	1:1	3 days at 23°C	18.2	7.00
DP420 3M	Epoxy	Amine	2:1	24h at 23°C	31.0	8.76

Before bonding, in first part of tests the joined surfaces of the specimens were washed with extraction gasoline then grinded with 3M abrasive fabric number 80 using a pneumatic gun at 1000 rpm for 60 seconds, designed for aluminum surfaces, and then washed with extraction gasoline. Threads were used to obtain a 0.15-mm-thick adhesive layer. The tool shown in the figure 2 was used to obtain adhesive layer with the same overlap lengths of 12.50 mm. All specimens were loaded equally at the same time with a force 1.2 MPa. In each case, the manufacturer's recommended process was used to cure the adhesive. The specimens were subjected to tensile testing on a testing machine and the results are shown in Table 2. Confidence intervals were also determined using the Student's t method (1)(2) - Figure 3.

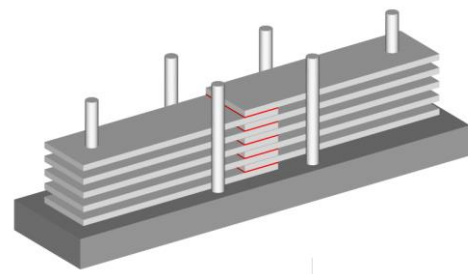


Fig. 2. The tool in which the specimens were placed in order to obtain a given weld length

$$n = 6 - \text{number of specimens}$$

$$\bar{X} = \frac{\sum_{i=1}^n n_i}{n} \tag{1}$$

$$SD = \sqrt{\frac{\sum_{i=1}^n n_i^2 - \bar{X}^2}{n * (n - 1)}} \tag{2}$$

$$t_\alpha = 2,571 - \text{Student's } t - \text{ratio for 6 specimens}$$

$$TS = SD * t_\alpha \tag{3}$$

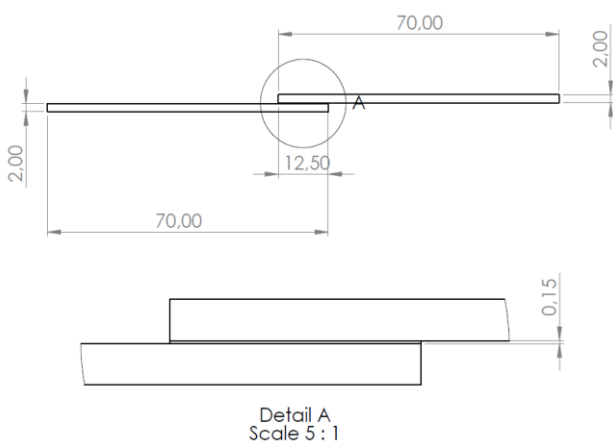


Fig.1. Geometric dimensions of lap specimens

The joints prepared with 3M's DP420 adhesive had the highest load capacity.

In order to determine the surface preparation method that provides the highest load capacity for the joint, additional tests were carried out for aluminum-carbon lap specimens. The adhesive that had the highest shear strength in previous tests was used. Two additional methods of surface preparation for bonding were tested: sandblasting (using F80 electrocorundum grains at an operating pressure of 8 at. And cleaning before and after with extraction gasoline), and grinding and using a primer (Surface pre-treatment

Table 2. Load capacity of overlap joints for different thermoplastics materials

Specimen no.	Load capacity [N]							
	AW 2024T3-CFRP				AW 2024T3-GFRP			
	L285/H285	Epidian 57/Z1	DP420	Loctite 9464	L285/H285	Epidian 57/Z1	DP420	Loctite 9464
1	1351	2253	3718	3000	871	2395	3463	3000
2	983	2240	3487	2850	846	2640	2197	2659
3	1185	1795	3852	3000	1641	2715	3378	2210
4	1113	1937	2805	2590	684	1709	2336	2252
5	1523	1493	3497	2790	493	3082	2480	2694
6	760	1429	3280	-	795	2702	1797	-
Average load capacity	1152±282	1858±372	3440±387	2846±212	888±413	2540±486	2608±590	2563±410

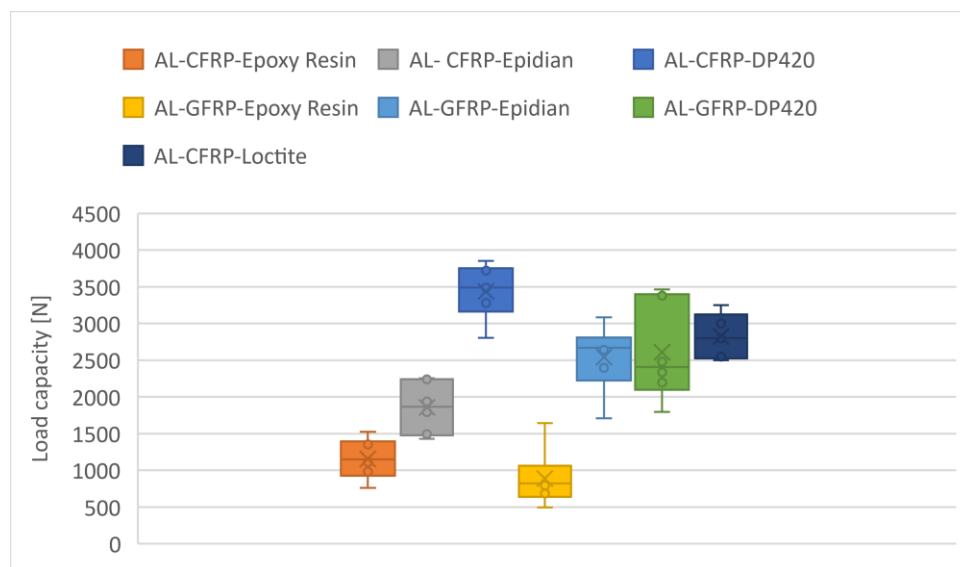


Figure 3. Arithmetic averages of overlap joints load capacity

AC-130-2 Kit from 3M). The two-component primer was mixed at a volume ratio of 49.2:1 ml. After mixing it for 60 s and leaving it for 30 min, it was applied to the grinded and cleaned surface (extraction gasoline) with a brush. It was left on the surface for 5 min,

according to the manufacturer's instructions. The samples were then bonded together after 60 min after evaporation of the product. The results of the overlap joint load capacity tests are shown in Table 3. Confidence intervals were also determined - Figure 4.

Table 3. Bearing capacity of overlap joints for different surface preparation methods

Specimen no.	AW 2024T3-CFRP		
	DP420		
	Grinding	Sandblasting	Grinding + Primer
1	3718	6180	6387
2	3487	5425	6917
3	3852	5507	5820
4	2805	6050	5485
5	3497	5853	6103
6	3280	5990	5773
Average Load capacity [N]	3440.00±387.00	5834,17±320.18	6080.83±537.50

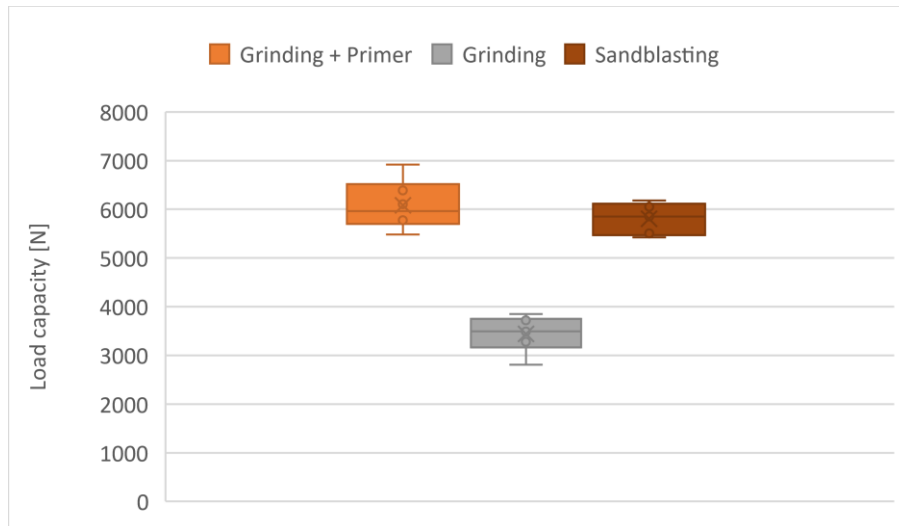


Figure 4. Arithmetic averages of overlap joints load capacity

The use of primer for surface preparation increased the load capacity of the joint by about 57%. An example of a damaged specimen after testing is shown in figure 5. In each case, the composite was damaged by delamination.

Specimens whose surfaces were grinded before bonding and treated with primer at the same time have the highest load capacity.



Fig. 5. The specimen after the strength test

**2.2. Specimens with a hole - the effect of patch thickness and surface preparation on the strength of overlay joints**

Tests in this field were carried out for aluminum (AW 2024T3) specimens with a laser-cut hole (the hole was assumed to be equivalent to the damage to the skin) with the dimensions shown in Figure 6. The specimens were in the form of overlay joints with a circular composite patch (GFRP 110 g/m<sup>2</sup>) with a diameter of 70 mm and three different thicknesses

(1 mm, 1.6 mm and 2 mm) and quasi-isotropic properties. Three specimens were prepared for each surface preparation method and patch thickness. A 19.9 mm diameter insert made of aluminum alloy was placed in the hole. In this case also, three methods of surface preparation were used: grinding, grinding + primer and sandblasting. The specimens were subjected to tension on an MTS series 809 tensile machine - Table 4 – the results were averaged. The undamaged and damaged specimen (without repair) were also tested.

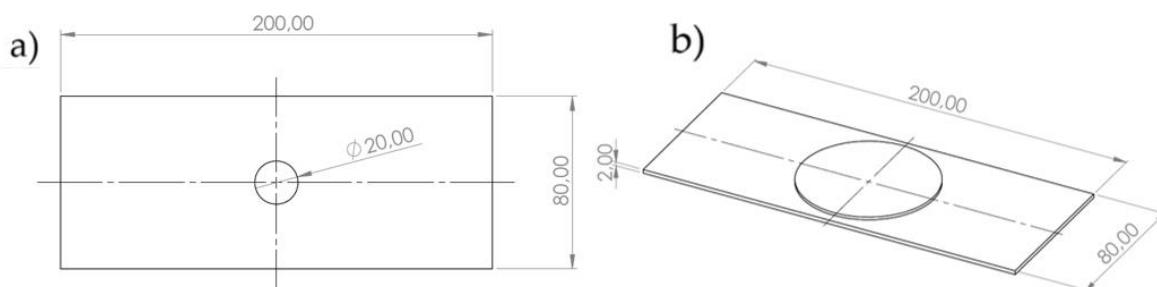


Fig. 6. Geometric dimensions of: a) the plate with a hole, b) repaired specimens

Table 4. Static test results for specimens with repair node

Specimen no.	Kind of specimen	Thickness	Method of Surface preparation	Force [kN]
1	Undamaged	-	-	69,3
2	Damaged	-	-	50
3	Repaired	1 mm	Grinding	49,5
4			Grinding + Primer	51,5
5			Sandblasting	52
6		1.6 mm	Grinding	61,5
7			Grinding + Primer	61,5
8			Sandblasting	60
9		2 mm	Sandblasting + primer	62,5
10			Grinding	58
11			Grinding + Primer	63,5
12			Sandblasting	59

Figure 7 shows examples of patch failure for different thicknesses (1 mm, 1.6 mm and 2 mm) for specimens whose surfaces were grinded before bonding and then primer was applied. In the case of the specimen with a 1 mm thick patch, it cracked together with the specimen (a). The specimen with

a 1.6-mm-thick patch cracked and then loaded the patch, which partially disrupted (b). On the other hand, the specimen with a 2-mm-thick patch experienced delamination of the composite overlay during specimen cracking (c).

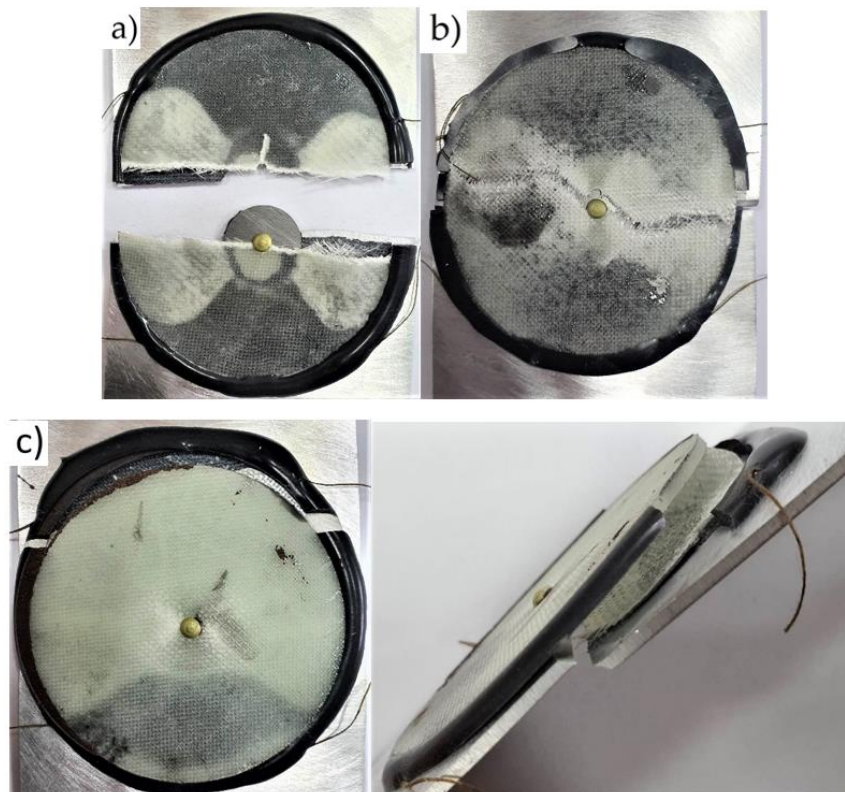


Fig. 7. Examples of patch damage during testing: 1 mm (a), 1.6 mm (b), 2 mm (c)

The use of primer increased the strength of the applied joint by only about 4%. The highest strength was characterized by specimens that used 2 mm thick

overlays with a surface prepared by grinding and primer. In neither case was adhesive failure observed - detachment of the patch from the repaired surface.

### 2.3. Surface roughness

In order to check the effect of the primer (AC-130-2 Surface Pretreatment Kit) on the geometric parameters of the surface of the aluminum sheet under study, the surface roughness was measured using a VHX-6000 Keyence optical microscope, at 500x

magnification, and five specimens whose surfaces were prepared using five methods (Figure 8).

Figures 9-11 show the surfaces of the prepared specimens without primer (a) and with (b).



Fig. 8. Surface roughness test specimens prepared by the following methods (from left): primer, grinded, grinded + primer, sanded, sanded + primer

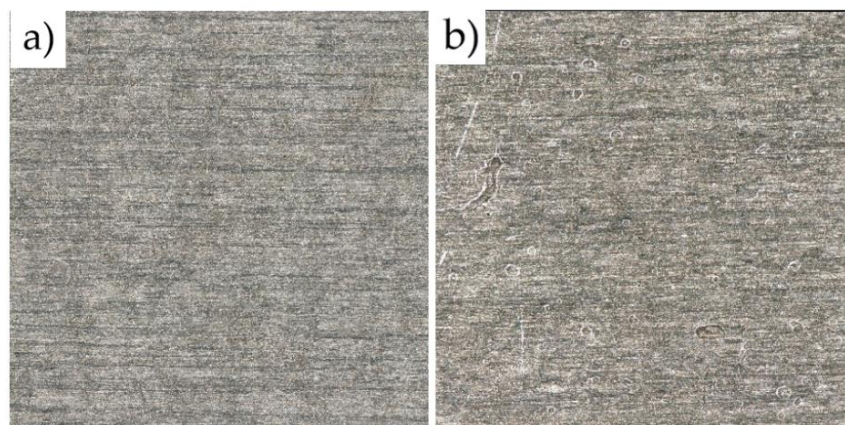


Fig. 9. The surface of the specimen without surface preparation (a) and after using primer (b)

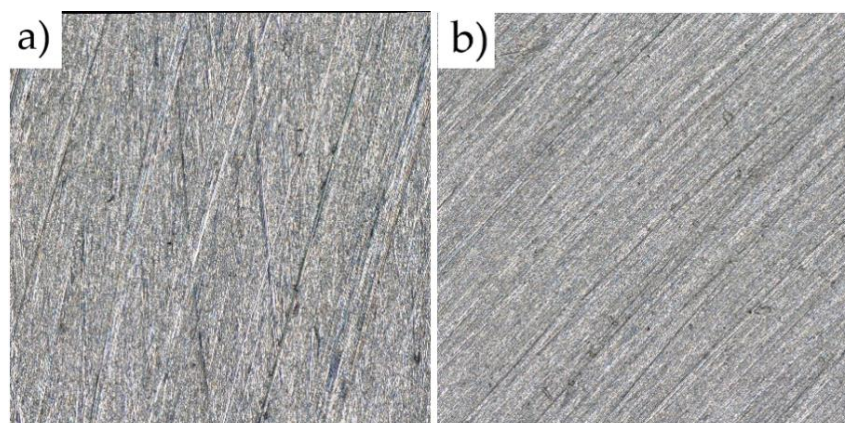


Fig. 10. Surface grinded with abrasive cloth No. 80 from 3M (a) and sanded and washed with primer (b)

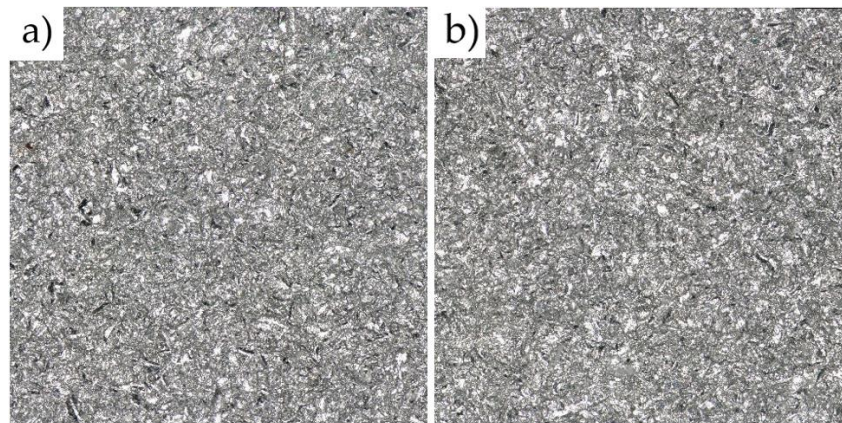


Fig. 11. Surface grinded with abrasive fabric No. 80, 3M (a) and grinded and washed with primer (b)

Surface roughness measurements were also carried out on an optical microscope for all specimens shown in the figures. Two measurements were taken for each surface preparation method. Four parameters were measured, using two methods: measurement on the line- R (Fig. 12); measurement on the surface - S (Fig. 13):

- Ra - the arithmetic mean deviation of the profile from the mean line,

- Rz - surface roughness according to the five points of the profile on the line,
- Sa - arithmetic mean deviation of the profile from the mean plane,
- Sz - surface roughness according to five points of the profile on the plane.

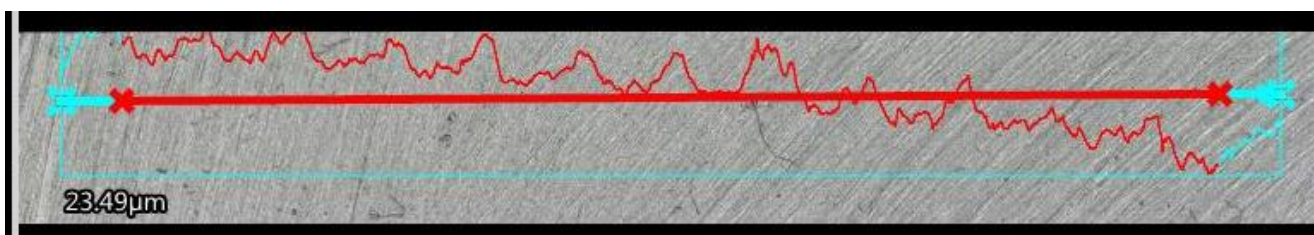


Fig. 12. Method of determining surface roughness on the line

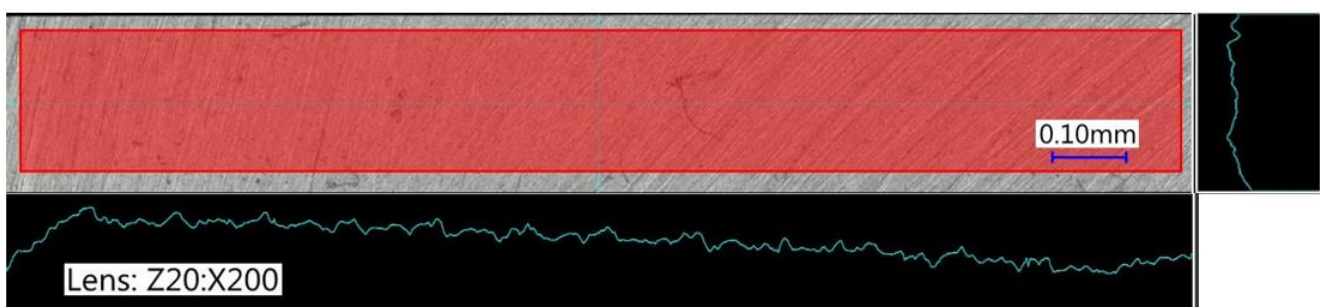


Fig. 13. Method of determining surface roughness on a surface

The surface roughness is not constant over the entire surface of the specimens which is related to the manual surface preparation process. The measurement values are shown in Table 5.

It can be observed that surfaces on which primer has been applied are smoother - they are characterized

by less surface roughness. Primer gets into the recesses, leveling out material defects and easing the even distribution of adhesive layer over the entire surface.

Table 5. Surface roughness measurement values

Specimen no.	Surface preparation method	Ra [ $\mu\text{m}$ ]	Rz [ $\mu\text{m}$ ]	Sa [ $\mu\text{m}$ ]	Sz [ $\mu\text{m}$ ]
1	None	3.11	18.72	3.66	35.58
2	Primer	3.12	16.43	3.84	23.17
3	Grinding	6.13	35.92	6.62	69.72
4	Grinding + Primer	7.83	43.07	8.64	58.40
5	Sandblasting	11.37	53.58	13.80	92.68
6	Sandblasting + Primer	11.56	55.87	13.72	93.93

### 3. Numerical simulations

In order to analyze the stress distribution in a specimen with a hole without and after repair, numerical simulations were performed using the CAE program Ansys Workbench 2021R2. The *Static Structural* calculation module was used for this.

The *Engineering Data* program library was used to define material properties. The parameters of three materials were used for the simulation, which are

shown in Tables 6 and 7. The given nonlinear properties of the aluminum alloy of the plate and the adhesive were defined as multilinear and bilinear, respectively. The parameters of the glass composite were defined as orthotropic properties. The material data were determined experimentally using a specimen of the experimental material. For the purpose of calculation the properties of the material was homogenized.

Table 6. Material parameters in the nonlinear range of each material

Material name	Young's Modulus [GPa]	Poisson's Ratio [-]	Yield Strength [MPa]	Tangent Modulus [MPa]	Plastic Strain [-]	Stress [MPa]
AW 2024T3 NL	71.000	0.3	-	-	0	330.00
					0.0098	348.45
					0.0196	370.00
					0.0385	410.80
					0.0741	468.72
					0.1071	507.36
0.1379	540.56					
DP 420	2.083	0.35	24.00	325.00	-	-

Table 7. Material parameters of orthotropic glass composite

Material name	Young's Modulus [GPa]			Poisson's Ratio [-]			Shear Modulus [GPa]			
	Direction	X	Y	Z	XY	YZ	XZ	XY	YZ	XZ
Glass composite		15	15	5	0.04	0.3	0.3	3	2.2	2.2

In the *Geometry* module, the geometry of the specimen model was defined (Fig. 14). The model consists of an 80x150x2 mm (width, length, thickness) element with a 20 mm diameter hole - the defined specimen is shorter than the specimen used in the experiment due to the fact that the surface of the specimen located in the jaws of the testing machine of the clamping area of the grips was not included. An insert was modeled in the hole with dimensions 19,9 mm. A adhesive joint with a diameter of 70 mm and a thickness of 0.12 mm and a composite patch with a diameter of 70 mm and a thickness of 2 mm were also modeled.

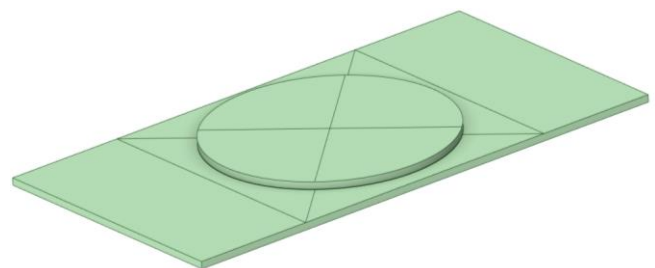


Fig. 14. Repair node model in the Geometry module

Using the *Contacts* function, the types of contacts occurring between the various elements of the model were defined to replicate the relationships that exist

between them. *Frictional* type contacts with a factor of 0.1 were defined between the insert and the plate - Fig. 15. *Bonded* type contacts were defined between the adhesive and the patch, the adhesive and the plate, and the adhesive and the insert - Fig. 16.

Discretizations of the model were performed using the Mesh function. In the mesh parameters for the entire model, the Mesh elements were given a size of 2 mm. The Multizone function with Hexa properties was used to define the type of mesh elements, which defines a hexagonal mesh type for the model. The Edge Sizing function was also used, and an element size of 1 mm was set at the edge of the hole - Fig. 17. After the geometry was discretized, a model consisting of 4289 elements and 31162 nodes of Hex20 type was obtained. The computational mesh is shown in Fig. 18.

The quality of the mesh near the hole was checked using the Element Quality function. The results of the analysis are shown in Fig. 19. The analysis of the quality of the mesh shows that it is correctly defined. Elements with values close to unity define the best quality of the computational mesh.

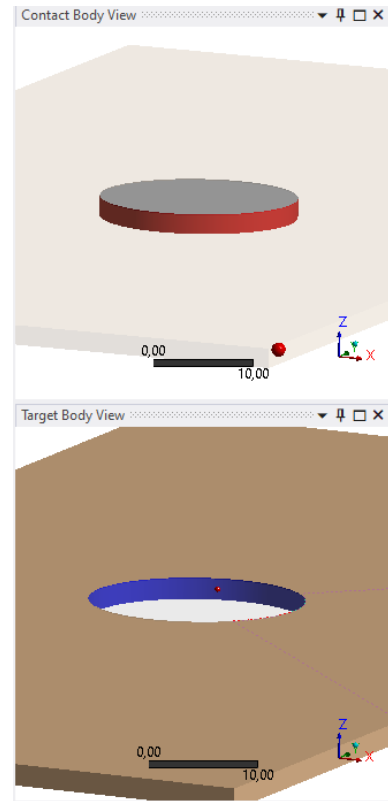


Fig. 15. Example of Frictional type of contact: insert-plate

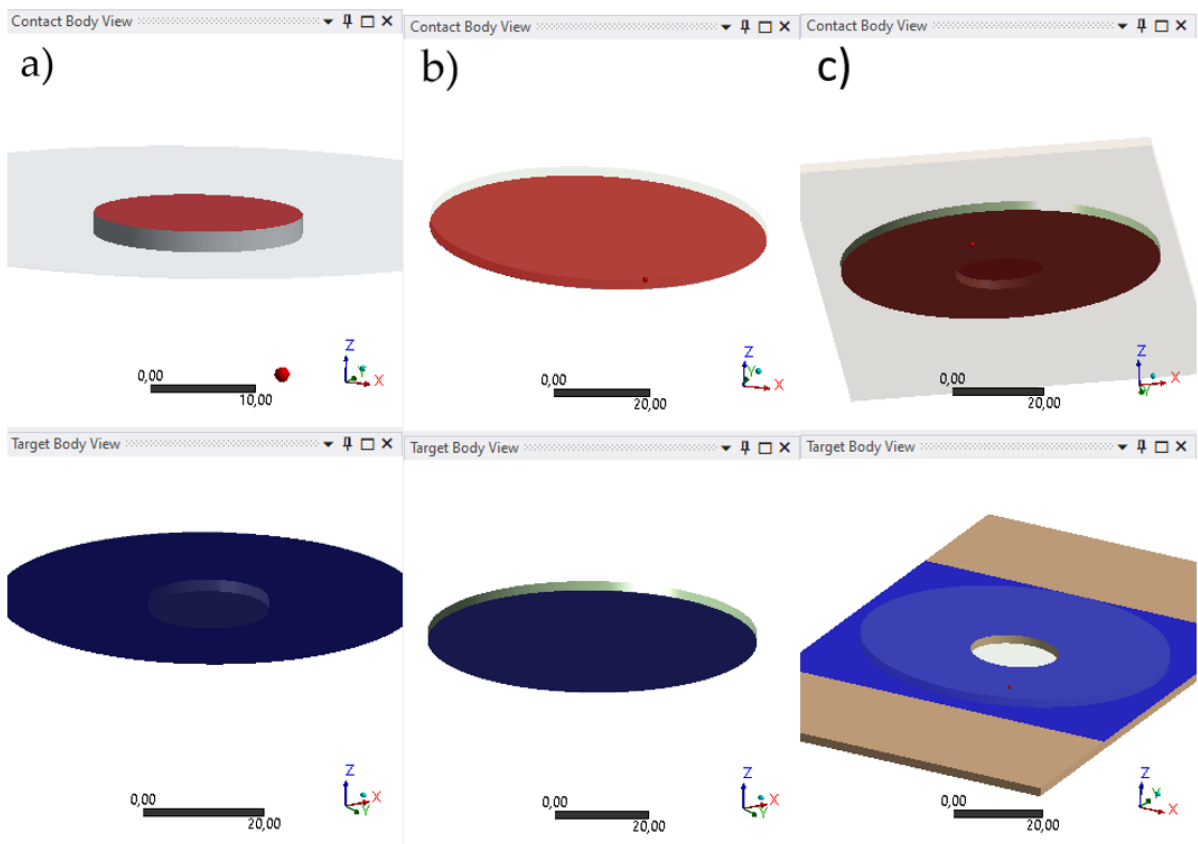


Fig. 16. Examples of Bonded type of contact: insert-adhesive (a), adhesive-bonded (b), adhesive-plate (c)

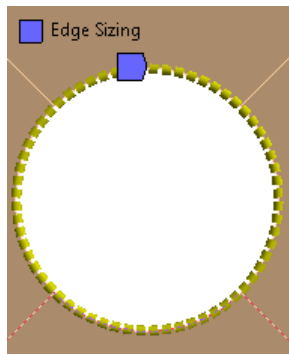


Fig. 17. Using the Edge Sizing function to thicken the mesh around the hole

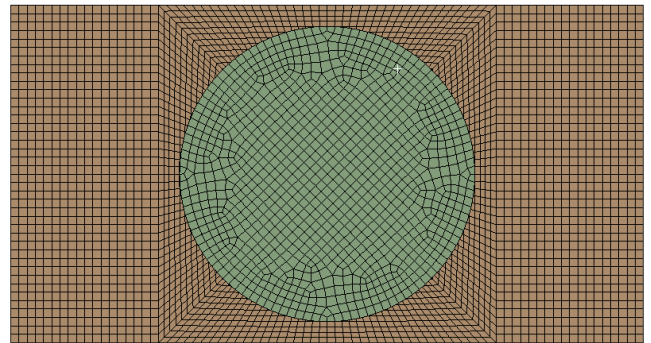


Fig. 18. Discretized numerical model

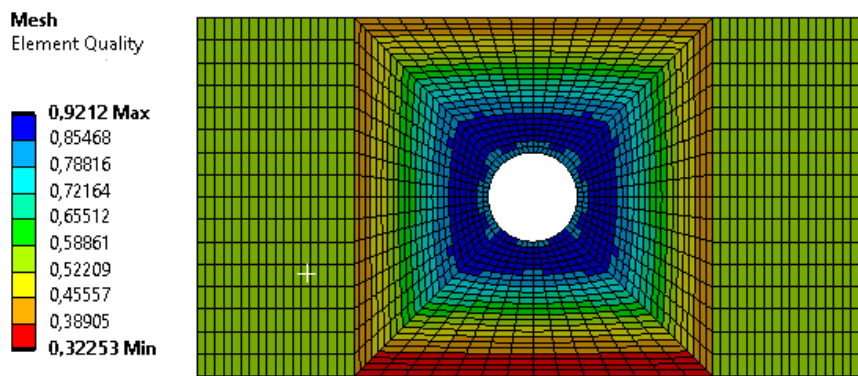


Fig. 19. Quality analysis of mesh elements around the hole

The boundary conditions were given using the *Static Structural* function. The computational model replicates the loading conditions of the specimen in the testing machine - Fig. 20. One side - was fixed using the *Fixed Support* function. All six degrees of freedom were taken away from the nodes -  $D_X; D_Y; D_Z = 0$ ,

$R_X; R_Y; R_Z = 0$ . For the second side, a *Force* load of 60 kN in the Y direction was defined. The value of the destructive force of such a specimen was determined in the experimental part. The second side was also fixed using the *Displacement* function on two directions -  $D_X; D_Z = 0; D_Y = Free$ .

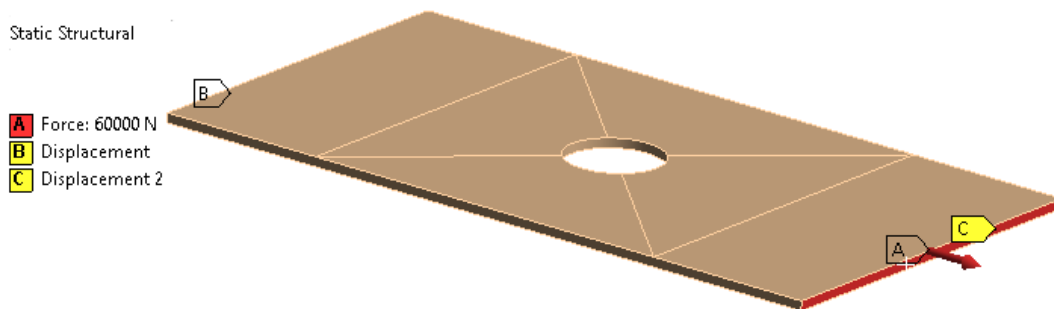


Fig. 20. The boundary conditions of the model (A - force, B and C - restraint)

**Simulation results**

Strength calculations were performed using the *Solution* function. The *von-Mises* stress in the repair plate is shown in Fig. 21. The largest *Equivalent Plastic Strain* in the model has a value of 0.247 and occurs around the hole in the adhesive layer - Fig. 22.

Analyzing the reduced *von-Mises* stresses in the adhesive bond - Fig. 23 - the occurrence of stress concentration phenomenon and failure stresses of the adhesive layer was observed in the vicinity of the hole. The distribution of *von-Mises* stresses in the patch is shown in Fig. 24.

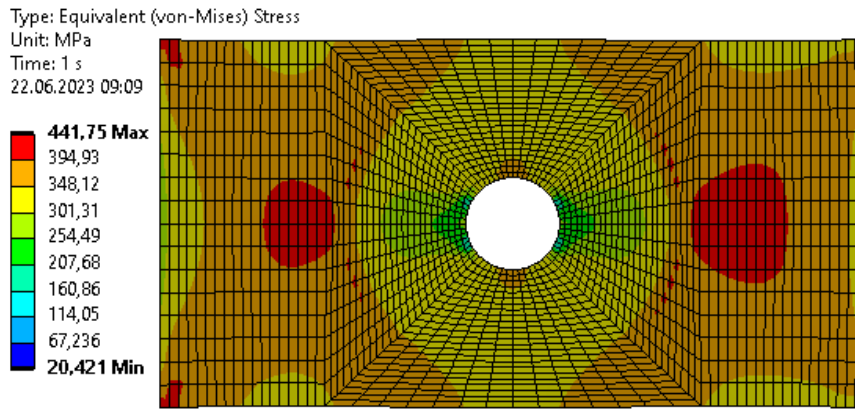


Fig. 21. Von-Mises stress map - plate

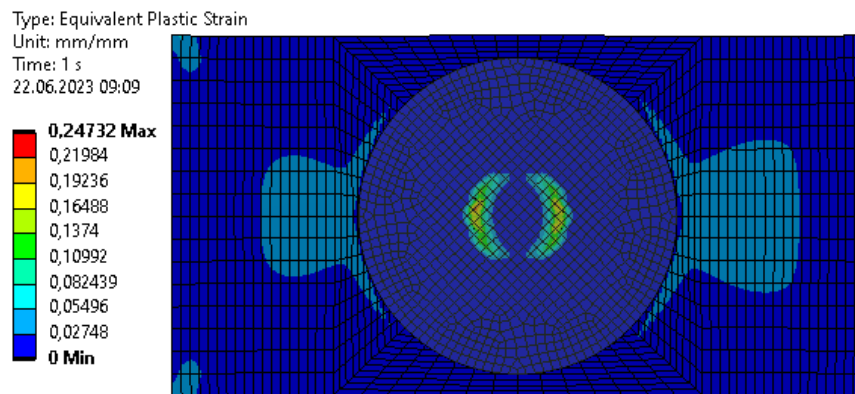


Fig. 22. Equivalent Plastic Strain map of the model

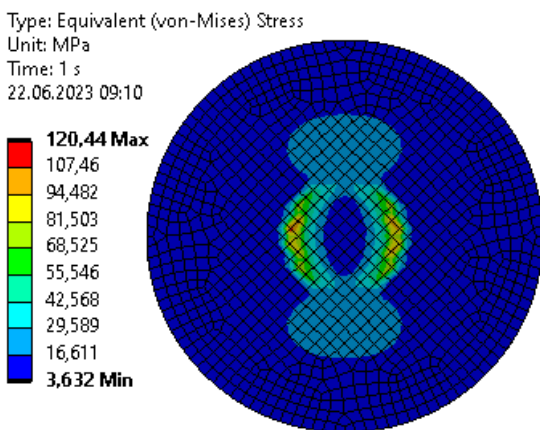


Fig. 23. Von-Mises reduced stress map – adhesive layer

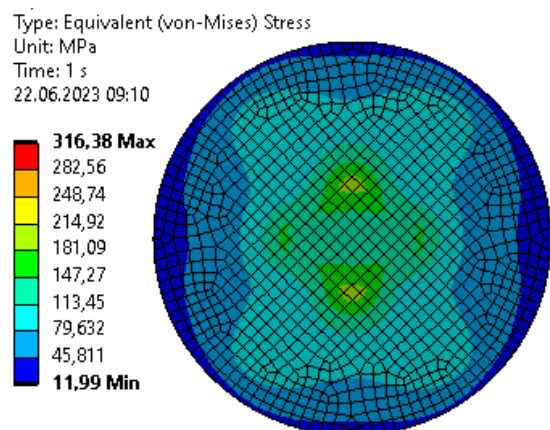


Fig. 24. Von-Mises reduced stress map - patch

Calculations were also carried out for a plate with a hole without a repair. The material parameters, geometry and boundary conditions are analogous to the previous model. The load for this design case is equal to 50 kN (the value obtained from experimental tests) (Fig. 25).

Table 8 summarizes the obtained results of the numerical analyses.

Analyzing the obtained results, a decrease in stresses in the plate was observed after the repair. In the adhesive layer, there are stresses with values exceeding the cohesive strength of the adhesive - which may indicate the destruction of the joint in the original construction.

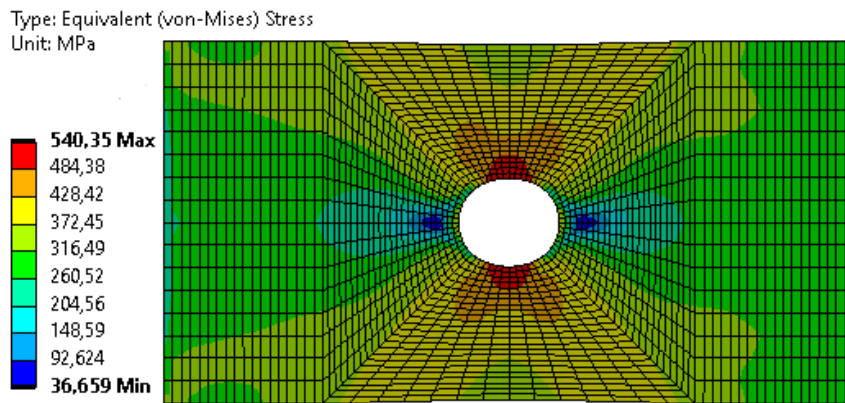


Fig. 25. Von-Mises stress map for the damaged plate

Table 8. Results of numerical simulations for two models (maximum value of Von Mises stresses)

Model type	Von-Mises [MPa]		
	Plate	Patch	Adhesive layer
Damage	540.35	-	-
Repaired	441.75	316.38	120.44

#### 4. Conclusions

Based on the experimental tests and numerical simulations, the following conclusions were defined:

In order to prepare an effective repair node, it is necessary to select, among other things, a suitable adhesive and a method of preparing the surfaces to be joined. In our study, the most favorable results were obtained by preparing the surface by grinding and then using primer. After using primer, the load capacity of lap joints increased by 57%.

The study showed that the use of primer also affects the surface roughness. The parameters defining surface roughness after primer use are lower which is due to the filling of cavities in the material. Too much surface roughening is unfavorable because it lowers the contact area between the adhesive and the material.

Composite surfaces have potentially higher adhesion than surfaces of metal parts. By using an effective method to prepare the surface of the metal part for bonding, a solution can be obtained in which the adhesive strength of the joint is higher than the cohesive strength of the composite part.

Based on numerical calculations, it was found that the use of an adhesive overlay significantly reduces the phenomenon of stress concentration around the hole.

#### Bibliography

1. Starke E.A. Jr., Staley J.T. 2011. Chapter 24: Application of modern aluminum alloys to aircraft. *Fundamentals of Aluminium Metallurgy. Production, Processing and Applications*. Pages 747-783. Woodhead Publishing Series in Metals and Surface Engineering.
2. Baker Alan A., Wang John. 2018. Chapter 6: Adhesively Bonded Repair/Reinforcement of Metallic Airframe Components: Materials, Processes, Design and Proposed Through-Life Management. *Aircraft Sustainment and Repair*. Pages 191-252. Butterworth Heinemann.
3. Baker Alan A., Jones Rhys A.C. 2012. "Bonded Repair of Aircraft Structures". *Springer Science & Business Media*.
4. Baker A.A. 2002. Chapter 1: Introduction and Overview. *Advances in the bonded composite repair of metallic aircraft structure – Volume 1*. Pages 1-18.
5. Shang X., Marques E.A.S., Machado J.J.M., Carbas R.J.C., Jiang D., da Silva L.F.M. 2019. "Review on techniques to improve the strength of adhesive joints with composite adherends". *Composite Part B: Engineering* 177.
6. Kweon J.H., Jung J.W., Kim T.H., Choi J.H., Kim D.H. 2006. "Failure of carbon composite-to-aluminum joints with combined mechanical fastening and adhesive bonding". *Composite Structures* 75: 192–198.
7. Jeevi G., Nayak S.K., Abdul K.M. 2019. "Review on adhesive joints and their application in hybrid composite structures". *Journal of Adhesion Science and Technology* 33 (14).
8. Zitoune R, Collombet F. 2007. "Numerical prediction of the thrust force responsible of delamination during the drilling of the long-fibre composite structures". *Composite Part A: Applied Science and Manufacturing* 38: 858–866.
9. Davim J.P., Reis P., Antonio C.C. 2004. "Drilling fiber reinforced plastics (FRP) manufactured by hand lay-up: influence of matrix (Viapal VUP 9731 and ATLAC 382-05)". *Journal of Materials Processing Technology* 155–156 : 1828–1833.
10. Kupski J., Teixeira de Freitas S. 2021. "Design of adhesively bonded lap joints with laminated CFRP adherends: Review, challenges and new opportunities for aerospace structure". *Composite Structures* 268 : 113923.

11. Yudhanto A., Alfano M., Lubineau G. 2021 “Surface preparation strategies in secondary bonded thermoset-based composite materials: A review”. *Composites Part A: Applied Science and Manufacturing* 147 : 106443.
12. Gary C.W. 2021. Chapter 4: Surface pretreatments for optimized adhesive bonding. *Adhesive Bonding (Second Edition) Science, Technology and Applications. Woodhead Publishing Series in Welding and Other Joining Technologies*. Pages 109-132.
13. Loutas T.H., Sotiriadis G., Bonas D., Kostopoulos V. 2019. “A statistical optimization of a green laser-assisted ablation process towards automatic bonded repairs of CFRP composites”. *Polymer Composites* 40 (8).
14. Dillingham R.G., Oakley B.R., Dan-Jumbo E., Baldwin J., Keller R., Magato J. 2014. “Surface treatment and adhesive bonding techniques for repair of high-temperature composite materials”. *Journal Composite Materials*, 48 (7).
15. Baker A.A., Jonse R. 2002. “Advances in the bonded composite repair of metallic aircraft structure. Volume 1”. *Elsevier Applied Science Publishers*.
16. Banea M.D., Da Silva L.F. 2009. Adhesively bonded joints in composite materials: an overview. *Proceedings of the Institution of Mechanical Engineers, Part L: Journal of Materials: Design and Applications* 223:1–18.
17. Dillingham R.G. 2013. “Qualification of surface preparation processes for bonded aircraft repair”. *BTG Labs*. 2013.
18. Hamill L., Nutt S. 2018. “Adhesion of metallic glass and epoxy in composite-metal bonding”. *Composites Part B: Engineering* 134, Pages 186-192.
19. Li S., Sun T., Liu Ch., Yang W., Tang Q. 2018. “A study of laser surface treatment in bonded repair of composite aircraft structures”. *The Royal Society Publishing* 18 (3).
20. Chester R. 2002. Chapter 2: Materials Selection and Engineering. *Advances in the bonded composite repair of metallic aircraft structure – Volume 1*. Pages 19-40.
21. Andrew J.J., Srinivasan S.M., Arockiarajan A. 2019. “Influence of patch lay-up configuration and hybridization on low velocity impact and post-impact tensile response of repaired glass fiber reinforced plastic composites”. *Journal Composite Materials*, 53 (1), pp. 3-17.
22. Zhou W., Ji X., Yang S., Liu J., Ma L. 2021. “Review on the performance improvements and non-destructive testing of patches repaired composites”. *Composite Structures* 263. 113659.
23. Yala A.A., Megueni A. 2009. “Optimisation of composite patches repairs with the design of experiments method”. *Materials and Design* 30 (1), pp. 200-205.
24. Bouanani M.F., Benyahia F., Albedah A., Aid A., Bouiadjra B., Belhouari M., Achour T. 2013. “Analysis of the adhesive failure in bonded composite repair of aircraft structures using modified damage zone theory”. *Materials and Design* 50, pp. 433-439

## DISPOSABLE PERSONAL PROTECTIVE EQUIPMENT VENDING MACHINE

### AUTOMAT VENDINGOWY DO SPRZEDAŻY JEDNORAZOWEJ ODZIEŻY OCHRONNEJ

Tomasz SAMBORSKI<sup>1,\*</sup> , Andrzej ZACHARSKI<sup>2</sup> , Andrzej ZBROWSKI<sup>3</sup> ,  
Miroslaw MROZEK<sup>4</sup> , Stanislaw KOZIOL<sup>5</sup> , Margaret HALLER de HALLENBURG<sup>6</sup>

<sup>1</sup> Łukasiewicz Research Network – Institute for Sustainable Technologies, ul. K. Pułaskiego 6/10, 26-600 Radom, Poland, e-mail: tomasz.samborski@itee.lukasiewicz.gov.pl, t.: 48 3649232.

<sup>2</sup> Łukasiewicz Research Network – Institute for Sustainable Technologies, ul. K. Pułaskiego 6/10, 26-600 Radom, Poland, e-mail: andrzej.zacharski@itee.lukasiewicz.gov.pl, t.: 48 3649359.

<sup>3</sup> Łukasiewicz Research Network – Institute for Sustainable Technologies, ul. K. Pułaskiego 6/10, 26-600 Radom, Poland, e-mail: andrzej.zbrowski@itee.lukasiewicz.gov.pl, t.: 48 3649306.

<sup>4</sup> Łukasiewicz Research Network – Institute for Sustainable Technologies, ul. K. Pułaskiego 6/10, 26-600 Radom, Poland, e-mail: mirosław.mrozek@itee.lukasiewicz.gov.pl, t.: 48 3649362.

<sup>5</sup> Łukasiewicz Research Network – Institute for Sustainable Technologies, ul. K. Pułaskiego 6/10, 26-600 Radom, Poland, e-mail: stanislaw.koziol@itee.lukasiewicz.gov.pl, t.: 48 3649290.

<sup>6</sup> Biovalley Cooperative, ul. Złota 9, 00-019 Warsaw, Poland, e-mail: m.haller@biovalley.pl

\* Corresponding author: tomasz.samborski@itee.lukasiewicz.gov.pl

#### Abstract

The article presents the concept and structure of a prototype of a vending machine that can dispense disposable personal protection equipment (PPE) or other products with similar physical properties (size, weight) to be used in outpatient clinics, hospitals or beauty parlours, where special and effective protection against pathogens is required, particularly during the pandemic. Due to the difficult-to-predict and unspecified technical and on-site conditions for the installation and use of the device, the authors wanted to achieve autonomy by using a replaceable battery as a power source and large storage capacity of a product rack, at a limited size of the device. The machine operates on a contactless payment system (credit/debit card or NFC mobile payments) – to buy a gown, a customer just has to tap or wave their card on or over the card reader installed in the front wall of the cabinet. Purchased products are dispensed automatically, once the transaction has been approved. The vending machine is also equipped with a removable dispenser to better manage any waste generated. The prototype was comprehensively tested in accordance with the developed verification methodology, in cooperation with an entity interested in implementing the device.

**Keywords:** vending machine, disposable personal protective equipment, reliability, control.

#### Streszczenie

Publikacja przedstawia koncepcję oraz budowę prototypowego urządzenia (automatu vendingowego) do samoobsługowej sprzedaży jednorazowej odzieży ochronnej lub innych produktów o podobnych cechach fizycznych (wymiar, masa) dedykowanego do zastosowań w przychodniach, szpitalach, gabinetach kosmetycznych, gdzie wymagana jest szczególna i skuteczna ochrona przed patogenami, zwłaszcza w okresach nasilonego narażenia epidemicznego. Ze względu na trudne do przewidzenia i nieokreślone warunki techniczne i lokalowe instalacji i użytkowania urządzenia, celem autorów było uzyskanie autonomiczności dzięki zasilaniu elektrycznemu z wymiennego akumulatora i dużej pojemności magazynka urządzenia przy ograniczonych gabarytach. Zastosowano terminal realizujący płatności bezgotówkowe oraz automatyczne wydawanie odzieży po ich zaakceptowaniu. Wbudowano wymienny zasobnik ułatwiający zagospodarowanie powstających

odpadów. Wykonany prototyp poddano kompleksowym badaniom zgodnie z opracowaną metodyką weryfikacji, we współpracy z przedsiębiorcą zainteresowanym wdrożeniem rozwiązania.

**Słowa kluczowe:** automat sprzedażowy, jednorazowa odzież ochronna, niezawodność, sterowanie.

## 1. Introduction

There is a high turnover of patients, visitors, staff and customers in medical facilities, treatment rooms and beauty parlours. During periods of intensified transmission of pathogens, as in the case of SARS-CoV-2, there is a high risk of rapid and wide spread of diseases. However, medical facilities are never completely free from pathogens even when the risk of a pandemic is low, which means that all possible measures and safeguards against uncontrolled transmission of pathogens must be implemented (e.g. the obligation to wear shoe covers in hospitals). Recently, there has been a growing need for disposable isolation gowns to be worn in medical facilities, particularly by visitors. This, in turn, has called for the organisation of an effective disposable PPE supply and distribution system, and the use of vending machines, commonly used to dispense shoe covers, proved to be the best and, at the same time, the easiest solution. What is needed is just a standardised packaging in which PPE (e.g. isolation gowns) should be placed to be easily dispensed, and a good location, preferably at the entrance door, where persons entering the facility can in a matter of seconds buy the required item with cash or debit/credit card.

Vending machines [6, 12] are commonly used to dispense snacks, canned or bottled beverages [1, 7], small toys, souvenirs and other small objects. Disposable PPE is characterised by high volume at a relatively small weight, which requires developing a special solution for its distribution. Additionally, most vending machines dispense various products showcased to customers [3]. In the case of disposable PPE, only one product is sold, which means that the space typically used to showcase products can be used to stack more items, which, in turn, means less frequent refilling.

Researchers at the Łukasiewicz Research Network – Institute for Sustainable Technologies (Łukasiewicz-ITeE) conducted studies on controlled distribution, dispensing and transportation of products, bulk and semi-liquid materials, and gases. The research was commissioned by business entities and scientific centres and it led to the development of, among other things, a solution for controlled transportation, quality assurance and selection of goods in a machine industry [14, 13, 2]; an automated inspection line for glass products [4]; a paint robot and an in-salon hair dye dispenser [8, 11]; an erosion

testing device (abrasive dispenser) [10]; and a production line for cable insulators (superabsorbent dispenser) [9]. In each of the above-mentioned examples, problems of dispensing, transporting and positioning individual products for the purpose of optical quality control and maintenance, as well as precise metering or continuous dosing of semi-liquid substances and powders were solved.

The vending machine developed at Łukasiewicz-ITeE for Biovalley is designed for medical facilities and it enables safe, easy and effective dispensing of disposable isolation gowns right at the entrance. The researchers were asked to solve the problem of the vending machine volume-to-stacked product quantity ratio, which – in the case of the products for which the vending machine was intended – was not typical for vending machines on the market. A smaller vending machine dispensing one kind of a product lowers production costs and fees collected by the facility owner. Another problem that needed to be addressed was the power supply. A replaceable battery was used as a power source to avoid additional electricity costs. An adequate level of energy consumption (energy balance), guaranteeing that the timing of the battery replacement is consistent with the timing of vending machine restacking, was ensured. The vending machine was equipped with a system to collect used PPE and packaging. This is an important solution, not found in vending machines available on the market, which is in line with the principles of circular economy. The vending machine dispenses only one kind of a product, which limits transaction time and contact with the machine. Only contactless payments (credit/debit card or NFC mobile payments) are supported. This helps limit transmission of microbes and increase customer satisfaction (positive customer experience).

## 2. Concept of the vending machine

The designed standalone device had to comply with the following technical and performance requirements: capacity of the product rack – at least 250 products; card reader to allow debit/credit card payments; automatic dispensing of a product in no more than 2–3 seconds after purchase; and autonomic power supply enabling all products to be dispensed.

The concept of the disposable PPE vending machine is presented in Figure 1. Isolation gowns packed in cylindrical packaging tubes made of thin

plastic are stacked in the top part of the machine (product rack). At the bottom of the product rack, there is a rotating drum with sockets for individual packaging tubes with isolation gowns to which the product purchased is dropped. Then the drum rotates and dispenses the product to the pick-up tray. A contactless payment device (card reader) is installed in the front wall of the vending machine. The vending machine's control system and actuators are battery-powered. The use of an autonomic battery as a power source means that the machine can be placed in any

location, even in places where no electricity power supply is available. The designers of the prototype assumed that isolation gowns would be placed in two stacks (columns) to better use the product rack space and, at the same time, reduce the size (depth) of the machine, which is just slightly bigger than twice the length of the individual packaging. As a result, the machine can be put in a small room or hallway. Instead of a product showcase, descriptive information about the product was placed on the front wall of the cabinet.

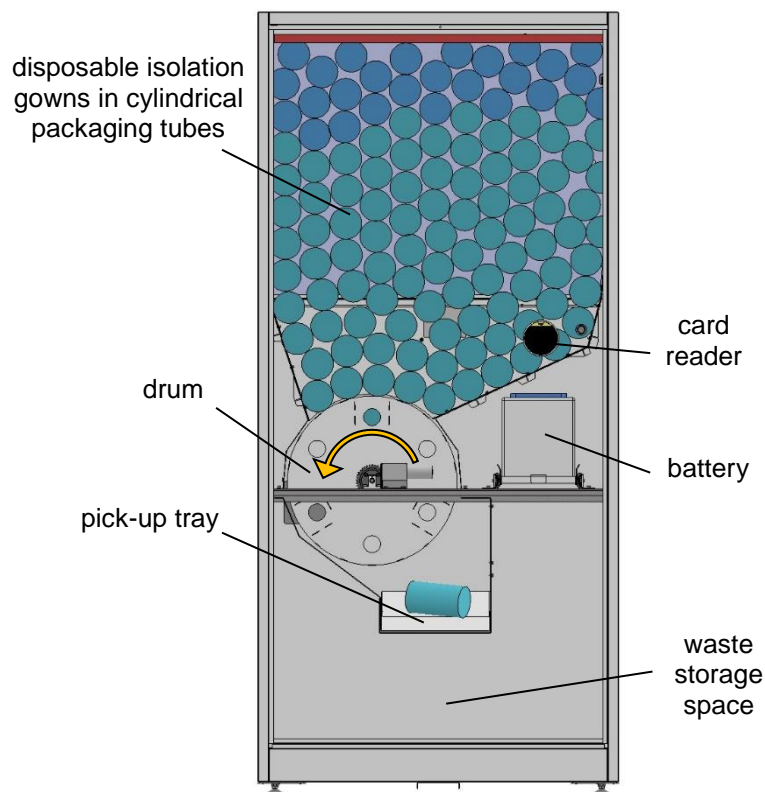


Fig. 1. Concept of the vending machine

The adopted concept assumes equipping the machine with integrated containers to store used gowns and packaging. The bottom part of the machine, which – for ergonomic reasons – would have been difficult to use otherwise, was designed for this purpose.

### 3. 3D model and documentation of the vending machine

The CAD 3D model was developed based on the adopted technical assumptions and concept of the vending machine. The model built in the CAD Autodesk Inventor system [5] allowed the spatial geometric and kinematic analysis of the adopted structural solutions. The model of a complete vending

machine with a visible internal structure is presented in Figure 2, and the elements enabling its automatic operation are presented in Figure 3.

The vending machine has a form of a rectangular cabinet in a metal casing (1), permanently closed on five sides; in the front wall there is a product inlet door (2), a card reader (3) and a service door. At the bottom of the front wall, in the centre, there is a pick-up tray (5) to which purchased gowns are dispensed. On each side of the pick-up tray there are slots for used gowns and packaging tubes (6). The pick-up tray and used gown and packaging tube slots are installed in a drawer, which plays the role of a waste bin (7). Disposable isolation gowns packed in cylindrical plastic packaging tubes (8) are placed on the product rack in two stacks separated by a moveable partition wall. At

the bottom of the rack (9) there are two slanted steel plates which enable the purchased product to easily slide to the middle and into a socket in the drum (10) closing the product rack from the bottom. The sockets are located in two rows – one closer the front wall of the cabinet under the front stack of plastic packaging tubes on the product rack, and the other closer to the back under the back stack. In each row there are six sockets in total (60° rotation). The drum rotates thanks to an electric motor with a shaft (11). Under the drum there is a dispensing chute (12), tilted towards the front wall of the cabinet, through which the purchased product is dispensed from the drum socket to the pick-up tray. The electric motor is powered by a battery (16) and controlled by an electronic controller (17). The product rack sensor detects a low level of product stacking, which indicates the need to refill the vending

machine. Drum position sensors (15) identify the indexed angular position of the drum. The drum rotates by 60°. The drum optical sensor checks whether a tube has been dropped into a correct drum socket. The product dispensing time  $t_p$ :

$$t_p = \frac{\alpha}{\omega} = \frac{\frac{\pi}{3}}{\frac{\pi n}{30} \frac{z_1}{z_2}}$$

where:

$\alpha$  – incremental rotation of the drum,  $= \frac{\pi}{3}$ ,

$\omega$  – angular velocity of the drum,  $\omega = \frac{\pi n}{30} \frac{z_1}{z_2}$ ,

$n$  – rotating speed of the gear motor, 12 r/min,

$\frac{z_1}{z_2}$  – transmission ratio,  $z_1 = 12$ ,  $z_2 = 36$ ,

is 2.5 s, in accordance with the adopted requirements.

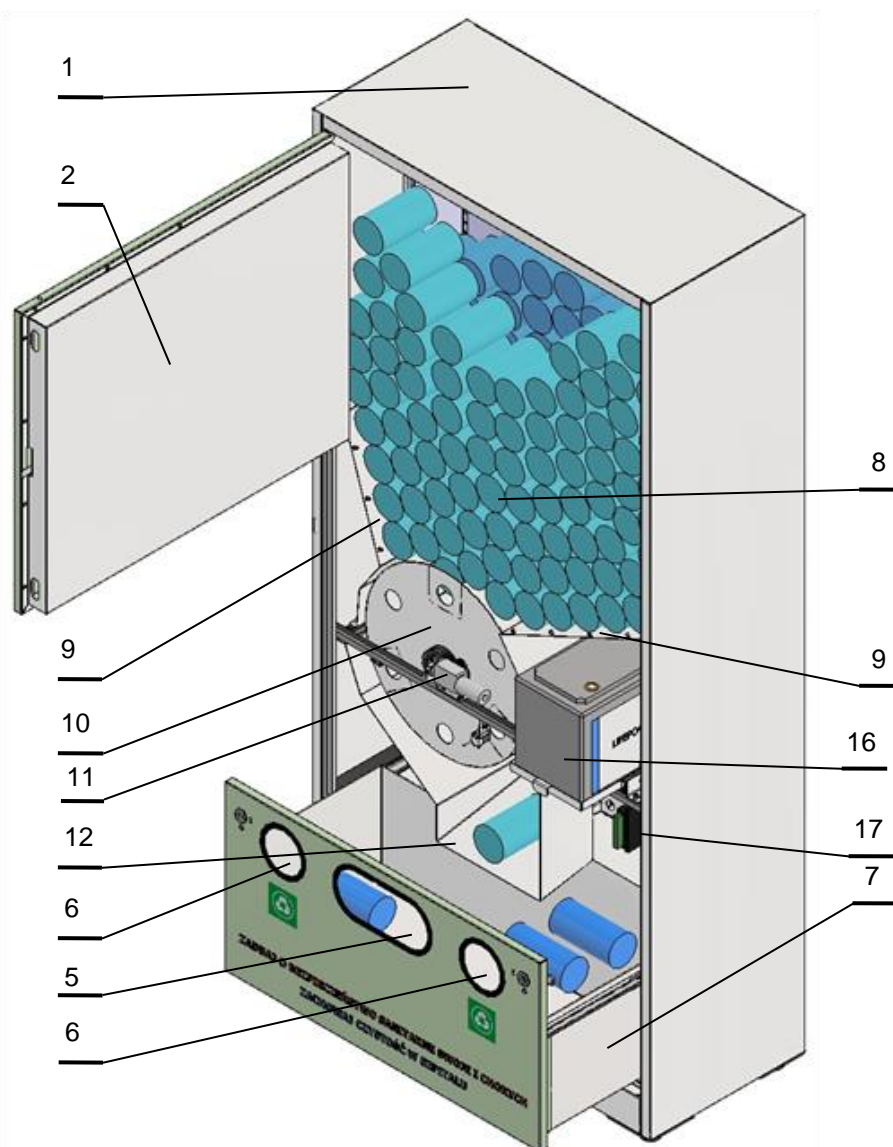


Fig. 2. CAD 3D model of the vending machine (general view): 1 – casing (cabinet); 2 – product inlet door; 5 – pick-up tray; 6 – slots; 7 – waste bin; 8 – products in cylindrical packaging tubes; 9 – bottom of the rack; 10 – drum; 11 – electric motor with a shaft; 12 – dispensing chute; 16 – battery; 17 – electronic controller

The vending machine can be filled with products after opening the product inlet door (Figure 5). First, products are stacked at the back and then at the front. Once the product inlet door is closed, the machine is ready to use. A customer activates the controller by pressing the button and making a contactless payment. This automatically activates the electric motor and rotates the drum. The drum makes so many 60 degree rotations as required for the sensor (14) to detect the presence of the product in the drum socket. When the machine works correctly, only one rotation is enough. After rotation, the product is dropped from the socket in the drum to the dispensing chute and to the pick-up

tray (5). After unpacking the gown, a customer can dispose of the packaging by placing it in the inlet hole (slot) at the bottom of the front wall. The other slot can be used to dispose of used gowns. The waste bin is attached to the sides of the cabinet with drawer slides, which means that all rubbish can be easily removed. Actuators and the card reader are powered by battery which stores enough electricity to keep the vending machine working for 18 days and dispense all products loaded (250 pieces). When the battery is flat (which is signalled automatically), it can be replaced with a charged one after opening the service door.

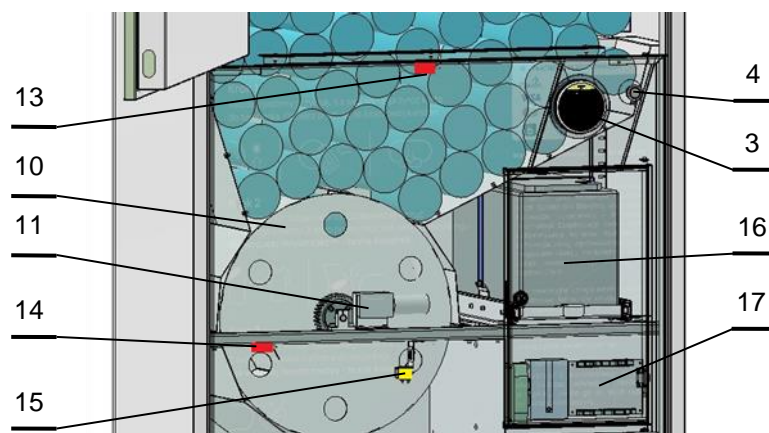


Fig. 3. CAD 3D model of the vending machine (automation elements): 3 – card reader; 4 – activating button; 10 – drum; 11 – electric motor with a shaft; 13 – product rack sensor; 14 – drum sensor; 15 – drum position sensor; 16 – battery; 17 – electronic controller

#### 4. Control system

The operation of the device is controlled by an electronic sensor, the block diagram of which is presented in Figure 4. The controller:

- controls the rotation of the drum based on the signals from sensors 14 and 15 and from a card reader (3) to properly dispense gowns;
- controls the inventory level using signals from sensor 13; and
- warns of a low product stacking and battery levels by sending an SMS.

The controller also controls the proper operation of the machine and manages battery electricity consumption; blocks the possibility of dispensing products that have not been paid for; and minimises the risk of accepting payment without dispensing a purchased product (this risk cannot be completely eliminated because it is impossible to exclude the potential failure of the machine after payment approval).

The control software verifies the proper sequence of sensor signals. This helps detect any inaccuracies and potential failures, e.g. absence of sensor signals,

damaged DC motor, drum block, product getting stuck in the dispenser. If such problems occur, an SMS notification is sent to maintenance workers. Such notifications are also sent when inventory levels are low. In such a case, once the signal from a relevant sensor has been confirmed five times in consecutive product dispensing cycles (to avoid any false alerts), maintenance workers will receive a notification reading: *ALERT: restack products*. The SMS notification module used was selected because it is reliable and characterised by low electricity consumption (approximately 0.005 A). For reasons of energy efficiency, the module was also used to measure and analyse battery charge level. In a standby mode, the main controller may use less electricity. Notification reading: *ALERT: replace batter* is sent when battery voltage drops to approximately 12.7 V and stays at this low level for at least 15 seconds. This value was selected to allow the battery to work for about three more days before the built-in battery management system (BMS) completely cuts off power supply. Theoretically, the use of a 100 Ah battery allows the machine to work for the maximum of 18 days (approximately), at the average electricity consumption of 0.23 A in a standby mode.

However, in practice, this period is a bit shorter (16–17 days), because, realistically, the available battery capacity will be lower than 100 Ah, and electricity consumption may also vary over time and

depending on the place of installation. This can be connected, among others, with higher electricity consumption when payment is made, notification sent, and product dispensed.

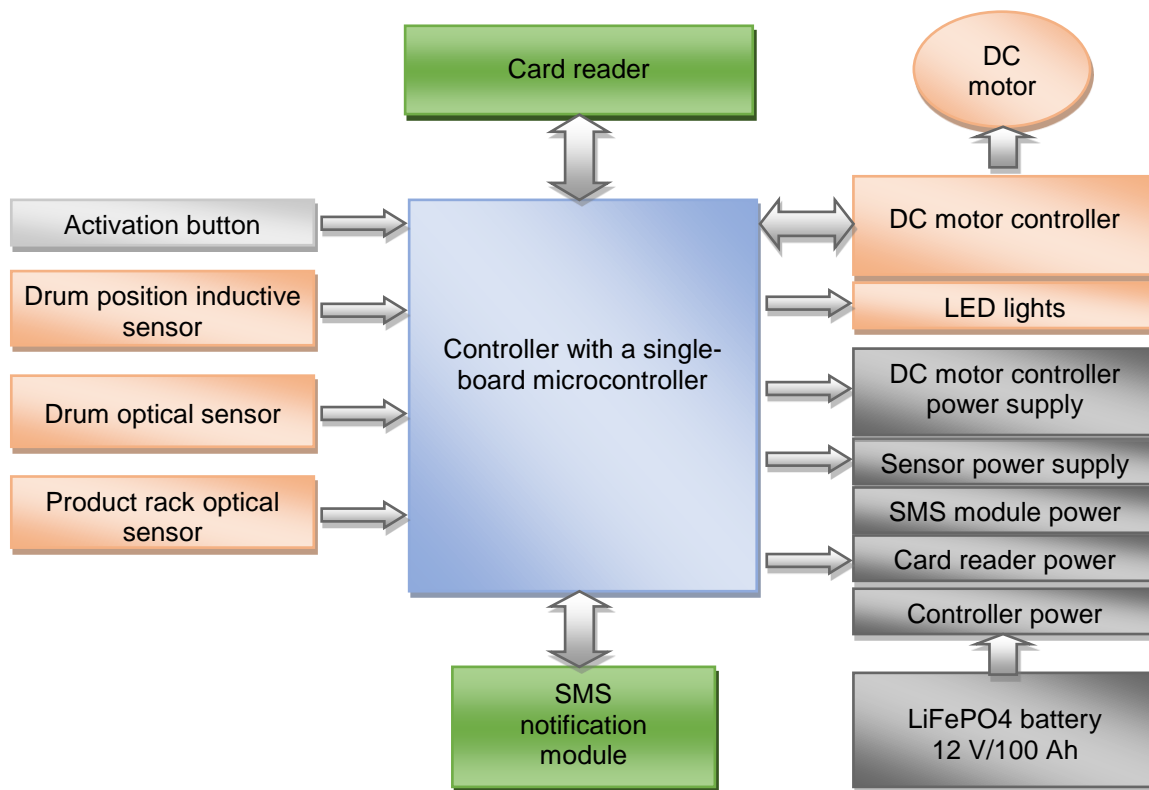


Fig. 4. Block diagram of the control and power supply systems

As shown in Figure 4, the controller manages battery electricity consumption. Electricity consumption is not monitored only in the case of the SMS notification module. All other components of the control system are enabled and activated only when the payment is made and product dispensed. This means that the optical sensors and the inductive sensor consume approximately 0.05 A each (0.15 A together). With the use of an additional activation button the machine wakes up from the standby mode. This button also unblocks the card reader, provided that a product is already in the drum socket. The LED illumination of this button also informs the customer whether or not the vending machine is fully operational – a continuous light indicates operability, while pulsing light means that the machine is faulty or empty.

When activated, the card reader consumes 0.35 A of electricity on average. Leaving it active would shorten the battery life. Therefore, after one minute, the card reader is blocked by the controller and goes into standby mode. Unfortunately, even in standby, the card reader consumes a lot of electricity (0.20 A) and

further electricity use reductions are impossible. In practice, completely cutting off the card reader power supply when the machine is not in use is not possible. This is because it takes 1.5 minute to activate it after a long period of idleness. Therefore, the card reader is the main component that determines the maximum operating time of a battery-powered vending machine.

## 5. Prototype verification

The prototype was built based on the adopted assumptions, developed model and technical documentation (Fig. 5). The prototype was equipped with a complete set of control instrumentation and software to verify the correct operation of the individual units and software controlling the automatic implementation of functional procedures.

The verification and functionality tests were carried out under real operating conditions [15]. Particular attention was paid to reliability of product dispensing (from a product rack to the drum and from the drum to the pick-up tray). The geometry of the bottom of the product rack and the size of the drum sockets were modified. The changes eliminated the

problem of occasional blocking of the collecting mechanism, improved the reliability of product collection from the product rack, and helped to dispense all products stacked. The dispensing chute was reshaped to ensure ergonomic positioning of the product in the pick-up tray. The bottom drawer (waste bin) was equipped with full-extension slides to enable easier collection of used gowns and plastic packaging tubes. Weights were mounted in the lower part of the machine – they lower the position of the centre of

gravity of the machine and position it better. The maximum operating time of the 12 V/100 Ah battery was tested. Dispensing all products used 2 Ah, which meant that the vending machine could remain on standby for about two weeks. Emergency control procedures were designed and introduced for uneven stacking of products on a product rack, dispensing errors, sensor failures or operation when a nearly flat battery is left to stand. Tests allowed the determination of flat battery notification thresholds.



Fig. 5. Prototype of a vending machine: a) at the time of stacking, b) after mounting at a medical facility

A verified prototype was placed in a medical facility (Figure 5b). The results of verification and field tests show that the developed device complies with the main requirements adopted at the concept stage.

The original structural solution of the vending machine developed at Łukasiewicz–ITeE and the entire concept of the device are the subject of a patent application and they are protected by intellectual property rights [16].

## 6. Summary

A prototype of a disposable personal protective equipment vending machine for facilities where procedures to prevent the spread of pathogens are in place and in use was designed and developed at Łukasiewicz–ITeE. The concept and the modus operandi of the machine were developed and formulated in cooperation with and as commissioned by a manufacturer and supplier of disposable personal protective equipment. The vending machine can dispense one product

type only, which, despite the limited size of the device, allows many products to be stacked. In the developed solution, an autonomic battery power supply and a card reader for contactless payments are used. The functional tests of the prototype confirmed that the functional parameters assumed at the concept stage were achieved and they revealed the potential for further improvement, particularly as regards the adaptation of selected structural solution to potential mass production. The developed and verified prototype, with a strong scientific foundation, may be an important step in the development of special purpose vending machines and a starting point for building similar scalable and customisable devices. Test results show that the stiffness and repeatability of the packaging (dents) have a major impact on the automatic dispensing process, which means that maintenance staff need to be very careful when stacking products as instructed. The original structural solutions developed at the Łukasiewicz–ITeE are the subject of a patent application.

## References

1. Buffington A. M. 2017. Are Vending Machine Selections Healthier? Trends in Dietary Quality of Vending Machine Food and Beverage Selections among NHANES Participants Age 6-19 Years between 2003-2012. University of Nevada, Las Vegas.
2. Czajka P., Samborski T., Garbacz P., Mężyk J. 2017. Automatisation of Multi-Parametric Quality Inspection of Rotary Symmetrical Metal Elements. *Journal of Machine Construction and Maintenance*, (2): 35-43.
3. Fukuda K., Iwako T., Nakajima N. 2015. Product Dispensing Mechanism for Vending Machines for Global Market. *Fuji Electric Review* Vol. 61-No.3: 187-190.
4. Garbacz P., Czajka P., Mizak W. 2016. Automation of Residual Stress Measurement in Tableware Glass Production. *Problemy Eksploatacji – Maintenance Problems*, (1): 29–40.
5. Jaskulski A. 2020. Autodesk Inventor Professional. Helion.
6. Kajimura T., Kametani N., Miyagishi T. 2003. Present Status and Future Prospects of Vending Machines. *Fuji Electric Review* Vol.49-No.1: 2-6.
7. Kobayashi T., Nishi M., Tamura T. 2003. Multi-purpose Food Vending Machines. *Fuji Electric Review* Vol.49-No.1: 11-15.
8. Kozioł S., Samborski T., Zbrowski A., Lipiński J. 2018. Modułowa struktura robota malarskiego do malowania obrazów. *Technologia i automatyzacja montażu*, (4): 21-27.
9. Kozioł S., Zbrowski A., Wiejak J. 2010. Modernisation of the technological line for the production of moisture resistant cable laminatem. *Problemy Eksploatacji* (4): 115-125.
10. Mizak W., Mazurkiewicz A., Smolik J., Zbrowski A. 2014. Problems with abrasive dosing in erosive wear process modelling. *Eksploatacja i Niezawodność – Maintenance and Reliability* (4): 559-564.
11. Samborski T., Zbrowski A., Mrozek M., Kozioł S. 2023. Automatic semifluid mass dispenser. *Technologia i automatyzacja montażu*, (1): 37-43.
12. Segrave K. 2015. *Vending Machines: An American Social History*. McFarland.
13. Zacharski S., Samborski T. 2015. Robotised and reconfigurable system to support the production process in the machining industry. *Problemy Eksploatacji – Maintenance Problems*, (1): 111-120.
14. Zbrowski A., Giesko T. 2008. Automatyzacja kontroli jakości wyrobów w linii technologicznej wytwarzania wałeczków łożysk tocznych. *Technologia i Automatyzacja Montażu*, (2): 36–40.
15. Zbrowski A. 2016. *Metodyka badań prototypów i jednostkowych urządzeń technicznych*. Radom: Wydawnictwo Naukowe ITeE – PIB.
16. Zgłoszenie patentowe P.443101. 2022. Urządzenie do samoobsługowej sprzedaży zwłaszcza jednorazowej odzieży ochronnej oraz sposób samoobsługowej sprzedaży zwłaszcza jednorazowej odzieży ochronnej.

## SIMULATION OF DISPLACEMENT OF CUTTING TOOL HOLDERS USED FOR TURNING

## SYMULACJA ODKSZTAŁCENIA I ODCHYLEŃ UCHWYTÓW NA NARZĘDZIA SKRAWAJĄCE STOSOWANYCH DO TOCZENIA

Viktor MAUTNER<sup>1</sup>, Katarina HORVAT<sup>2</sup> , Marija STOIC<sup>3</sup> , Antun STOIC<sup>4\*</sup> 

<sup>1</sup> ĐĐ TEP d.o.o, Ul. 108 brigade ZNG 1, 35000 Slavonski Brod, Croatia, e-mail: mautnerviktor@gmail.com

<sup>2</sup> Strojarstva tehnička škola Frana Bošnjakovića, Konavoska ul. 2, 10000, Zagreb, Croatia, e-mail: katarina.stoic666@gmail.com

<sup>3</sup> University of Slavonski Brod, Trg Ivane Brlić Mažuranić 2, 35000 Slavonski Brod, Croatia, e-mail: mstoic@unisb.hr

<sup>4</sup> University of Slavonski Brod, Trg Ivane Brlić Mažuranić 2, 35000 Slavonski Brod, Croatia, e-mail: astoic@unisb.hr

\* Corresponding author: astoic@unisb.hr

### Abstract

This paper gives a comparison of the deformation and deflection of two types of tool holders used in turning processes. Comparison of the deflection and stresses has been performed on the location where the highest value of deflection can be measured i.e. on the tip of the cutting insert. Selected tool holder types (TH1 and TH2) have rectangular and polygonal shank. Tool holders were 3D modelled in SolidWorks and Autodesk Inventor software packages and exposed to the loading with ANSYS structural analysis FEM software. In FEM analysis, two elements size of the network are selected (mesh size 5 and 1 mm). The simulation was carried out for five different loading values acting on the tool holder model. Obtained results confirm lower deflections on CAPTO tool holders.

**Keywords:** FEM, cutting tool holder, deflection, turning.

### Streszczenie

W artykule porównano odkształcenie i ugięcie dwóch typów opravek narzędziowych stosowanych w procesach toczenia. Porównanie ugięcia i naprężeń wykonano w miejscu, w którym można zmierzyć największą wartość ugięcia, czyli na czubku płytki skrawającej. Wybrane typy opravek narzędziowych (TH1 i TH2) mają chwyt prostokątny i wielokątny. Uchwyty narzędziowe zostały wymodelowane w 3D w pakietach oprogramowania SolidWorks i Autodesk Inventor i poddane obciążeniu za pomocą oprogramowania do analizy strukturalnej FEM ANSYS. W analizie MES wybierane są dwa rozmiary elementów sieci (rozmiar oczek 5 i 1 mm). Symulację przeprowadzono dla pięciu różnych wartości obciążeń działających na model oprawki. Uzyskane wyniki potwierdzają mniejsze naprężenia i ugięcia opravek narzędziowych CAPTO.

**Słowa kluczowe:** MES, oprawka narzędzia skrawającego, ugięcie, toczenie.

## 1. Introduction

During machining process with clamped tool shank, the most of mechanical energy that is required to remove the chips from the workpiece has been spreaded over the contact surfaces. Cutting edge has been exposed to the workpiece resistant forces

that are transmitted on tool holder and as a result appears tool deformation and deflection. Because of force action, extensive contact stresses are present and combined elastic and plastic deformations may appear.



Both of processes (deformation and deflection) achieves maximum values on cutting contact surfaces between cutting tool and finish product. Many researchers explore deflection either tool (tool holder) either workpiece. In inner surface turning process and sculptured surface milling process, more interested is tool deflection. In contrast, deflection of participant with bad ratio of length and cross dimension which appears in thin wall and small diameter workpieces is also interesting.

Furthermore, over the tool holder clamping contact surfaces displacements and deformations has been transferred on the third participant of the machining process, machine tool individually. Deformations and deflections also occur on each certain sequentially connected parts of the machine tool, making tool and workpiece clamped together. Therefore, determining the effect of total deformation and deflection during machining on machining accuracy is very complex.

The cutting force generated with regime of turning process in regards with slenderness causes certain values of deflection. Consequently deflections, the true depth of cut differs from the planned value, manifesting as surface or dimensional errors on the workpiece or increased tool wear.

Deflections can influence many other unfavorable effects like loss of tolerances on workpiece, change of shearing angle and difficulties in chip formation, friction and tool wear condition.

As a mainly adverse effect of deflection, dimensional errors in turning, chatter appearance etc. have been recently analyzed by many researcher [1],[2],[3]. Duan et al. [1] estimates tool deflection variation as a result of inclination of tool edge and workpiece. Their tool deflection model gives more precise results when higher deflections appear if comparing model results with real experiment measurement. Gasagara et al. [2] determine that dynamic behavior of tool deflections induces chatter vibrations. Furthermore, conclusion was that deflections varies throughout the tool. It has maximum at tool tip and minimum at the position of clamping. In his work Kalasua et al. [3] determine the cutting tool deflection as a result of acting cutting forces which were influenced by cutting regime and tool geometry. Kops et al. [4], [5] perform deflection analysis by using an analytical formulation and obtaining an interrelationship between the workpiece deflection and depth of cut. Yang et al. [6] perform FEM analysis on model developing a real-time workpiece deflection error compensation system facing also with different deflection values along the

workpiece. In both work, only the radial component of the cutting force is considered.

Some other researcher expand the analysis on multi-diameter workpiece bars [7] and tapered workpieces [8] including all cutting force components and FEM.

Too much deflection can lead to catastrophic failure on the tool if chatter appears and lead to workpiece surface roughness increase [9]. Kiyak et al. [9] explore in their work the influence of functional tool length (tool overhang) on tool deflection, surface roughness and flank tool wear. Cross section of tool holder was 25x25 mm and functional tool length varies from 50 to 90 mm. With increasing of the tool length, deflection and roughness increases also, but flank wear decreases.

Analysis performed in this paper is oriented towards deformations and deflections that appear on the cutting tool holder. Selection of tool holder is very important role in planning of cutting process. Tests were made on selected tool holders with rectangle and polygonal clamping surfaces commonly used in turning process. Analysis has been performed assuming that all parts of the machine tool and contact surfaces during the loading condition affected by cutting process are considered rigid.

Depending on value of the force and its orientation during cutting process, as well as orientation and size of clamping shank surface, various deflection on the edge tip can appear. Shank surfaces in rectangular holder are parallel (angle between contact surfaces are 0°) and in CAPTO polygonal clamping system contact surfaces are under the angle 2,88°. The higher the angle of contact surfaces the higher deflection can be expected. Main difference between CAPTO and rectangular shank is that CAPTO allows additional flange contact (see Fig. 1). To be comparable, selected tools has different functional length of cutting edge on holder 1 (TH1) and holder 2 (TH2) with values 70 and 50 mm respectively (see Fig. 1).

Cross-section area of rectangular tool holder shank was 32x25 mm and fixation length was 100 mm, while polygonal shank holder was C4 (ISO 26623-2:2014 specifies dimensions for polygonal taper interfaces with flange contact surface). Some dimensions and data of CAPTO holders are given in Table 1. Cross section dimension of tool holder influence deflection values with power of 4 and functional length with power of 3.

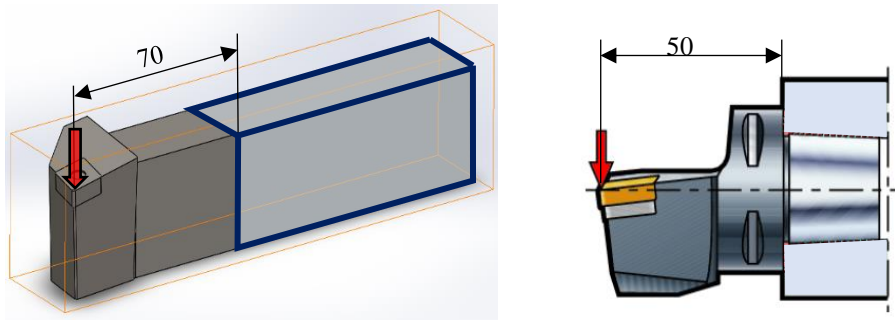


Fig. 1. Functional length of tool holders

Table 1. Some data of CAPTO holders

Holder type	Functional length, mm	Flange diameter, mm	Clamping force, kN
C3	40	32	13
C4	50	40	22
C5	60	50	30,5
C6	65	63	39
C8	80	80	48

Deflections can be given in absolute values (values in mm) or relatively (values in mm/m – Figs. 2 and 3) values. Relative values of deflection shown in Figs. 2 and 3 are approximative values used just to select comparable size of holder for this experiment (in our tests similar approximative deflections have C4 and PCLN3225 holders). For selected tool holders (marked with red color in Figs. 2 and 3), we expect similar and comparable deflection values of tool tip. This relative deflection parameter is obtained by dividing absolute deflection value with functional length of cutting tool. Results should enable better tool holder selection in planning process.

The high compressive and frictional contact stresses on the tool/workpiece interface can be simplified and replaced with a total cutting force  $F$  as shown in Fig. 4. Dependence of forces and its influence on deflection has been analyzed by Kowalik et al. [10]. The cutting force vector is defined in terms of orthogonal cutting with force components  $F_c$ ,  $F_f$ ,  $F_p$ . These components are most often shown in the literature, and their vectors are oriented in the direction of cutting speed, feed and cutting depth ( $v_c$ ,  $f$ ,  $a_p$ ) Fig. 4.

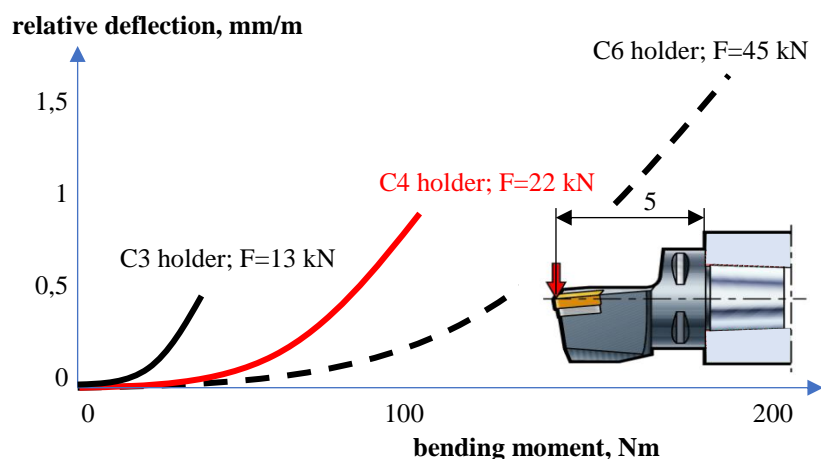


Fig. 2. Influence of selected polygonal shank tool holder on relative deflection of tool tip

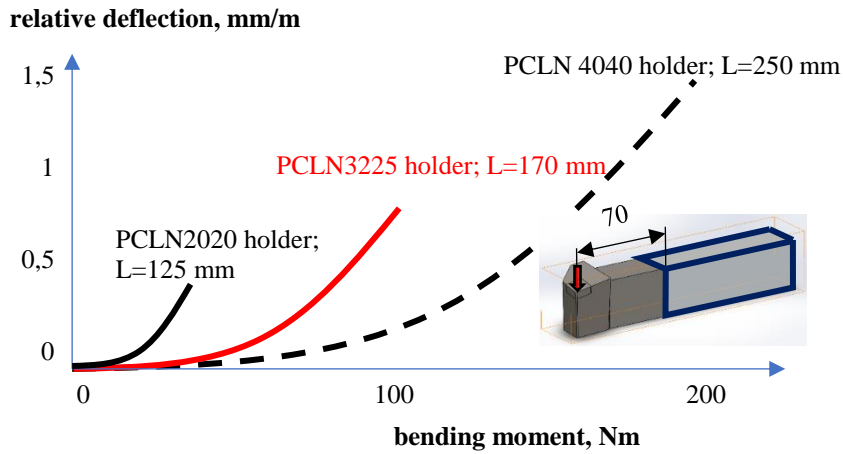


Fig. 3. Influence of selected rectangular shank tool holder on relative deflection of tool tip

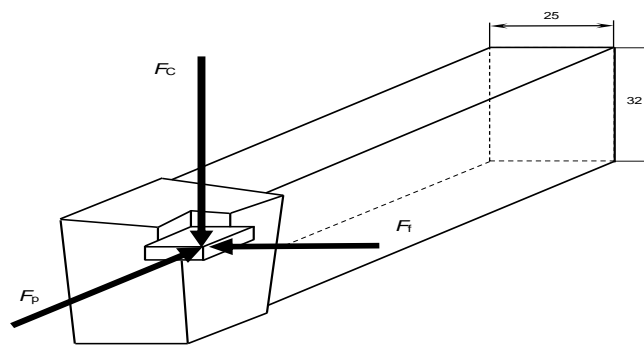


Fig. 4. Force components acting on rectangular shank turning tool

## 2. Tool holders modeling

The 3D models of two holders consists of several merged bodies: an external turning tool holder and a cutting insert with fixation devices for its fixation on the holder. The dimensions of the model are defined by the dimensions declared by producer of real holder and the insert.

For rectangular (TH1) shank model, it was used the Corloy CNMG 120408HA (NC 3220) insert. The dimensions of the insert are:  $l = 12.0$  mm,  $t = 4.76$  mm,  $r = 0.80$  mm,  $d = 12.70$  mm,  $d1 = 5.16$  mm. The insert was inserted and fixed into the PCLNL 3225M12 tool holder. The holder and the insert are molded in the package SolidWorks (Fig. 5). For polygonal (TH2) shank holder, it was used Sandvik Coromant model C4DCKNR-27050-12 (Fig. 6).

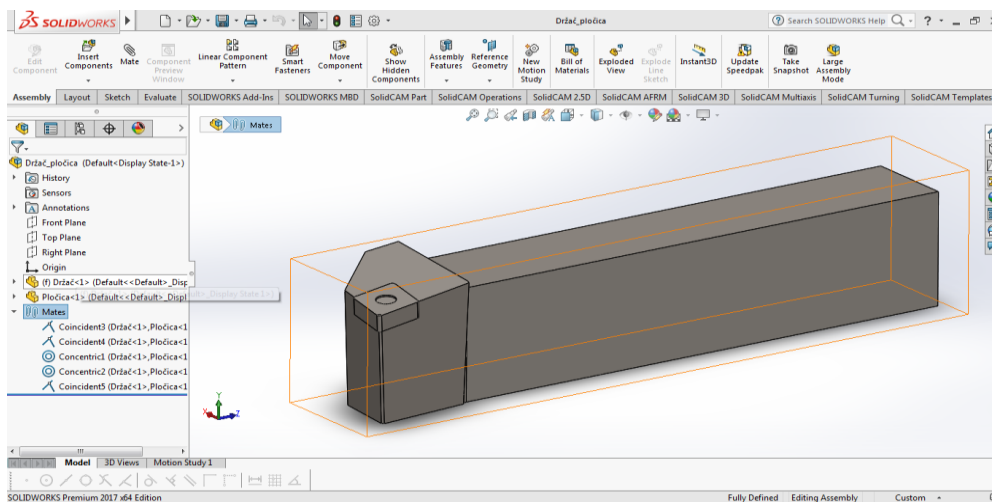


Fig. 5. Model of cutting tool holder with insert

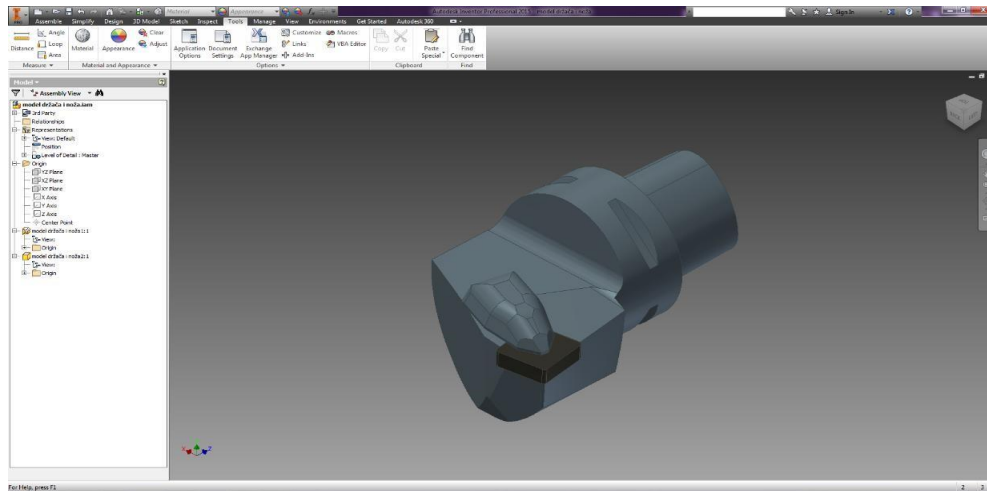


Fig. 6. 3D model of CAPTO tool holder prepared in Autodesk Inventor

The contact surfaces between the model parts (tool holder and insert) have been merged and thus the model position within the space has been defined. To obtain accuracy of modelled stresses and deformation during simulation, it is necessary to merge all the contact surfaces to each other because the forces in reality are transmitted over all of these surfaces.

### 3. Mesh size selection

The developed finite element models of considered tool holders were analyzed using static structural approach within the ANSYS software. Using of this software needs short time training and is not complicated in use [11].

Results obtained by this software can be used for better tool holder selection. The software enables

simulation of problems in multiple scenarios and with different parameters. This is the reason why this software can be used in almost all industries and enables product optimization and cost savings comparing with physical tests. [12]

Two network mesh of finite elements is defined for selected tool holders. By choosing a smaller size of elements, a model with a flawed grid is obtained, i.e. the model has multiple elements. Also, by choosing smaller mesh elements the results obtained by simulation are more accurate but FEM calculation process last longer. For comparison purposes, two dimensions of the elements were selected for this work. One net is less common (popular) with the size of the 5 mm elements, the Fig. 7 - left and the other the mesh is louder with the size of the 1 mm elements, Fig. 7 - right.

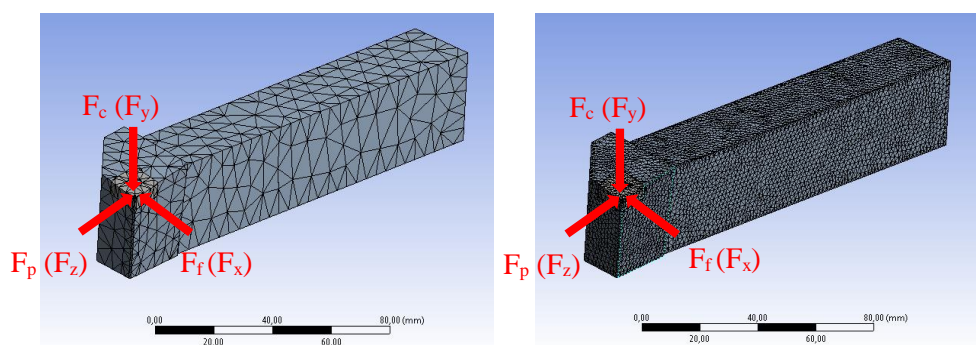


Fig. 7. Spreading of FEM mesh over the rectangular cutting tool (5mm-left, 1mm-right)

The force action location is nested on one single point on edge tip. This location represents the contact surface between the insert and workpiece during turning process. The force components ( $F_x$ ,  $F_y$ ,  $F_z$ ) are set in the direction of all three axes substituting appropriate ( $F_c$ ,  $F_f$ ,  $F_p$ ) components.

Before the simulation starts, it is necessary to select the desired mesh size elements. Of course, as

many elements are selected, longer simulations will last because of the greater number of equations that needs to be solved. For this analysis two parameters have been observed. These are data on overall (total) deformation and stress.

For simplification of force components value selection, the equal values of the cutting force components in the direction of the x and z axis were

selected (in reality, the passive and shear components of the cutting force). The highest value of the force is in the direction of the axis y, which is also in real load conditions.

#### 4. Results

The simulation was carried out for five different values of force acting on the model. Each of these 5 force values were used through simulation of the above-mentioned two variants of the finite element mesh node numbers.

The cutting deflection ( $\delta$ ) of the cutting edge is particularly important as the size of the deformation affects the machining accuracy, as well as on other geometrical size tribology processes on the cutting tools contact surfaces. For this reason, only the size of

the deformation will be presented in simulation results. Deformation values  $\delta_5$  and  $\delta_1$  are obtained for different FEM mesh size 5 and 1 millimeters respectively.

Table 2 shows the results for five different load combinations (five values of loading) and for different FEM mesh size (two mesh size). Displacement values given in table 2 are total values of displacements.

The picture of deformations shown in table 3 shows that the greatest deformations (deflections) appear at the very top of the inserts, exactly on location where the force acts. In the area of cutting tool support, they do not even appear because they are assumed as a rigidly fixed contact. Highest value of deformations (deflections) and the largest stress concentration is created also at the location of force action.

Table 2. Results of displacements

Meas. nr	Tool holder type	Total force F, N	F <sub>c</sub> , N (F <sub>y</sub> )	F <sub>p</sub> , N (F <sub>z</sub> )	F <sub>r</sub> , N (F <sub>x</sub> )	FEM - mesh size 5 mm	FEM - mesh size 1 mm	$\Delta$ ( $\delta_5$ , $\delta_1$ ), %
						Deform. $\delta_5$ , $\mu\text{m}$	Deform. $\delta_1$ , $\mu\text{m}$	
1	Rectangular shank, TH1	966,6	900	250	250	29,264	30,605	4,38
2		1510	1400	400	400	45,232	47,321	4,41
3		2053	1900	550	550	61,202	64,039	4,43
4		2596,2	2400	700	700	77,172	80,758	4,44
5		3139,3	2900	850	850	93,142	97,477	4,45
1	Polygonal shank, TH2	1023,9	950	270	270	17,627	18,572	5,09
2		1603,1	1500	400	400	27,902	29,392	5,07
3		2053,0	1900	550	550	35,228	37,119	5,09
4		3019,9	2800	800	800	51,943	54,729	5,09
5		3724,3	3500	900	900	65,193	68,667	5,06
6		4242,6	4000	1000	1000	74,583	78,55	5,05

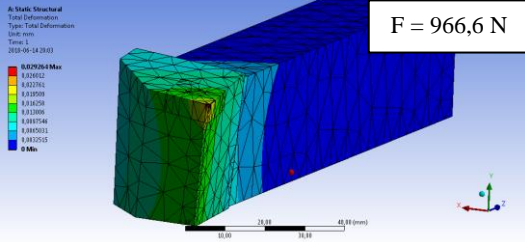
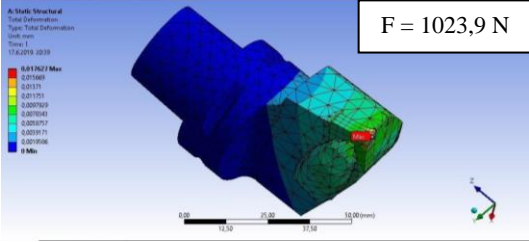
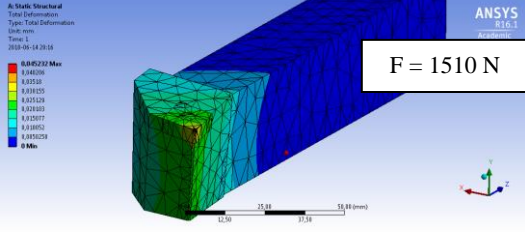
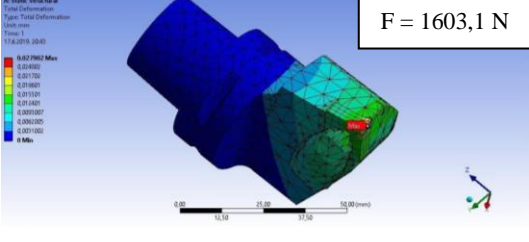
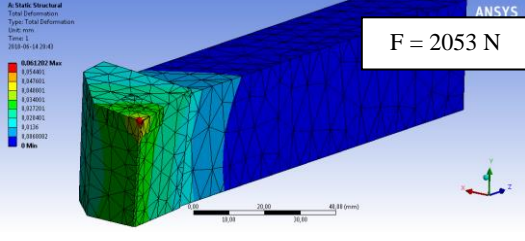
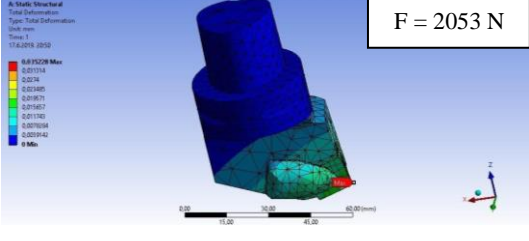
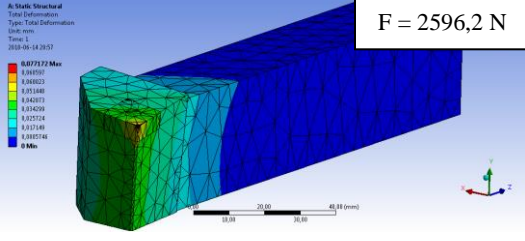
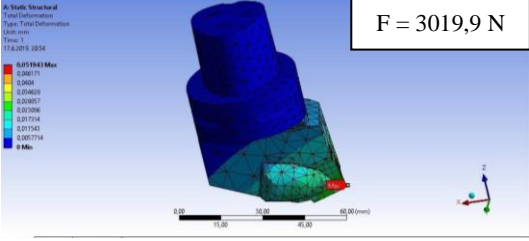
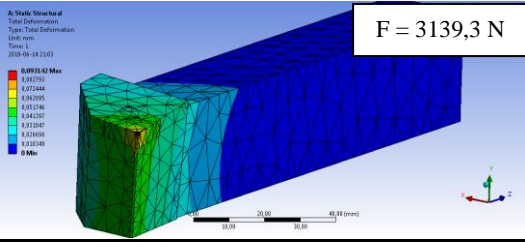
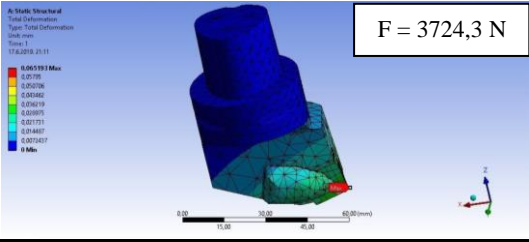
Table 2 shows that the results with the smaller mesh size are slightly different, or higher than those of the previous ones. The reason for this is just the number of elements that are smaller on the model and the results are more precise.

But, it is also apparent that the differences in the model obtained deformations are less than 5% (Table 2) which can be considered as sufficiently accurate if a mesh with larger elements is applied.

Comparison of deflection results obtained for two holder are given in absolute values (Fig.8). Better deflection results have been obtained for polygonal shank holder (TH2). Reason for such results some can explain with better slenderness of this holder. There is

also visible slightly higher distancing of lines for higher loading. The reason for this fact lies in different cross section dimension and functional length of tool holders (deflection increase with these parameters with power of 4 and power of 3 respectively). If deflection results are compared in relative values, difference between these two holder becomes lower (Fig. 9). Deflection data are given for the model with mesh size 5 mm. Some author show the deflection results as a function of bending moment. If the comparison of deflection has been made in this frame, better results are obtained for rectangular tool holder TH1 (Fig. 10).

Table 3. Deformation ( $\delta_5$ ) distribution over the cutting tool holder model

nr	Rectangular tool holder deflection values $\delta_5$ , mm	Polygonal tool holder deflection values $\delta_5$ , mm
1	 <p><b>F = 966,6 N</b></p>	 <p><b>F = 1023,9 N</b></p>
2	 <p><b>F = 1510 N</b></p>	 <p><b>F = 1603,1 N</b></p>
3	 <p><b>F = 2053 N</b></p>	 <p><b>F = 2053 N</b></p>
4	 <p><b>F = 2596,2 N</b></p>	 <p><b>F = 3019,9 N</b></p>
5	 <p><b>F = 3139,3 N</b></p>	 <p><b>F = 3724,3 N</b></p>

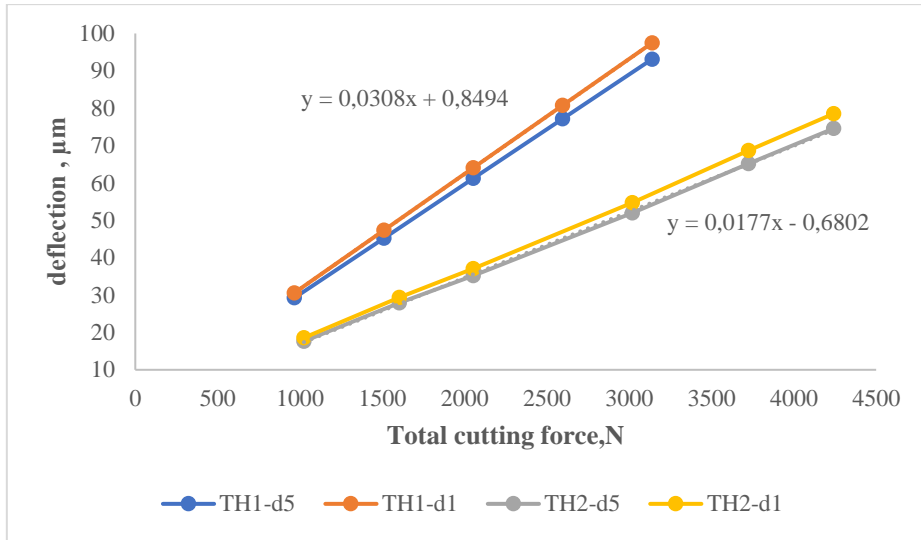


Fig. 8. FEM results of absolute deflection data

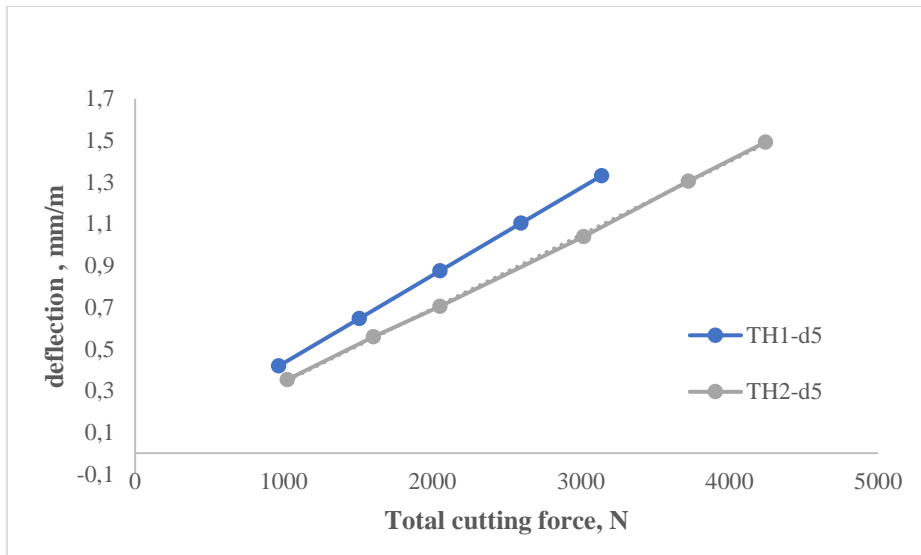


Fig. 9. FEM results of relative deflection data

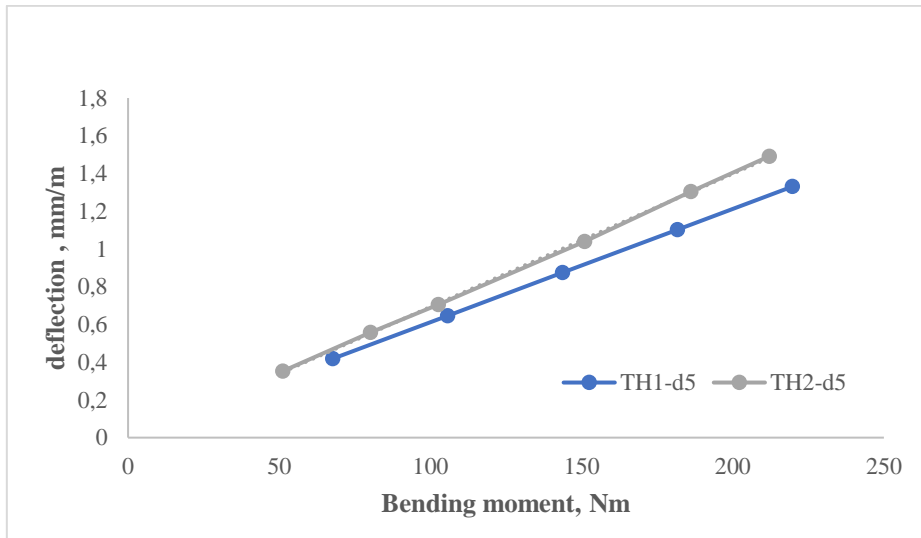


Fig. 10. FEM results of relative deflection data vs bending moment

## 5. Analysis of results and conclusions

The results of tool holder deflection shown in this paper, and obtained by FEM simulation of loading of two types of cutting tool holders, can be expected during real turning process. The results obtained by the simulation even without the use of the machine tool offers useful information for process optimization. Comparison of calculated tool deflection values for selected tool holders offers the answer which tool holder has bigger impact on dimensional accuracy of workpiece resulting from tool holder deflection. Tool deflection values for both tool holders are relatively small and for OD turning process these deflections have no the most significant influence on dimensional accuracy. More important influence on machining accuracy could have deflection of workpiece.

The differences in the model obtained deflections for different FEM mesh element size are less than 5% and mesh element size of 5mm is capable to offer acceptable results. FEM calculation with larger mesh size allows also very fast obtaining of results.

The increase of the force acting on the model increase deformations and stresses of tool holder.

Beneficiary, FEM deflection analysis offers possibility of exposing the tool holder model to various forces and processing modes without the risk of damage and material destroying. By optimizing the turning process parameters experimentally instead of on a computer, some will spend a lot of time, generate greater material consumption and, most importantly, there is a risk of fractures and failures due to wrongly selected regime parameters.

## References

1. Duan Xianyin, Peng Fangyu, Yan Rong, Zhu Zerum, Huang Kai, Li Bin. 2016. "Estimation of Cutter Deflection Based on Study of Cutting Force and Static Flexibility". *Journal of Manufacturing Science and Engineering*, 138 (041001): 1-15.
2. Gasagara Amon, Jin Wujiyin, Uwimbabazi Angelique. 2019. "Stability analysis for a single-point cutting tool deflection in turning operation". *Advances in Mechanical Engineering* 11(6): 1-14.
3. Kalasua Vishrant, Tiwari Gaurav, Thakur Ankit. 2015. "Modelling of Single Point Cutting Tool Deflection due to Cutting Forces under Variable Side Rake Angle". *International Journal for Research in Applied Science & Engineering Technology*, 3 (1): 2321-9653.
4. Kops Lukas, Gould Madelyn, Mizrach Michael. 1993. "Improved analysis of the workpiece accuracy in turning, based on the emerging diameter". *ASME Journal of Engineering for Industry*, 115: 253-257.
5. Kops L., Gould M., Mizrach A. 1994. "A search for equilibrium between workpiece deflection and depth of cut: key to predict compensation for deflection in turning" *Manufacturing Science and Engineering ASME*, 68(2):819-825.
6. Yang S., Yuan J., NiJ. 1997. "Real-time cutting force induced error compensation on a turning center" *International Journal of Machine Tools and Manufacture*. 37: 1597-1610.
7. Cloutier G., Mayer J.R., Phan A-V. 1999. "Singular function representation in obtaining closed-form solutions to workpiece deflections in turning multi-diameter bars". *Computer Modeling and Simulation in Engineering*, 4: 133-137.
8. Phan AV., Cloutier G., Mayer J.R.R. 1999. "A finite element model for predicting tapered workpiece deflections in turning" *Computer Modeling and Simulation in Engineering*, 4: 138-142.
9. Kiyak M., Kaner B., Sahin I., Aldemir J., Cakir O. 2010. "The dependence of tool overhang on surface quality and tool wear in the turning process" *International Journal Advanced Manufacturing Technology* 51 : 431-438.
10. Kowalik M., Rucki M., Paszta P., Gołębski R. 2016. "Plastic Deformations of Measured Object Surface in Contact with Undeformable Surface of Measuring Tool" *MEASUREMENT SCIENCE REVIEW* 16(5): 254-259.
11. PLATFORMA OBSLUGI NAUKI PLATON; URL: <https://pcz.cloud.pionier.net.pl/>, last accessed 2018/06/25.
12. ANSYS, Inc., Canonsburg, Pennsylvania. ANSYS Structural Analysis; URL: <https://www.ansys.com/products/structures>, last accessed 2018/06/25.

## NOISE EMISSION AND VIBRATION STUDY OF A MISTA RD-165 FHAD GRADER TO REDUCE ENVIRONMENTAL HARMFUL IMPACT

### BADANIA HAŁASU I DRGAŃ RÓWNIARKI MISTA RD-165 FHAD MAJĄCE NA CELU ZMNIEJSZENIE JEJ SZKODLIWEGO WPŁYWU NA ŚRODOWISKO

Janusz KOBIAŁKA<sup>1,\*</sup> , Andrzej BARSZCZ<sup>1</sup> 

<sup>1</sup> Sieć Badawcza Łukasiewicz-Warszawski Instytut Technologiczny, ul. Racjonalizacji 6/8, Warszawa, Polska.

\* Corresponding author: [janusz.kobialka@wit.lukasiewicz.gov.pl](mailto:janusz.kobialka@wit.lukasiewicz.gov.pl)

#### Abstract

Construction machinery noise emission and vibration on the operator site are the most important harmful factors having impact on human health. They affect for people working on the operators and as well as other persons around the machine. The article concerns the issues of noise level and noise emission measurements applied to the earthmoving machinery which are covered by the EU directive 2005/88/EC. The methods of noise testing during design and in the certification, process has been described. The basic information about testing the noise emission to the environment has been presented.

Methods and results of vibration tests affecting the operator are also presented.

The reference documents and EU standards concerning this topics have been described.

The noise testing methods has been presented based on the prototyping and R&D cycle of the Mista RD-165 FHAD grader which is subjected to the European noise limits. The results of noise measurements and sound power level determination has been presented. The testing procedure implemented during two stages of R&D cycle. The article describes the effects of the improvements in the grader focused on noise emission limitation limits.

**Keywords:** earth moving machinery, grader, noise emission, noise level, vibrations.

#### Streszczenie

Hałas emitowany przez maszyny budowlane jest jednym z głównych czynników szkodliwych wpływających na środowisko, a szczególnie na zdrowie osób przebywających w obszarze oddziaływania tych maszyn. Narażonym na hałas poddane są osoby bezpośrednio zaangażowane w pracę, ale również inne osoby znajdujące się w otoczeniu maszyny. Artykuł porusza zagadnienia badania hałasu i drgań miejscowych w maszynach budowlanych podlegających pod dyrektywę Unii Europejskiej 2005/88/WE. Omówione zostały sposoby badania hałasu w trakcie produkcji i certyfikacji maszyn. Przedstawiono podstawowe informacje dotyczące przeprowadzania badań emisji hałasu do otoczenia. Przywołano dokumenty odniesienia i normy badawcze które regulują te badania.

Na przykładzie równiarki drogowej Mista RD-165 FHAD, która podlega limitom emisji hałasu, przedstawiono prowadzenie badań podczas prac badawczo-rozwojowych. Przedstawione zostały wyniki pomiarów hałasu i wyznaczona moc akustyczna maszyny. Badania były wykonywane na dwóch etapach prac konstrukcyjnych. W artykule zaprezentowano efekty prac doskonalących konstrukcję pod względem zmniejszenia emisji hałasu do otoczenia

**Słowa kluczowe:** maszyny do robót ziemnych, równiarka, emisja hałasu, poziom hałasu, wibracje.

## 1. Introduction

Every earthmoving machine introduced to the European Union market should get the CE marking. This confirms that the machine has undergone an assessment process of meeting the requirements of the New Approach Directives and/or standards harmonized with them for the human protection and environmental protection.

In the design procedure and subsequent certification of a new machinery, studies are conducted that target the impact of harmful factors on human health. Among such tests are: machine noise emitted into the environment, noise occurring at the operator's space and mechanical vibrations affecting the machine user.

Noise emitted into the environment by earthmoving machinery is a component of street and road noise. This type of noise in the opinion of people is considered the most harmful and annoying. The permissible levels of noise in the environment were published in the Regulation of the Minister of Environment of January 22, 2014 (Rozporządzenie Ministra Środowiska z dnia 22 stycznia 2014 r.). Studies conducted by the Chief Inspectorate of Environmental Protection (GIOS) have shown that road noise above 65dB threatens as much as 54% of the population in Poland. This is why it is so important to limit the noise emitted into the environment by any vehicle operating in and around the road, as well as construction sites.

It is also important to limit noise and vibration affecting the machine operator inside the vehicle, at the workspace. The permissible levels of these hazards are outlined in the Decree of the Minister of Family, Labor and Social Policy of June 12, 2018 (Rozporządzeniu Ministra Rodziny, Pracy i Polityki Społecznej z dnia 12 czerwca 2018 r.) on the highest permissible concentrations and intensities of factors harmful to health in the work environment, and in the Decree of the Minister of Economy and Labor of August 5, 2005 (Rozporządzeniu Ministra Gospodarki i Pracy z dnia 5 sierpnia 2005 r.) on health and safety at work involving exposure to noise or mechanical vibration. Health and safety regulations limit the exposure to harmful factors to which an operator of the machinery may be subjected. Exposure to noise and vibration in this case is determined on a 8-hour workday basis. In order for OSH supervision to be possible, it is required that the manufacturer informs in the manual what the noise and vibration exposure levels are at the operator's workplace, as well as what sound power the machine has.

### 1.1. Study machine

Grader RD-165 FHAD manufactured by MISTA Sp. z o.o. Stalowa Wola is the example of a machine that falls under the above mentioned requirements and was subjected to vibroacoustic testing at the prototype and manufacturing stage. Machine intended for testing was indicated by the manufacturer, i.e. the MISTA company. The grader has got a 129kW engine with a maximum speed of 2200 rpm. It worked 10 hours until the measurements began (Fig. 1).



Fig. 1. Front view of the Mista RD-165 FHAD grader

### 1.2. Noise emitted into the environment

The grader was subjected to tests of noise emissions to the environment, which were conducted in accordance with PN-EN ISO 3744. The detailed conduct of measurements, preparation of the test object and processing of the results were conducted in accordance with the ISO 6395 standard for earthmoving machinery. The latter standard details the test method to determine sound power for all common earth-moving machinery. The requirements for graders are outlined in Annex G of ISO 6395. The machine is subjected to measurements of time-averaged sound pressure levels corrected for A-frequency characteristics.

Tests are carried out at points around the machine, distributed over a defined measuring surface matched to the test object. In the case of earthmoving machinery, this is usually a hemisphere or quarter of sphere with a reflective plane, which is a hardened surface. Due to the type of testing ground, a quarter sphere with a hardened concrete slab was used to test the grader. The machine, due to its pneumatic tires, moved on the paved surface. For the grader, the standard stipulates driving forward only during the work cycle. The radius of the quarter sphere was 16 m. A set of Bruel & Kjaer microphones connected to

a PULSE portable recorder was used for the measurements. The microphones were distributed at 3 points according to the indications of the standard, and the measurements were carried out while the machine was positioned in both directions along the X axis, thus reflecting the measurement on the hemisphere. Based on the averaged result of the sound pressure measurement, the acoustic power of the machine was calculated.

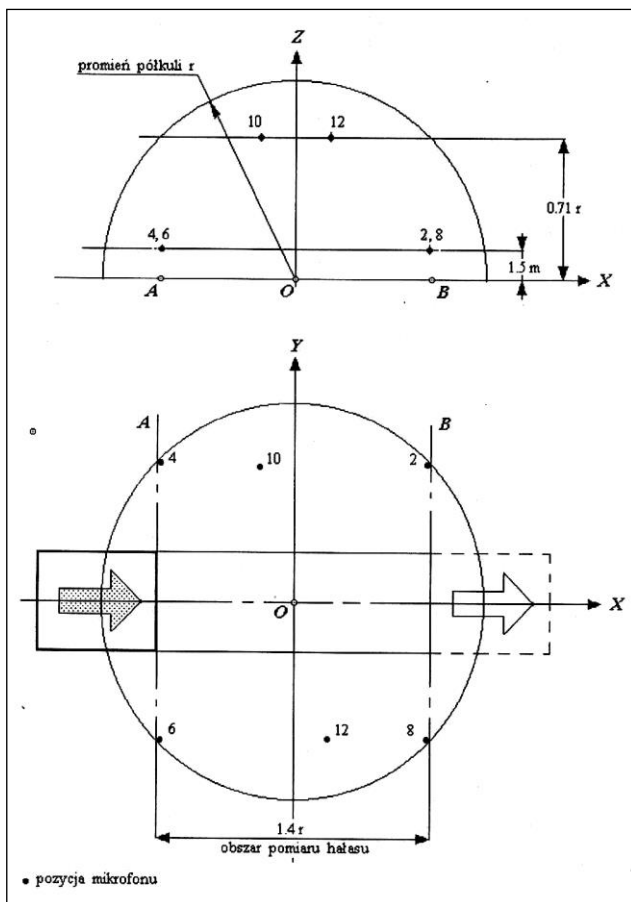


Fig. 2. Microphone array for determining sound power (Source: ISO 6395 standard page 4.).

Other machine tests concerned the operator's workspace. Inside the cab, the noise affecting operator was measured, as well as the level of general and local vibrations to which the operator is subjected during the work cycle.

Noise tests affecting the operator were carried out in accordance with the method specified in ISO 6396. The measurement microphone of the SONOPAN SON-50 device was placed on the operator's helmet near the operator's ear and pointed in the direction of his gaze. Three measurements lasting 5 minutes each were carried out while the machine was in operation, driving around the testing ground on both unpaved

and paved surfaces. During the runs they were measured:

- equivalent A-frequency corrected sound level,
- maximum frequency-corrected sound level A,
- peak sound level corrected by frequency characteristics C.

### 1.3. Vibration test

The EN 1032+A1 standard governs the mobile machinery vibration emissions tests. In addition, other standards define the rules for measuring and determining exposure to two types of vibrations affecting humans working on machinery.

The basic type of vibration is general vibration, which affects the entire human body. These vibrations are dealt with in PN-EN 14253 +A1 standard. Such vibrations are introduced into the body either through the ground on which the machine operator works in a standing position, or through the seat. The latter situation is most common in earthmoving machines. The test is carried out by measuring with a special seat vibration sensor measuring in the three axes of the coordinate system, which is placed in the center of the seat and pressed down by the weight of the operator's body.

The second type of vibration is that which acts locally, such as the machine handles parts, which operator holds with his hands. This could be, for example, the steering wheel, other handles or manipulators. A tri-axial sensor is mounted to such items, the orientation of which is specified in EN ISO 5349 standard, which specifies a method for measuring local vibrations. Either type of vibrations are measured by recording their value during the work cycle, which is representative of the machine operating characteristics, i.e. including the full variability of the emitted vibrations.

The vibration waveforms are then subjected to tertial analysis, which results in vibration acceleration results in 1/3 octave frequency bands. The effective vibration accelerations in the frequency bands are corrected by filters that perform frequency weighting according to the curves specified in the mentioned standards. General and local vibrations have separate weighting curves, resulting from the characteristics of the effects of these vibrations on the human body. In the grader, vibration measurements were made with a set of two tri-axial sensors connected to a portable recorder made by Bruel & Kjaer. The waveforms were analyzed on dedicated software. The measurements were made during runs lasting 5 minutes each. Five runs were recorded, and the results obtained from these runs were then averaged.



Fig. 3. Rear view of the Mista RD-165 FHAD grader

## 2. Acoustic power and vibration tests to improve vehicle mechanical design

MISTA RD-165 FHAD grader acoustic power tests were carried out at 2 stages of research and development works. The first measurements were carried out at the first version of the prototype. The machine tested at this stage had a developed superstructure and drive train, while body finishing elements such as engine covers, radiator covers, or exhaust system mounting and insulation elements were not yet worked out.



Fig. 4. MISTA RD-165 FHAD – first tested prototype

The measurements carried out at this stage gave an indication of the estimated sound power level for the first machine prototype. The test results of this stage slightly exceeded the acceptable guaranteed sound power level, i.e., the measurement uncertainty margin

-  $107.5 \pm 1.9$  dB (A) exceeded the limit imposed by the Noise Directive for a grader with a power of 129 kW., It was  $L_{wA} \leq 108$  dB(A). This meant that the guaranteed sound power level was not within the limit.

The grader underwent further work, The new engine covers were design. Soundproofing liners were applied to their inner side. A louver was installed to direct the propagation of noise from the radiator fan toward the ground. The installation of the exhaust system was improved, isolating it from the body. This reduced the number of potential secondary noise sources. The second series of test included a production version of the machine. It score the changes due the tests from the first prototype.



Fig. 5. MISTA typ RD-165 FHAD – second prototype

The designers took into account in their design work issues related to the elimination of noise sources in the machine. Tests of the machine after the development work yielded satisfactory results. The determined sound power level has decreased so much that, taking into account the measurement uncertainty, it is possible to guarantee compliance with the requirements of the EU Noise Directive 2005/88/EC.

Standards take so-called dominant value as the final result of the tests for local vibrations. The dominant value is the highest value of vibration from each direction of measurement, taking into account the coefficients. The Z-axis is the direction along the spine of the seated operator, while X is the forward direction and Y is the side direction For local vibration, the test result is the resultant vector from the 3 measurement directions.

Table 1. Comparison of test results with the Polish and EU requirements for machinery

No	Tested product feature or quantity and requirements	Tests or observation results
1	Noise acting on the operator - Equivalent sound level A According to the Dziennik Ustaw Nr 2014 June 6, 2014, No. 817 $L_{Aeq,dop} \leq 85$ dB(A)  According to the Dziennik Ustaw Nr 157, August 5, 2005 r. No. 1318 "action threshold" $\leq 80$ dB(A)	$L_{Aeq} = 79 \pm 3$ dB(A)
2	Noise acting on the operator - Maximum sound level A According to the Dziennik Ustaw Nr 2014, August 6, 2014 r. No. 817 $L_{Amax,dop} \leq 115$ dB(A)	$L_{Amax} = 80 \pm 3$ dB(A)
3	Noise acting on the operator - Peak sound level C According to the Dziennik Ustaw Nr 2014, August 6, 2014 r. No. 817 $L_{Cpeak,dop} \leq 135$ dB(C)	$L_{Cpeak} = 107 \pm 5$ dB(C)
4	Vibrations acting on the whole body According to the Dziennik Ustaw Nr 2014 z dnia June 6, 2014 r. No. 817 Effective frequency-weighted vibration acceleration dominant among vibration accelerations determined for the three directional components X, Y, Z, taking into account a factor of 1.4 for X,Y directions, with an 8-hour vibration effect on humans $a_{vmax dop} = 0.8$ m/s <sup>2</sup> according to the Dziennik Ustaw Nr 157 z dnia 5 sierpnia 2005 r. poz.1318 "action threshold" = 0.5 m/s <sup>2</sup>	$a_{wmax} = 0,41 \pm 0,13$ m/s <sup>2</sup> ,
5	Regulation of the Ministry of Economy of October 21, 2008 on essential requirements for machines Dz.U. nr 199, No. 1228 The manuals of the moving machine should include the highest weighted effective value of the acceleration of vibrations acting on the whole body of the operator, when this value exceeds 0.5 m/s <sup>2</sup> - if this value does not exceed 0.5 m/s <sup>2</sup> , this information should be included in the instructions	
6	Vibrations acting through the upper limbs According to the Dziennik Ustaw Nr 2014 of June 6, 2014 r. No. 817  The values of the vector sum of the effective weighted vibration accelerations determined for the three directional components X, Y, Z should not exceed 2.8 m/s <sup>2</sup> , with an 8-hour vibration effect on a person. $a_{hv} / (w, \acute{s}r)_{wek} (8h)_{dop} = 2.8$ m/s <sup>2</sup>  according to the Dziennik Ustaw Nr 157 August 5, 2005 r. No. 1318 "action threshold" = 2.5 m/s <sup>2</sup>	$a_{hv} = 1,253 \pm 0,49$ m/s <sup>2</sup> ,
7	Regulation of the Ministry of Economy of October 21, 2008 on essential requirements for machines Dz.U. nr 199, poz. 1228 The manual of the moving machine should include the total value of vibrations acting on the upper limbs of the operator, if the value exceeds 2.5 m/s <sup>2</sup> , if the value does not exceed 2.5 m/s <sup>2</sup> , this information should be included in the manual	
8	Corrected sound power level $L_{wA} \leq 108$ dB(A)	Prototype $L_{wA} = 107,5 \pm 1,9$ dB(A)  Manufacture machine $L_{wA} = 103,9 \pm 1,9$ dB(A)

### 3. Summary and conclusions

The RD 165 FHAD grader is a machine developed by MISTA Sp. z o.o. of Stalowa Wola under the project POIR.01.01.01-00-0236/15 "Development of innovative technology for the control system and

engine cooling system of a hydrostatic drive road grader - RD-165 FHAD (Full Hydrostatic Advance Drive)". The machine is equipped with a 129 kW diesel engine, and its driving system is fully hydrostatic. As a result of cooperation between the manu-

facturer and the Łukasiewicz Research Network - Institute of Mechanization of Construction and Rock Mining, Machinery and Construction Laboratory, vibro-acoustic tests of the machine were carried out during development work, as well as after its completion and manufacturing of the final unit. As a result, it was verified whether the levels of sound power and noise at the operator's workstation and vibrations affecting him are at an acceptable level in relation to the legal regulations in force in this matter. A comparison of the results with the requirements is shown in Table 1. The first tests of sound power were carried out at the prototype stage, and their results, taking into account measurement uncertainty, did not provide a guarantee of compliance with the requirements of the Machinery Directive. The manufacturer improved the components responsible for reducing noise emissions to the environment. Re-testing was carried out on the production copy, with successful results that ensured compliance with the requirements. The tests carried out indicate that vibro-acoustic testing is an important component of research and development work on earth-moving machinery and any other machinery where optimization of the design in terms of vibration and noise emissions is taken into account.

## References

1. Kazimierska-Grębosz M., „Problem hałasu w czasie eksploatacji maszyn do prac ziemnych”; Biuletyn WAT vol. LVI, Numer Specjalny, 2007.
2. <https://bhpodpodeszewki.pl/halas-w-srodowisku-pracy/>
3. Dobrowolska D., Kolasa J., „Akustyka Ultradźwięki Drgania mechaniczne Przewodnik po dziedzinie”; Materiał opracowano w Biurze Strategii Głównego Urzędu Miar.
4. Dyrektywa Unii Europejskiej 2005/88/WE; <https://eur-lex.europa.eu/legal-content/PL/TXT/PDF>
5. Rozporządzenie Ministra Środowiska z dnia 22 stycznia 2014 r.; <https://isap.sejm.gov.pl/isap.nsf/download.xsp/WDU20140000112/O/D20140112.pdf>
6. Rozporządzenie Ministra Rodziny, Pracy i Polityki Społecznej z dnia 12 czerwca 2018 r.; <https://isap.sejm.gov.pl/isap.nsf/DocDetails.xsp?id=WDU20180001286>
7. Rozporządzenie Ministra Gospodarki i Pracy z dnia 5 sierpnia 2005 r.; <https://isap.sejm.gov.pl/isap.nsf/DocDetails.xsp?id=WDU20051571318>
8. Norma ISO 6395 <https://cdn.standards.iteh.ai/samples/12730/0e4f7ce91aa4490d809e597936d1310f/ISO-6395-1988.pdf>
9. Norma PN-EN 1032+A1; <https://sklep.pkn.pl/pn-en-1032-a1-2010p.html>
10. Norma PN-EN ISO 5349; <https://sklep.pkn.pl/pn-en-iso-5349-2-2004-a1-2015-11p.html>